FOREWORD

This report was prepared for the National Aeronautics and Space Administration, Ames Research Center, Moffett Field, California. This work was performed between 1 April 1975 and 15 December 1975. The technical monitor at NASA was Dr. Wayne Johnson. The principal SCI (Vt) investigator was W. Earl Hall, Jr. Project engineers were Richard Mohr and Robert Walker. Report preparation was done by Deborah Buenz.

TABLE OF CONTENTS

TABLE OF CONTENTS (CONCLUDED)

LIST OF FIGURES

LIST OF FIGURES (CONTINUED)

LIST OF FIGURES (CONTINUED)

LIST OF FIGURES (CONCLUDED)

LIST OF TABLES

LIST OF SYMBOLS

A_i	Amplitude of frequency response
A_2, A_1, A_o	Mass, damper, and spring matrices of dynamic equations
a	Acceleration, $\ddot{x}$ (Appendix B)
a_2, a_1, a_o	Mass, damper, and spring matrices of cantilever wing and support dynamic equations (Appendix A)
$\tilde{a}$	Coefficient matrix for rotor forces and moments in the cantilever wing and support dynamic equations (Appendix A)
B	Coefficient matrix for control vector in dynamic equations
B_G	Coefficient matrix for gust vector in dynamic equations
b'	Coefficient matrix for control vector in cantilever wing and support dynamic equations (Appendix A)
b'_G	Coefficient matrix for gust vector in cantilever wing and support dynamic equations (Appendix A)
c	Damping coefficient (Appendix B)
$C_{x_s}, C_{y_s}, C_{\psi_{sup}}$	Damping coefficients for x_s, y_s, and ψ_{sup} (support) degrees of freedom
D	Control distribution matrix in measurement equation
D'	Gust distribution matrix in measurement equation
e	Base of natural exponentials
F	State dynamics matrix
F_i	Generalized force for the i^{th} generalized coordinate in Lagrange's equation (Appendix A)
f	Control variable (Appendix B)

G	Control distribution matrix in state dynamics equation
g	Gust vector
H	State distribution matrix in measurement equation
H	Transfer function
H	Inplane rotor force (Appendix A)
h	Distance from wing tip elastic axis to rotor hub (Appendix A)
I	Identity matrix
$I(\zeta)$	An integral used in damping calculation $$I(\zeta) = \int_{\omega_1}^{\omega_2} \frac{2\zeta\omega_n\omega^2}{(\omega_n^2-\omega^2)^2+(2\zeta\omega_n\omega)^2}\, d\omega$$
j	$= \sqrt{-1}$, imaginary unit
$K_{x_s}, K_{y_s}, K_{\psi_{sup}}$	Spring constants for x_s, y_s, and ψ_{sup} degrees of freedom
k	Spring coefficient
k_i	Residue for i^{th} pole of impulse response
k_i'	Residue for i^{th} pole of response to sinusoidal input
L	Gust correlation distance
L	Lagrangian, difference of kinetic and potential energy (Appendix A)
ℓ_{x_f}	Distance fuselage c.g. is ahead of support yaw axis
ℓ_{x_p}, ℓ_{y_p}	Distance the pylon c.g. is ahead and above the wing tip elastic axis
ℓ_{x_w}, ℓ_{y_w}	Distance cantilever root restraint of wing at the root elastic axis is ahead and to the right of support yaw axis

LIST OF SYMBOLS (CONTINUED)

M_x, M_y	Rotor moments about the rotor's x and y axes
MPR	Modal power ratio
m	Mass
m_s	Sum of fuselage, wing, and pylon masses
N/S	Noise-to-signal ratio
n	Noise vector
p	Wing torsion degree of freedom
Q	Rotor torque about the z axis (shaft)
q	Power spectral density of gust
$q_{w_1} = q_1$	Lowest mode wing vertical bending degree of freedom
$q_{w_2} = q_2$	Lowest mode wing chordwise bending degree of freedom
R_i	Residue of i^{th} pole
r	Power spectral density of measurement noise
S/N	Signal-to-noise ratio
s	Laplace independent variable
T	Transfer function
T	Kinetic energy (Appendix A)
T	Rotor thrust (Appendix A)
t	Time
U_o	Wing velocity
u	Control vector

LIST OF SYMBOLS (CONTINUED)

V	Variance
V	Potential energy (Appendix A)
X_n, X_s	Power under the noise and signal power spectra
x	State vector
x_s	Support longitudinal degree of freedom
x, y, z	Cartesian position coordinates
Y	Rotor force along y axis (Appendix A)
y	Measurement vector
y_s	Support lateral degree of freedom
y_{T_w}	Wing semispan, distance from root restraint to shaft axis along wing elastic axis
α	Angular position vector (Appendix A)
β_{1c}, β_{1s}	Rotor tip-path-plane pitch and yaw degrees of freedom
β_o	Rotor coning degree of freedom
β_{GC}, β_{GS}	Rotor gimbal pitch and roll angles
β_{+1}, β_{-1}	Rotor gimbal modes above and below once per rotor revolution in frequency
Γ	Gust distribution matrix in state dynamics equation
γ	Lock number (Appendix A)
Δ	Distortion factor of transfer functions due to calibration errors
δ_f	Wing flaperon deflection angle

LIST OF SYMBOLS (CONTINUED)

$\delta_{w_1}, \delta_{w_2}, \delta_{w_3}$	Wing dihedral, sweep, and incidence angles
ϵ	Control calibration error
ζ	Damping factor
ζ_{+1}, ζ_{-1}	Rotor inplane bending modes above and below once per rotor revolution in frequency
η	Measurement calibration error
η	Blade bending mode shape (Appendix A)
η'	Slope of bending mode (Appendix A)
θ_o, θ_{coll}	Collective pitch
θ_c	Lateral cyclic pitch
θ_s	Longitudinal cyclic pitch
λ_i	i^{th} pole of transfer function or, equivalently, i^{th} eigenvalue of F matrix
ξ_i	i^{th} generalized coordinate in Lagrange's equation (Appendix A)
ϕ	Frequency spectrum
ϕ_u, ϕ_v, ϕ_w	Frequency spectra of gust components
ϕ_i	Phase angle of frequency response
σ	Standard deviation
ψ_s	Rotor rotational speed perturbation
ψ_{sup}	Support yaw degree of freedom
ω	Frequency
ω_n	Natural frequency

LIST OF SYMBOLS (CONCLUDED)

Subscripts

A	Asymmetric
A	Reference frame centered at wing elastic axis root restraint (Appendix A)
a	Actual or true
f	Fuselage
I	Inertial reference frame (Appendix A)
L	Left
m	Measured
p	Pylon
p	Peak
R	right
rms	root-mean-square
S	Symmetric
w	Wing

Operators

$(\dot{})$, $(\ddot{})$	First and second derivatives with respect to time
$(\ )^{-1}$	Matrix inverse
$(\ )^{T}$	Matrix transpose
Im( )	Imaginary part of complex quantity
$\mathcal{L}(\ )$	Laplace transform
Re( )	Real part of complex quantity

I. INTRODUCTION AND SUMMARY

1.1 INTRODUCTION

The XV-15 is an advanced tilt rotor research aircraft (Figure 1.1) currently under development by the National Aeronautics and Space Administration and the U.S. Army Air Mobility R&D Laboratory. An important element of the aircraft development is an extensive full-scale wind tunnel test to be conducted in the Ames Research Center 40- by 80-foot wind tunnel. Since previous wind tunnel scale model and full-scale tests of the tilt rotor concept have been effective in previous years, it is desired to conduct the forthcoming XV-15 tests in a comprehensive manner to continue to minimize uncertainties in system characteristics.

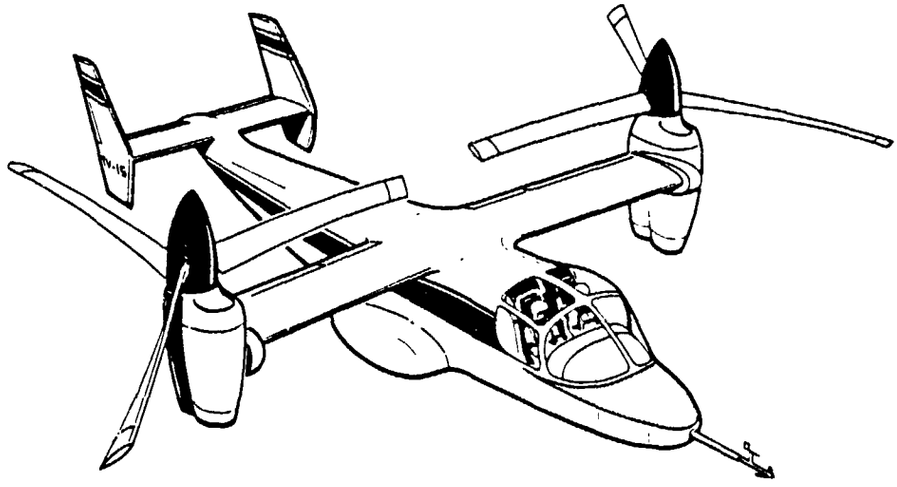

Figure 1.1 The NASA/Army XV-15

This study is a determination of specific test requirements which impact the conduct of these tests. This research is based on a mathematical model of the XV-15. This model is used to analyze the dynamic characteristics of the vehicle at 190 knots in the wind tunnel.

1.2 METHOD OF APPROACH

The method of approach used for this work is schematically shown in Figure 1.2. The mathematical model was converted into a simulation and a state vector format. These two reformulations were then combined with existing data on the input control channels and instrumentation characteristics to provide a model for the test system.

The next steps were the evaluation of the test model to determine basic requirements on the data analysis algorithms. In particular, this step produced an evaluation of mode identifiability which set further requirements on instrumentation and inputs.

Originally, the effort was directed to a basic rotor/cantilever wing model. During the course of this effort, coordination with the test agency indicated the need for results which expanded this method of approach to coupled modes between both wings. The steps were repeated for this case.

1.3 PRINCIPAL CONTRIBUTIONS AND CONCLUSIONS

The following analytical tools have been developed:

(1) An XV-15 digital simulation incorporating a simplified tunnel support model, control system loop, measurement lags, gust disturbances, and sensor noise. Time histories are generated from this simulation which provide a correlation base for the tunnel tests, as well as a means of evaluating various data processing methods.

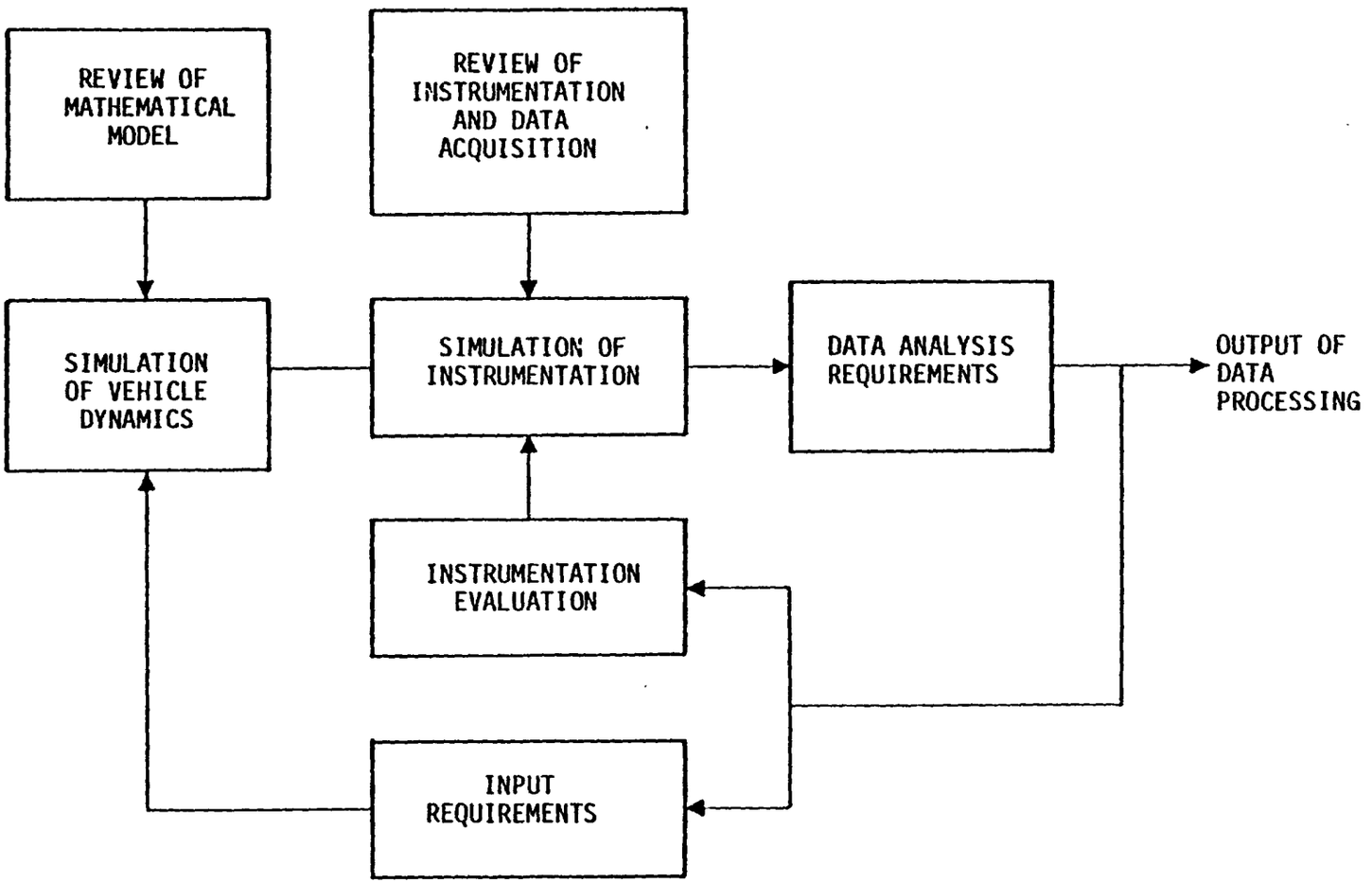

Figure 1.2 Study of XV-15 Tunnel Test Procedures and Analysis

(2) Specialization of existing data analysis programs to the high order XV-15 dynamical model. The programs so specialized at various stages of this work are: (a) the transfer function program, (b) a time series analysis program (FFT, auto-correlation, transfer functions), and (c) SCIDNT, an advanced maximum likelihood parameter identification program.

(3) Several auxiliary programs have been developed to provide estimates of damping from transfer functions, as well as calculation of modal decomposition of system response (to identify modes), particularly useful for analysis of coupled wing responses.

Application of these programs to the basic symmetric, nine degree-of-freedom mathematical model have produced the following conclusions (see Table 1.1):

(1) If the test configuration at 190 knots is such that control inputs are limited to collective pitch and flaperon at frequencies below approximately 5 Hz and measurements are made only of the wing bending accelerations, $\ddot{q}_{w1}$ and $\ddot{q}_{w2}$, then sufficient information for calculating modal frequency and damping accurately is available only for the q_{w1} and q_{w2} modes. (Necessary input amplitudes to achieve a desired noise-to-signal ratio for different levels of wind gust and speed of actuator response can be obtained from Figures 3.3-3.7 for the cantilever wing and Figures 4.6-4.8 for the coupled wing.)

(2) If the above test configuration could be improved to allow flaperon input frequencies in the vicinity of 10 Hz, then information would be sufficient to compute modal frequency and damping of the wing torsion mode from measurements of the wing bending accelerations.

Table 1.1

Frequency and Damping Information Available in Various Test Configurations for the Nine Degree-of-Freedom Symmetric Model

CONTROL INPUT:		NOT LIMITED	FREQUENCY BAND LIMITED AT 5 HZ	θ_o, θ_{1C}, θ_{1S}, δ_f FREQUENCY BAND LIMITED AT 5 HZ (FIRST ORDER LAG)			θ_o, δ_f ONLY FREQUENCY BAND LIMITED AT 5 HZ (FOURTH ORDER LAG)		
MEASUREMENTS:		ALL 9 DOF MEASURED		$\ddot{q}_1,\ddot{q}_2,p,$ β_{GC},β_{GS}	$\ddot{q}_1,\ddot{q}_2,p$	$\ddot{q}_1,\ddot{q}_2$	$\ddot{q}_1,\ddot{q}_2,p$ β_{GC},β_{GS}	$\ddot{q}_1,\ddot{q}_2,p$	$\ddot{q}_1,\ddot{q}_2$
MODE	q_1	✓	✓	✓	✓	✓	✓	✓	✓
	q_2	✓	✓	✓	✓	✓	✓	✓	✓
	p	✓	✓	✓	✓	✓	X	X	X
	β	✓	✓	✓	✓	✓	X	X	X
	ζ_{+1}	✓	✓	✓	✓	X	X	X	X
	β_{+1}	X	X	X	X	X	X	X	X
	ζ_{-1}	X	X	X	X	X	X	X	X
	β_{-1}	X	X	X	X	X	X	X	X

NOTE: (1) The ζ collective mode is not oscillatory, but consists of two real poles.

(2) A "✓" indicates information is sufficient to compute modal frequency and damping.

(3) A "X" indicates such information is insufficient.

(3) Similarly, collective pitch input frequencies near 20 Hz would provide information for the frequency and damping of the rotor coning mode, β.

(4) If instrumentation is provided to measure the wing torsion degree-of-freedom, p, and if cyclic pitch control at 18.6 Hz is possible, then the frequency and damping of the upper rotor inplane bending, ζ_{+1}, could be determined.

(5) Even under the best of circumstances (i.e., any of the four controls could be excited at any frequency and measurements could be taken of all nine degrees-of-freedom) sufficient information is not present in the transfer functions to calculate the modal frequencies and dampings of the upper and lower gimbal modes, β_{+1} and β_{-1}, and the lower rotor inplane bending mode, ζ_{-1}. It is because these modes are well damped that there are no resonant peaks associated with them in the transfer functions.

Consideration of the coupled wing motions in the presence of control and measurement calibration errors produced the following conclusions:

(1) The test configuration of exciting one wing and measuring the response of that wing makes the determination of frequency and damping of individual modes extremely difficult since the symmetric and asymmetric modes usually result in a single resonant peak in the frequency response.

(2) Symmetric and asymmetric motions can be separated if either both wings are excited and/or the responses of both wings are measured.

(3) Errors in calculating a mode's frequency and damping from its resonant peak may still occur if the motion of other modes is significant.

(4) Measurement and control calibration errors less than 20% do not produce significant errors in calculating damping values compared to the problem stated in (3) above.

1.4 SUMMARY OF REPORT

The objective of this report is to present principal modeling and analysis approaches and reference material for tunnel test planning. Chapter II discusses the modeling of the aircraft, instrumentation, and controls. Chapter III reviews results of the rotor/cantilever wing model, and Chapter IV presents the coupled wing results. Chapter V gives some examples of data prediction with system identification techniques. Chapter VI presents detailed conclusions and recommendations.

The appendices provide the detailed analysis and figures upon which the text draws. Appendix A is the derivation of the support equations. Appendix B presents the principal derivations for transfer function analysis. Appendix C is the plots of transfer functions.

II. TILTING PROPROTOR MATHEMATICAL MODEL

An analytical evaluation of tilting proprotor test requirements is based on a comprehensive description of the dynamics and aerodynamics of the subject vehicle. This section discusses the basis of that description (the simulation, detailed in [2]), and modifications to this simulation which approximate typical test configuration constraints and disturbances. Section 2.1 reviews essential elements of the basic rotor/wing model. Section 2.2 discusses the influence of the aircraft tunnel support restraint. Coupled wing interactions are approximated in Section 2.3, followed by Section 2.4, outlining the gust simulation method, Section 2.5, modeling of instrumentation, and Section 2.6, control system representations.

2.1 REVIEW OF BASIC ROTOR WING MATHEMATICAL MODEL

The basic mathematical model of the XV-15 aircraft dynamics has been established by Johnson [2-5]. A conclusion of Reference 5 was that, in general, the basic rotor dynamics were satisfactorily described by a nine degree-of-freedom model (the first bending mode and rigid pitch mode of each blade, gimbal pitch and roll angles, and rotor speed perturbation), but that in some cases it may be reduced to six degree-of-freedom by using the quasi-static blade-torsion approximation, which is discussed in Reference 2. For the purposes of this study, it was determined that the six degree-of-freedom model was satisfactory. Hence, the complete rotor/pylon/wing model consists of the six rotor and pylon degrees-of-freedom described above, plus three degrees-of-freedom for the wing, which are lowest mode vertical bending, chordwise bending, and torsion. These nine degrees-of-freedom are listed in Table 2.1 for ease of reference.

Table 2.1
Rotor, Pylon, Wing Degrees-of-Freedom and Controls

SYMBOL	DESCRIPTION
	Degrees-of-Freedom
β_{1c}	Longitudinal component in nonrotating frame of lowest blade bending mode
β_{1s}	Lateral component in nonrotating frame of lowest blade bending mode
β_o	Coning of the rotor
β_{GC}	Gimbal pitch angle
β_{GS}	Gimbal roll angle
ψ_s	Rotor rotational azimuth perturbation
q_1	Wing vertical bending
q_2	Wing chordwise bending
p	Wing torsion
	Controls
θ_o	Blade collective pitch
θ_s	Blade longitudinal cyclic pitch
θ_c	Blade lateral cyclic pitch
δ_f	Wing flaperon deflection

Several aspects of this model deserve further comment. The lowest blade bending modes are essentially inplane bending (lead-lag) during high speed, axial flow. The effect of collective lag of the blades appears in the rotor speed perturbation degrees-of-freedom. The effects of engine and transmission dynamics are included in the equations of motion, but they do not introduce additional degrees-

of-freedom. The equations of motion include the effects of gusts and four control variables (see Table 2.1): collective, longitudinal cyclic, and lateral cyclic pitch of the blades and wing flaperon deflection.

The computer program developed by Johnson [3] calculates the equations of motion in the general form

$$A_2\ddot{x} + A_1\dot{x} + A_0x = Bu + B_Gg \tag{2.1}$$

where

- x is the state vector composed of either the nine symmetric or asymmetric degrees-of-freedom,
- u is the vector of control variables,
- g is the gust vector,
- A_2, A_1, A_0 are the "mass", "damper", and "spring" matrices, respectively, and
- B, B_G distribute the controls and gusts, respectively, among the states.

This equation is readily converted to the standard state-space form

$$\dot{x} = Fx + Gu + \Gamma g \tag{2.2}$$

where

$$x = \begin{bmatrix} x \\ \dot{x} \end{bmatrix} \tag{2.3}$$

$$F = \begin{bmatrix} 0 & I \\ -A_2^{-1}A_0 & -A_2^{-1}A_1 \end{bmatrix} \tag{2.4}$$

$$G = \begin{bmatrix} 0 \\ B \end{bmatrix} \tag{2.5}$$

and

$$\Gamma = \begin{bmatrix} 0 \\ B_G \end{bmatrix} \tag{2.6}$$

Measurements, y, of the degrees-of-freedom are modeled as linear combinations of the state and control:

$$y = Hx + Du + D'g \tag{2.7}$$

Except where stated otherwise, it is assumed that the accelerations of the wing bending degrees-of-freedom, q_1 and q_2, are measured by accelerometers and that direct measurements of other degrees-of-freedom are available as needed for the sake of discussion.

The frequency response of the measurements to the controls or gusts are available from the Laplace transfer functions

$$\frac{y(s)}{u(s)} = H(sI-F)^{-1}G + D \tag{2.8}$$

$$\frac{y(s)}{g(s)} = H(sI-F)^{-1}\Gamma + D' \tag{2.9}$$

which follow directly from Eq. (2.2). The results obtained from these functions are discussed in Chapters III and IV.

2.2 EFFECT OF SUPPORT FLEXIBILITY

A preliminary requirement for this study was to determine if the flexibility of the support structure in the 40 x 80 wind tunnel would introduce modal frequencies near frequencies of interest. If

so, the isolation of the modal frequencies of interest and the determination of the modal damping factor would be made more difficult.

Displacement of the support attachment points in a horizontal plane was considered. Vertical displacement was not considered because the support is far more rigid in that direction. Thus, the basic equations of motion were expanded to include two more degrees-of-freedom: longitudinal and lateral translation of the aircraft, x_s and y_s, respectively. Aircraft yaw is also possible, but data were not available to adequately specify the frequency and damping parameters for the yaw degree-of-freedom, so it was omitted from the study.

The support equations will be only briefly described here; a detailed derivation of the equations appears in Appendix A. The direct aerodynamic effects on the x_s and y_s degree-of-freedom are negligible compared to the structural kinetic effects; therefore, only the latter are retained in the equations. The result may be written simply as

$$m_s^* \ddot{x}_s + C_{x_s}^* \dot{x}_s + K_{x_s}^* x_s = F_{x_s} \tag{2.10}$$

$$m_s^* \ddot{y}_s + C_{y_s}^* \dot{y}_s + K_{y_s}^* y_s = F_{y_s} \tag{2.11}$$

where the asterisk superscripts denote nondimensional quantities. The mass coefficient, m_s^*, is estimated from a weight analysis of the XV-15. The terms F_{x_s} and F_{y_s} are composed of all the cross-coupling terms between the support and the remaining degrees-of-freedom, plus the effects of controls and gusts, all of which were available from the existing computer program. Therefore, only the damping coefficients, $C_{x_s}^*$ and $C_{y_s}^*$, and the spring coefficients, $K_{x_s}^*$ and $K_{y_s}^*$, remain to be specified. This was done by assuming 2%

structural damping and specifying the frequency of the support oscillations with the rotor off. These frequencies were taken as 3.5 Hz in the longitudinal direction and 4.0 Hz in the lateral, based on earlier experience in the 40 x 80 tunnel [6].

The result is shown in Figure 2.1, which compares the pole locations of the symmetric nine degree-of-freedom model to the same model with the support degrees-of-freedom added. As can be seen, the effect is an increase in the modal frequencies of the rotor-coning (β_0) mode (from 2.6 to 2.9 per rev); of the upper blade lag (ζ_{+1}) mode (from 2.4 to 2.6 per rev); and of the wing chordwise bending (q_{w2}) mode (from 0.67 to 0.84 per rev). The frequencies of the remaining modes are unchanged. The two new modes associated with x_s and y_s are at low frequencies (0.12 and 0.15 per rev, respectively) and are not expected to cause any difficulties in identifying the frequencies and damping of other modes. Also, even though the β_0, ζ_{+1}, and q_{w2} modal frequencies are altered, there still remains adequate separation of frequencies to permit discrimination of individual modes. Therefore, the conclusion is that the support flexibility does not change the basic characteristics of the XV-15 structural damping or frequencies and need not be considered in the remainder of this study.

2.3 MODELING OF COUPLED WING RESPONSES

A major part of this study was to ascertain the effects of exciting one or both rotors (or wings), the effects of measuring the response of one or both wings, and the effects of calibration errors in the measurements of the control inputs and the wing responses on the ability to correctly compute the frequency and damping of important modes. The nine degrees-of-freedom of the right rotor/pylon/wing system are coupled to the nine degrees-of-freedom of the left system, principally by means of the transmission

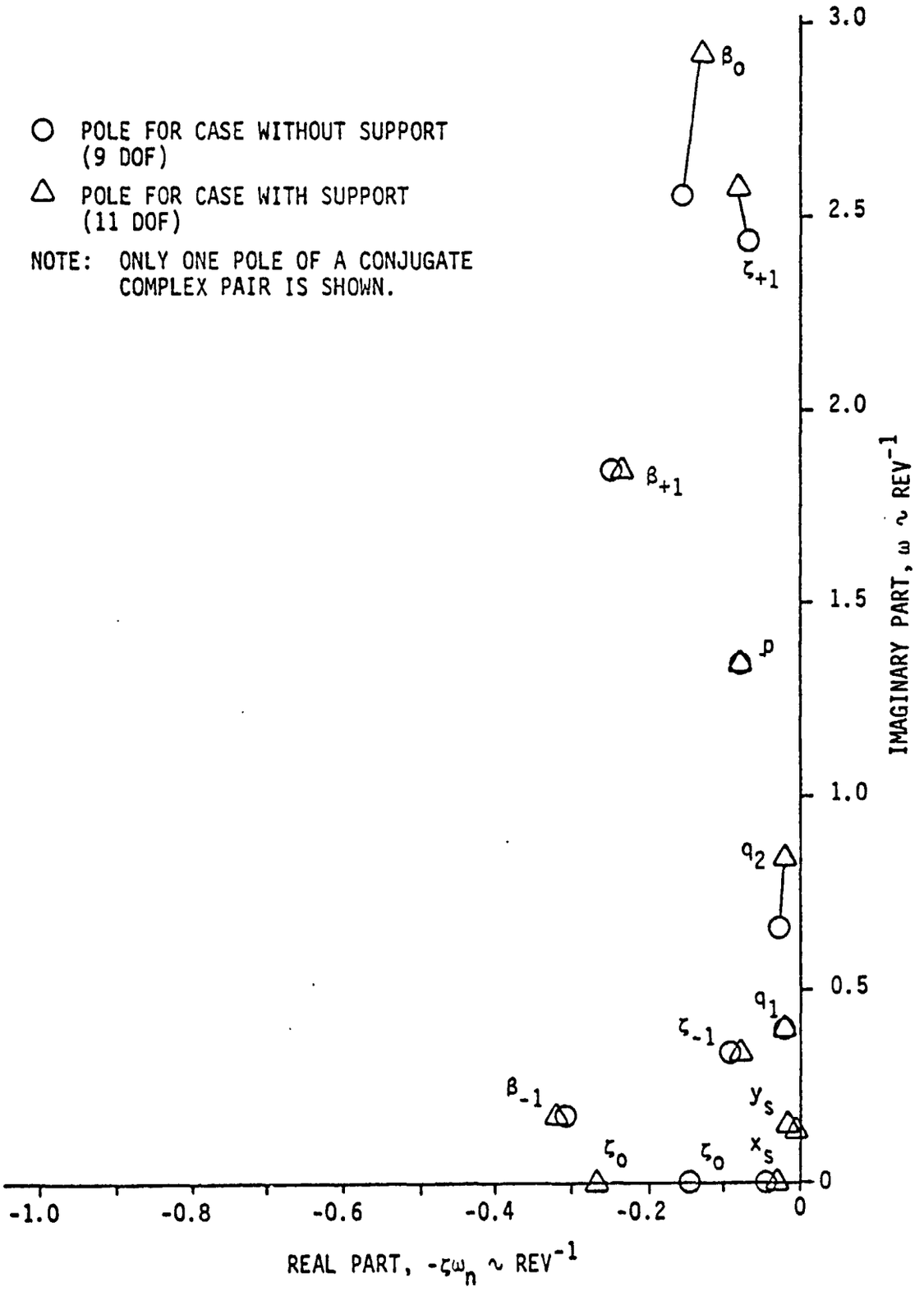

Figure 2.1 Comparison of Pole Locations for Symmetric Equations With and Without Support Degrees-of-Freedom

interconnect shaft. This left and right system of eighteen degrees-of-freedom may be decoupled into symmetric and asymmetric systems of nine degrees-of-freedom each. This procedure is advantageous because it aids the understanding of the complete system, simplifies the mathematics, and reduces the computational effort.

There are nine cases to be investigated (Table 2.2). It is assumed that the symmetric and asymmetric responses are separated whenever possible to better isolate the frequencies of individual modes.

Some definitions are helpful before proceeding with this analysis. Six subscripts which will be used are:

S ∿ symmetric
A ∿ asymmetric
R ∿ right
L ∿ left
a ∿ actual or true
m ∿ measured

The basic symmetric and asymmetric transfer functions are:

$$T_S(s) \triangleq \frac{y_S(s)}{u_S(s)} \quad , \quad T_A(s) = \frac{y_A(s)}{u_A(s)} \tag{2.12}$$

where

$$y_S(s) \triangleq \frac{1}{2}\,(y_R(s)+y_L(s)), \quad \text{measurement of symmetric response} \tag{2.13}$$

$$y_A(s) \triangleq \frac{1}{2}\,(y_R(s)-y_L(s)), \quad \text{measurement of asymmetric response} \tag{2.14}$$

Table 2.2

Transfer Functions of Coupled Wing Responses

MEASURE	EXCITE		
	ONE WING	BOTH WINGS	BOTH WINGS WITH CALIBRATION ERRORS
ONE WING	$\frac{y_R}{u_R} = \frac{y_L}{u_L} = \frac{1}{2}(T_S+T_A)$ $\frac{y_L}{u_R} = \frac{y_R}{u_L} = \frac{1}{2}(T_S-T_A)$	$\frac{y_R}{u_S} = \frac{y_L}{u_S} = T_S$ $\frac{y_R}{u_A} = -\frac{y_L}{u_A} = T_A$	$\frac{y_R}{u_{S_m}} = T_S\left(1+\frac{\epsilon_R+\epsilon_L}{2}\right) + T_A\left(\frac{\epsilon_R-\epsilon_L}{2}\right)$ $\frac{y_R}{u_{A_m}} = T_A\left(1+\frac{\epsilon_R+\epsilon_L}{2}\right) + T_S\left(\frac{\epsilon_R-\epsilon_L}{2}\right)$
BOTH WINGS	$\frac{y_S}{u_R} = \frac{1}{2}T_S$ $\frac{y_A}{u_R} = \frac{1}{2}T_A$	$\frac{y_S}{u_S} = T_S$ $\frac{y_A}{u_A} = T_A$	$\frac{y_S}{u_{S_m}} = T_S\left(1+\frac{\epsilon_R+\epsilon_L}{2}\right)$ $\frac{y_A}{u_{A_m}} = T_A\left(1+\frac{\epsilon_R+\epsilon_L}{2}\right)$
BOTH WINGS WITH CALIBRATION ERROR	$\frac{y_{S_m}}{u_R} = \frac{1}{2}T_S\left(1+\frac{\eta_R+\eta_C}{2}\right) + \frac{1}{2}T_A\left(\frac{\eta_R-\eta_L}{2}\right)$ $\frac{y_{A_m}}{u_R} = \frac{1}{2}T_A\left(1+\frac{\eta_R+\eta_L}{2}\right) + \frac{1}{2}T_S\left(\frac{\eta_R-\eta_L}{2}\right)$	$\frac{y_{S_m}}{u_S} = T_S\left(1+\frac{\eta_R+\eta_L}{2}\right)$ $\frac{y_{A_m}}{u_A} = T_A\left(1+\frac{\eta_R+\eta_L}{2}\right)$	$\frac{y_{S_m}}{u_{S_m}} = T_S\left(1+\frac{\epsilon_R+\epsilon_L}{2}\right)\left(1+\frac{\eta_R+\eta_L}{2}\right) + T_A\left(\frac{\epsilon_R-\epsilon_L}{2}\right)\left(\frac{\eta_R-\eta_L}{2}\right)$ $\frac{y_{A_m}}{u_{A_m}} = T_A\left(1+\frac{\epsilon_R+\epsilon_L}{2}\right)\left(1+\frac{\eta_R+\eta_L}{2}\right) + T_S\left(\frac{\epsilon_R-\epsilon_L}{2}\right)\left(\frac{\eta_R-\eta_L}{2}\right)$

$$u_S(s) \triangleq \frac{1}{2}\,(u_R(s)+u_L(s)),\ \text{symmetric control input} \qquad (2.15)$$

$$u_A(s) \triangleq \frac{1}{2}\,(u_R(s)-u_L(s)),\ \text{asymmetric control input} \qquad (2.16)$$

Also, right and left control calibration errors (ε_R and ε_L, respectively) and the right and left measurement calibration errors (η_R and η_L, respectively) are defined such that:

$$(u_R)_{\text{actual}} = (1+\varepsilon_R)(u_R)_{\text{commanded or measured}} \qquad (2.17)$$

$$(y_R)_{\text{measured}} = (1+\eta_R)(y_R)_{\text{actual}} \qquad (2.18)$$

and the left variables are related similarly.

An example of the first case, that of exciting one wing and measuring one wing where no calibration errors are present, is the following:

$$y_R(s) = y_S(s) + y_A(s)$$

$$= \frac{1}{2}\,T_S(s)[u_R(s)+u_L(s)] + \frac{1}{2}\,T_A(s)[u_R(s)-u_L(s)] \qquad (2.19)$$

$$\therefore \quad \frac{y_R(s)}{u_R(s)} = \frac{1}{2}\,[T_S(s)+T_A(s)] \qquad (2.20)$$

$$\frac{y_R(s)}{u_L(s)} = \frac{1}{2}\,[T_S(s) - T_A(s)] \qquad (2.21)$$

Next, consider the last case, that of exciting both wings either symmetrically or asymmetrically and measuring the responses of both wings in the presence of both control and measurement calibration errors. For symmetric excitation:

$$y_{R_m} = (1+\eta_R)y_{R_a}$$

$$y_{R_a} = T_S u_{S_a} + T_A u_{A_a}$$

$$y_{R_a} = T_S\{\tfrac{1}{2}\,[u_{R_m}(1+\varepsilon_R)+u_{L_m}(1+\varepsilon_L)]\}$$

$$+ T_A\{\tfrac{1}{2}\,[u_{R_m}(1+\varepsilon_R)-u_{L_m}(1+\varepsilon_L)\} \qquad (2.22)$$

and similarly for y_{L_m} and y_{L_a}. From the above, it is easily shown that

$$\frac{y_{S_m}}{u_{S_m}} = T_S\left(1+\frac{\varepsilon_R+\varepsilon_L}{2}\right)\left(1+\frac{\eta_R+\eta_L}{2}\right) + T_A\left(\frac{\varepsilon_R-\varepsilon_L}{2}\right)\left(\frac{\eta_R-\eta_L}{2}\right) \qquad (2.23)$$

and, similarly for asymmetric excitation,

$$\frac{y_{A_m}}{u_{A_m}} = T_A\left(1+\frac{\varepsilon_R+\varepsilon_L}{2}\right)\left(1+\frac{\eta_R+\eta_L}{2}\right) + T_S\left(\frac{\varepsilon_R-\varepsilon_L}{2}\right)\left(\frac{\eta_R-\eta_L}{2}\right) \qquad (2.24)$$

The results for the remaining cases are found in a similar manner and presented in Table 2.2 Note that many cases follow directly from the above two equations when the calibration errors are set to zero as appropriate. For example, the case of measuring both wings and exciting both wings with control (but not measurement) calibration errors follows simply by setting $\eta_R = \eta_L = 0$ in the above equation.

The following observations are made concerning these results:

(1) Exciting one wing and measuring one wing does not allow the separation of symmetric and asymmetric responses.

(2) Exciting both wings with calibration error and measuring one wing means that the measured response will consist of both symmetric and asymmetric modes when only one or the other was wanted. A similar case exists when one wing is excited and both are measured in the presence of measurement error.

(3) When both wings are excited and both measured and both measurement and control errors are present, then again the unwanted modes contribute to the response. However, the fractional amount of this unwanted contribution is reduced to the order of the square of the calibration errors.

How much the presence of these unwanted modes affect the estimate of the damping factors of individual modes as computed from test data will be the discussed in Chapter III.

2.4 MODELING OF GUST EFFECTS

In general, there are two principal sources of random effects which can degrade the information content of data. These are process noise (e.g., gusts) and measurement noise. For a well instrumented aircraft, with prefiltering on data, the process noise effects are of most concern. Particularly for the wind tunnel tests at high speeds, these gust effects can obscure essential stability information.

This study required a method for emulating gust effects in both the frequency and the time domain. Gust spectra charact istics of the 40- by 80-foot wind tunnel are largely unquantified, and it is not clear as to the relation between tunnel randomness and corresponding flight gusts.

The approach used is based on use of an atmospheric gust spectrum. The von Karman spectrum is known to be one of the most accurate of isotropic atmospheric gust models, although such a spectrum is not convenient for matching with linear filters (due to noninteger factors in the spectrum). An approximating spectrum is the Dryden spectrum, which is "close" to the von Karman spectrum for low frequencies. The Dryden spectra used for longitudinal, lateral, and vertical gusts are:

$$\phi_u(w) = \frac{\sigma_u^2 L}{u_o \pi} \frac{2}{\left[1 + \left(\frac{wL}{u_o}\right)^2\right]}$$

$$\phi_v(w) = \frac{\sigma_v^2 L}{u_o \pi} \frac{1 + 3\left(\frac{wL}{u_o}\right)^2}{\left[1 + \left(\frac{wL}{u_o}\right)^2\right]^2}$$

$$\phi_w(w) = \frac{\sigma_w^2 L}{u_o \pi} \frac{1 + 3\left(\frac{wL}{u_o}\right)^2}{\left[1 + \left(\frac{wL}{u_o}\right)^2\right]^2}$$

where L is the correlation distance, u_o the wind velocity, and $\frac{L}{u_o} = T_{corr} = \frac{1}{\omega_n}$ (ω_n is the bandwidth of the noise).

For this work, the bandwidth of the noise was estimated at 2 Hz (which corresponds to a correlation distance of 25.5 ft) for all three directions. The variance of the lateral and vertical gust was chosen to be a fixed fraction of the longitudinal gust variance, but this ratio was chosen conservatively. This allowed parameterization of the noise-to-signal ratio (see Appendix B.2.3) as a function of input amplitude on the longitudinal gust rms velocity. The resulting variance is

$$\begin{bmatrix} \sigma^2_{long} \\ \sigma^2_{lat} \\ \sigma^2_{vert} \end{bmatrix} = \begin{bmatrix} 0.485 \\ 0.172 \\ 0.343 \end{bmatrix} \sigma^2_T$$

where σ_T is the total rms gust velocity.

As discussed in Section B.2.3, these spectra and variances were used with the aircraft dynamic response to random gusts to determine the power due to random gusts in a particular measurement. Viewing the three gust directions as uncorrelated with each other, their power contributions to a particular measurement can be added in an rms sense. Representations of these gust effects in time domain simulation were approximated using white noise passed through a first order filter with a break frequency at 2 Hz.

2.5 INSTRUMENTATION MODELING

Measurements were taken from the position states except those measurements with which the XV-15 is now instrumented--wing vertical bending acceleration and wing chordwise bending acceleration. The measurements were created from the appropriate linear combinations of the states and controls. The simulation did not include a lag in measurement (the strain gauge accelerometers on the pylon have bandwidth of 100 Hz (13.1 per rev), which is far above any modes of interest). Initially, random measurement noise was added to simulations, but in general the process noise (tunnel gust) was the only noise considered, due to the expected severity of such tunnel disturbance.

The transfer functions all included a first order lag at 100 Hz (13.1 per rev), but its effect is difficult to isolate since the primary modes of interest lie in the regime 0.1 to 10 per rev.

2.6 CONTROL MODELING

Two cases for the order of the control system actuator were chosen, a first order and a fourth order lag, to represent an optimistic case and worst case for the steepness with which the actuator gain falls off with frequency. The break frequency was 5 Hz. (This corresponds to a good quality control servo.)

The frequency responses discussed in Chapters II and III all include a first order lag at 5 Hz. The fourth order control lag was achieved by applying the following third order filter to the transfer function data:

$$\frac{\omega_n^3}{(s+\omega_n)(s^2+2(0.5)\omega_n s+\omega_n^2)} \quad \text{with } s = j\omega.$$

(5 Hz = 0.654 per rev). As will be seen in Chapters III and IV, there is little difference in these two representations of the actuator below 5 Hz, for example in studying the q_{w1} mode (symmetric) motion at 0.398 per rev). Of course, the fourth order lagged control would make the study of high frequency modes (greater than 1.5 per rev) prohibitive. Cyclic inputs were studied with a first order control lag at 2 Hz and 10 Hz.

Time domain simulations of the measured responses were made using different inputs (multiple sinusoids, random inputs, and swept sine), all using a first order lag, primarily at 5 Hz bandwidth but also at 10 Hz.

Scale errors between the commanded and actual control were modeled as described in Section 2.3.

III. ANALYSIS OF ROTOR/CANTILEVER WING DYNAMICS

This section presents the analytical evaluation of test considerations for rotor/cantilever wing modes. This evaluation is based on the frequency response characteristics of the nine degree-of-freedom model, discussed in Section 3.1. Section 3.2 reviews the wing modes which are of principal significance in defining stability tests at maximum tunnel speed of 190 knots. Section 3.3 shows the input considerations which are required to isolate these principal modes, and Section 3.4 discusses the effect of tunnel induced random disturbances in the measured responses. A summary is presented in Section 3.5.

3.1 FREQUENCY RESPONSE OF THE ROTOR/CANTILEVER WING MODEL

As discussed in Chapter II, the transfer function

$$\frac{y(s)}{u(s)} = H(sI-F)^{-1}G+D$$

can be used to evaluate the frequency response characteristics of the system with dynamics matrix, F; measurement distribution matrix, H; control distribution matrix, G; and direct measured inputs, D. The stability of this transfer function is completely described by the roots of the characteristic equation of F. Measurement of these stability characteristics, however, depends not only on these roots, but also on the roots of the numerator of the transfer function. These numerator roots are governed not only by the system dynamics (F), but also the mesurements and the controls which define the test configuration.

3.1.1 Transfer Functions of Rotor/Cantilever Wing Model

The primary controls available on the XV-15 are collective pitch (θ_o) and wing flaperon (δ_f), at least for the fully converted configuration. For reference, the frequency response to these inputs for all degrees of freedom of the basic rotor/cantilever wing, are given in Appendix C.

3.1.2 Evaluation Method of Transfer Functions

The transfer functions of Appendix C serve as a useful reference description of the frequency response of the nine degrees-of-freedom to collective and flaperon inputs. In this section, we examine the total information content of the transfer functions, assuming that all states are measured and input bandwidth is above the highest frequency mode of the system. This "ideal" case demonstrates the relative ranking of modal information independent of test input or instrumentation limits. In Sections 3.2-3.4, we discuss the effect of these limits in more detail. The purpose of presenting these "ideal" transfer function characteristics is to formulate a basis for discussing the desirability of more stringent requirements on instrumentation and excitation hardware.

The basic objective of stability testing is the determination of frequency and damping of system responses. For a multivariable rotorcraft system, however, it is necessary to isolate the frequency and damping of the elemental modes which produce that system response. The problem is, however, that the system response (as indicated by the transfer functions of Appendix C) represent the sum of contributions of all these elemental modes at a particular frequency. In many cases, the elemental modes are essentially uncoupled, and a particular peak corresponds to a unique degree of freedom (e.g., wing vertical bending). For the rotorcraft, however, significant modes are highly coupled and measurement of system

frequency response may not provide the desired stability characteristics for a particular degree-of-freedom. A corollary to this is that determination of system damping for a particular peak, itself a nontrivial calculation, may not define the stability of a particular degree of freedom.

There are several analytical techniques which may be used to decompose system response into contributions from various modes (such decomposition is equivalent to quantifying the identifiability of a particular degree of freedom). These techniques include the following:

(a) Mode Shape Analysis: Corresponding to a particular natural frequency of response is a mode shape associated with that frequency. This mode shape, or eigenvector, may be calculated. The eigenvector consists of a vector of components of the elemental degrees-of-freedom. The relative size of these components quantifies the participation of each degree of freedom at a natural frequency. Unfortunately, highly coupled modes yield eigenvectors which show several components of nearly equal contribution, and it is not clear how to isolate the most significant degrees-of-freedom.

(b) Residue Analysis (Appendix B): The natural response of a system mode may be written as a sum of elemental modes. The terms of this expansion are of the form

$$e^{-\zeta_i \omega_{n_i}} A_i \cos\left(\omega_{n_i} \sqrt{1-\zeta_i^2}\, t + \phi_i\right)$$

where A_i is the combined residue of the mode eigenvalue, $\lambda = \zeta_i \pm j\omega_i$ ($A_i = 2|R_i|$, where R_i is residue of λ_i). Modal content can be estimated by ranking the residues of all modes at each frequency.

(c) Modal Power (Appendix B): The modal power of a particular transfer function peak is the power contributed by the complex pole pair associated with the vibration (in a selected frequency range about the peak).

(d) Modal Power Ratio (MPR) (Appendix B): The ratio of a particular degrees of freedom power to total power of a response. The MPR can be positive or negative depending on whether a particular degree of freedom is adding or subtracting power from a resonant peak. The sum of the MPR's for each mode is unity.

The modal power and modal power ratios are used to quantify the following:

(1) Which transfer function is more desirable to identify a particular mode?

(2) Which mode is most significant in a resonant peak when more than one mode is contributing?

The modal power ratio does not include information on the magnitude of the peak. (For example, transfer function B may show a resonant peak of much less magnitude than transfer function A, yet their MPR's are nearly equal.) Thus, for selecting which transfer function is more desirable to identify a particular mode, the modal power should be used. This can be done since: (1) the system of equations is normalized so the transfer function evaluations are independent of the units, and (2) the same integration interval was used on each transfer function. When investigating one peak of a particular transfer function to determine which mode is being identified, either the MPR or modal power may be used. When comparing the uniqueness (meaning lack of other modes that contaminate) of

different peaks of one transfer function, the MPR must be used because the modal power may be computed at different frequency bandwidths for each peak.

3.1.3 Transfer Function Comparisons

Table 3.1 is a qualitative comparison of the transfer functions to collective and flaperon. Such a table is useful for rapid reference to determine the importance of measuring a particular degree-of-freedom or using a particular input. For example, the table indicates that the q_{w1}, q_{w2}, p, and β modes can be isolated (if sufficient control bandwidth is available).

Table 3.2 is the quantitative evaluation of the transfer functions, upon which Table 3.1 is based, and summarizes the modal power computations for the cantilever wing (symmetric motion) transfer functions. Transfer functions to all nine degrees-of-freedom excited by collective pitch and wing flaperon, as well as selected cyclic transfer functions, are included. In the horizontal direction of the table are the different transfer functions; in the vertical direction of the table are the different modes. As developed in Appendix B.2.2 and B.2.3, every mode contributes either positively or negatively by some great or small amount to the total power of each peak in a particular transfer function. Only contributions (in terms of MPR) greater than 5% are included in Table B.1.

Each box associated with a particular transfer function contains three values. The first is the frequency of the peak for which the modal power is computed, and the following two values are the modal power and modal power ratio (MPR). Each transfer function does not exhibit peaks at each of the modal frequencies. When a mode is not excited in a particular transfer function, the block for that mode is used to indicate that mode's contribution to the nearest adjacent peak, which is at the indicated frequency.

Table 3.1

Qualitative Comparison of Transfer Functions

FREQUENCY (CYCLES/REV)	TRANSFER FUNCTIONS															
	$\frac{\ddot{q}_{w2}}{\theta_{coll}}$	$\frac{\ddot{q}_{w1}}{\delta_f}$	$\frac{\ddot{q}_{w2}}{\theta_{coll}}$	$\frac{\ddot{q}_{w2}}{\delta_f}$	$\frac{\beta_{GC}}{\theta_{coll}}$	$\frac{\beta_{GC}}{\delta_f}$	$\frac{\beta_{GS}}{\theta_{coll}}$	$\frac{\beta_{GS}}{\delta_f}$	$\frac{p_w}{\theta_{coll}}$	$\frac{p_w}{\delta_f}$	$\frac{\beta_{1C}^1}{\theta_{coll}}$	$\frac{\beta_{1C}^1}{\delta_f}$	$\frac{\beta_{1S}^1}{\theta_{coll}}$	$\frac{\beta_{1S}^1}{\delta_f}$	$\frac{\beta_0^2}{\theta_{coll}}$	$\frac{\beta_0^2}{\delta_f}$
β (2.5548)	3	1	2	3	2	1	2	2	2	1	2	2	2	2	2	3
ζ_{+1} (2.4345)	2	1	2	2	2	1	2	2	2	1	2	2	2	2	2	2
β_{+1} (1.8546)	1	1	1	1	1	1	1	1	1	1	1	1	1	1	1	1
p (1.3440)	1	3	3	3	3	3	2	3	3	3	3	3	2,3	3	1	3
q_{w2} (0.66608)	3	1	3	3	3	1	3	1	2,3	1	3	1	3	1	1	2,3
q_{w1} (0.39852)	1	3	3	3	2	3	3	3	2	2,3	2	2,3	2	3	1	3
ζ_{-1} (0.33365)	1	1	1	1	1	1	1	1	1	1	1	1	1	1	1	1
β_{-1} (0.17635)	1	1	1	1	1	1	1	1	1	1	1	1	1	1	1	1

LEGEND:
1. Bode plot does not show a resonant peak near this modal frequency.
2. Bode plot shows a small peak, or the mode is obscured by other modes nearby in frequency with similar magnitude.
3. Bode plot shows a peak and the natural response of this mode dominates by an order of magnitude.

Tilt Rotor (9 Degree-of-Freedom Model)

V = 190 kts, μ = 0°, G_T = 0.001265

Bending Degrees-of-Freedom: 2, 3, & 4
Powered Flight - Governor
Control Bandwidth = 5 Hz

Table 3.2a

XV-15 Rotor/Cantilever Wing Modal Decomposition

MODE	TRANSFER FUNCTION PEAK QUALITY	TRANSFER FUNCTION									
		$\frac{q_{w2}}{\theta_{coll}}$	$\frac{q_{w2}}{\delta_f}$	$\frac{q_{w1}}{\theta_{coll}}$	$\frac{q_{w1}}{\delta_f}$	$\frac{\beta^1_{1c}}{\theta_{coll}}$	$\frac{\beta^1_{1c}}{\delta_f}$	$\frac{\beta^1_{1s}}{\theta_{coll}}$	$\frac{\beta^1_{1s}}{\delta_f}$	$\frac{\beta^2_o}{\theta_{coll}}$	$\frac{\beta^2_o}{\delta_f}$
Coning (β_0) (2.555 per rev)	Peak Frequency	2.512	2.512	2.630		2.400		2.400		2.512	2.512
	Modal Power	0.425E-3	0.124E-7	0.240E-4	*	-0.370E-3	*	-0.404E-3	*	0.117E-1	0.244E-6
	Modal Power Ratio	1.03	0.658	0.975		-0.307		-0.284		1.015	1.281
Upper Inplane (ζ_{+1}) (2.434 per rev)	Peak Frequency	2.512	2.512			2.400	2.400	2.400	2.400		2.512
	Modal Power	-0.241E-4	0.790E-8	*	*	0.157E-2	0.710E-5	0.184E-2	0.766E-5	*	-0.683E-7
	Modal Power Ratio	-0.058	0.420			1.311	1.020	1.292	1.034		-0.360
Upper Out of Plane (β_{+1}) (1.855 per rev)	Peak Frequency		2.512						1.320		
	Modal Power	*	-0.163E-8	*	*	*	*	*	-0.786E-5	*	*
	Modal Power Ratio		-0.0870						-0.075		
Wing Torsion (p) (1.344 per rev)	Peak Frequency		1.318	1.380	1.380	1.320	1.320	1.320	1.320		1.380
	Modal Power	*	0.119E-6	0.173E-4	0.255E-4	0.168E-3	0.221E-3	0.106E-3	0.113E-3	*	0.253E-6
	Modal Power Ratio		1.040	0.948	0.950	0.906	1.070	0.588	1.076		0.961
Wing Chordwise (q_{w2}) (0.666 per rev)	Peak Frequency	0.661	0.661	0.661		0.661		0.661		0.631	0.661
	Modal Power	0.251E-2	0.123E-6	0.158E-4	*	0.530E-2	*	0.201E-1	*	0.557E-3	0.378E-7
	Modal Power Ratio	1.020	1.031	1.225		0.940		1.097		0.327	0.700
Wing Vertical Bending (q_{w1}) (0.398 per rev)	Peak Frequency		0.417	0.398	0.398	0.398	0.398	0.398	0.398		0.398
	Modal Power	*	0.192E-8	0.655E-4	0.428E-4	0.535E-2	0.362E-2	0.211E-2	0.260E-2	*	0.700E-6
	Modal Power Ratio		0.800	1.085	1.005	1.058	1.161	1.346	1.144		1.069
Lower Inplane (ζ_{-1}) (0.336 per rev)	Peak Frequency		0.417			0.398	0.398	0.398	0.398		
	Modal Power	*	0.143E-9	*	*	0.343E-3	-.405E-3	-0.491E-3	-0.362E-3	*	*
	Modal Power Ratio		0.0596			0.0678	-0.130	-0.313	-0.159		
Lower Out of Plane (β_{-1}) (0.176 per rev)	Peak Frequency							0.398			
	Modal Power	*	*	*	*	*	*	-0.154E-3	*	*	*
	Modal Power Ratio							-0.0980			

Table 3.2b

XV-15 Rotor/Cantilever Wing Modal Decomposition

MODE	TRANSFER FUNCTION PEAK QUALITY	TRANSFER FUNCTION							
		$\frac{\beta_{GC}}{\theta_{coll}}$	$\frac{\beta_{GC}}{\delta_f}$	$\frac{\beta_{GS}}{\theta_{coll}}$	$\frac{\beta_{GS}}{\delta_f}$	$\frac{\psi_S}{\theta_{coll}}$	$\frac{\psi_S}{\delta_f}$	$\frac{p_w}{\theta_{coll}}$	$\frac{p_w}{\delta_f}$
Coning (β_o) (2.555 per rev)	Peak Frequency	2.400		2.400		2.630		2.400	
	Modal Power	-0.103E-3	*	-0.718E-4	*	0.811E-3	*	0.109E-4	*
	Modal Power Ratio	-0.215		-0.275		1.100		0.149	
Upper Inplane (ζ_{+1}) (2.434 per rev)	Peak Frequency	2.400		2.400	2.400			2.400	2.512
	Modal Power	0.597E-3	*	0.337E-3	0.205E-5	*	*	0.670E-4	0.986E-7
	Modal Power Ratio	1.250		1.292	0.723			0.916	0.0630
Upper Out of Plane (β_{+1}) (1.855 per rev)	Peak Frequency			1.320	1.320				2.512
	Modal Power	*	*	0.346E-4	-0.145E-4	*	*	*	-0.123E-6
	Modal Power Ratio			0.0722	-0.077				-0.0787
Wing Torsion (p) (1.344 per rev)	Peak Frequency	1.320	1.320	1.320	1.320		1.320	1.320	1.320
	Modal Power	0.102E-2	0.143E-2	0.259E-3	0.209E-3	*	0.322E-4	0.463E-3	0.730E-3
	Modal Power Ratio	0.873	0.995	0.539	1.119		1.002	0.988	0.975
Wing Chordwise (q_{w2}) (0.666 per rev)	Peak Frequency	0.661		0.661	0.724	0.7244		0.661	
	Modal Power	0.112E-1	*	0.567E-1	-0.240E-5	-0.461E-2	*	0.764E-4	*
	Modal Power Ratio	1.052		1.025	-0.173	-0.243		0.478	
Wing Vertical Bending (q_{w1}) (0.398 per rev)	Peak Frequency	0.398	0.398	0.398	0.398	0.7244	0.398	0.398	0.398
	Modal Power	0.343E-2	0.285E-2	0.316E-2	0.148E-2	-0.958E-3	0.297E-2	0.624E-3	0.383E-3
	Modal Power Ratio	1.179	1.030	0.577	1.168	-0.050	0.991	0.992	0.962
Lower Inplane (ζ_{-1}) (0.336 per rev)	Peak Frequency	0.398		0.398	0.398				
	Modal Power	-0.970E-3	*	0.368E-3	-0.188E-3	*	*	*	*
	Modal Power Ratio	-0.334		0.0671	-0.148				
Lower Out of Plane (β_{-1}) (0.176 per rev)	Peak Frequency	0.398		0.398					
	Modal Power	0.188E-3	*	0.313E-3	*	*	*	*	*
	Modal Power Ratio	0.0647		0.0570					

Table 3.2c

XV-15 Rotor/Cantilever Wing Modal Decomposition

MODE	TRANSFER FUNCTION PEAK QUALITY	TRANSFER FUNCTION					
		$\frac{q_{w1}}{\theta_{1c}}$	$\frac{q_{w1}}{\theta_{1S}}$	$\frac{q_{w2}}{\theta_{1c}}$	$\frac{q_{w2}}{\theta_{1S}}$	$\frac{p}{\theta_{1c}}$	$\frac{p}{\theta_{1S}}$
Coning (β_0) (2.555 per rev)	Peak Frequency	2.400	2.400	2.400	2.400		
	Modal Power	0.234E-6	0.286E-6	0.193E-5	0.254E-5	*	*
	Modal Power Ratio	0.349	0.383	0.0776	0.122		
Upper Inplane (ζ_{+1}) (2.434 per rev)	Peak Frequency	2.400	2.400	2.400	2.400	2.400	2.400
	Modal Power	0.291E-7	0.101E-6	0.244E-4	0.206E-4	0.559E-3	0.518E-3
	Modal Power Ratio	0.137	0.136	0.981	0.992	1.119	1.057
Upper Out of Plane (β_{+1}) (1.855 per rev)	Peak Frequency	2.400	2.400	1.585	1.259	2.400	2.400
	Modal Power	0.495E-6	0.466E-7	0.872E-6	0.153E-5	-0.159E-3	-0.190E-3
	Modal Power Ratio	0.736	0.0624	0.440	0.432	-0.319	-0.387
Wing Torsion (p) (1.344 per rev)	Peak Frequency	1.320	1.320	1.585	1.259	1.320	1.320
	Modal Power	0.246E-3	0.452E-3	-0.790E-6	0.169E-5	0.721E-2	0.134E-1
	Modal Power Ratio	1.123	1.074	-0.400	0.476	1.124	1.096
Wing Chordwise (q_{w2}) (0.666 per rev)	Peak Frequency			0.661	0.661		
	Modal Power	*	*	0.110E-3	0.523E-4	*	*
	Modal Power Ratio			1.024	1.092		
Wing Vertical Bending (q_{w1}) (0.398 per rev)	Peak Frequency	0.398	0.398			0.398	0.398
	Modal Power	0.310E-3	0.457E-3	*	*	0.279E-2	0.410E-2
	Modal Power Ratio	1.128	0.994			1.040	0.908
Lower Inplane (ζ_{-1}) (0.336 per rev)	Peak Frequency	0.398			0.380	0.398	0.398
	Modal Power	-0.183E-4	*	*	-0.935E-8	-0.233E-3	0.663E-3
	Modal Power Ratio	-0.0666			-0.075	-0.0868	0.147
Lower Out of Plane(β_{-1}) (0.176 per rev)	Peak Frequency				0.380	0.398	0.398
	Modal Power	*	*	*	-0.138E-6	-0.159E-3	-0.788E-3
	Modal Power Ratio				-1.113	-0.0592	-0.174

Thus, the table can be used in the following ways:

- Comparisons can be made horizontally of the modal power values for a desired mode to choose the transfer function giving the best information for that mode. This comparison can be made because the equations were normalized and the same frequency bandwidths were used.

- Comparisons of MPR can be made vertically to determine which peaks of a particular transfer function arise mostly from the resonance of a single mode and are least obscured by other modes.

Figures 3.1a and 3.1b are illustrative of the manner in which modal power ratio is used to evaluate system response. The wing chordwise acceleration to wing flaperon ($\ddot{q}_{w2}/\delta_f$) transfer function is shown in Figure C.2 (Appendix C). Four distinct peaks are evident. Figure 3.1a shows the modal power ratios for each of these peaks for contributors above 5% of the total power in the response. (Note that other degrees of freedom not shown are below 5% of the total power and sum with the plotted MPR's to unity.) The following Figure 3.1b shows the effect of additional control system lag beyond 5 Hz and the alterations in MPR associated with this lag.

The modal power ratio has even more utility when considering the coupled wing responses. This will be discussed in Chapter IV.

3.2 DISCUSSION OF TRANSFER FUNCTION CHARACTERISTICS

The primary modes of interest for XV-15 structural stability testing are those associated with the wing. For the purposes of this study, these modes include the wing vertical bending (q_{w1}), wing chordwise bending (q_{w2}), and wing torsion (p) modes. These

(a) Tilt rotor at 190 knots, first order control lag at 5 Hz, first order measurement at 100 Hz.

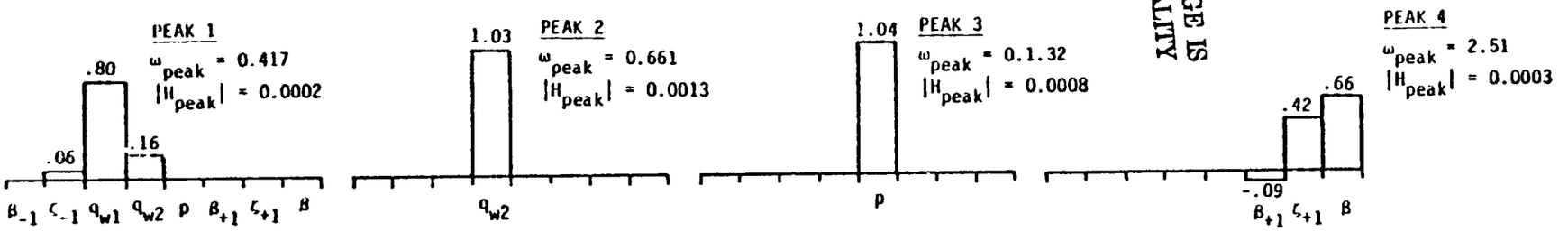

(b) Tilt rotor at 190 knots, fourth order control lag at 5 Hz, first order measurement at 100 Hz.

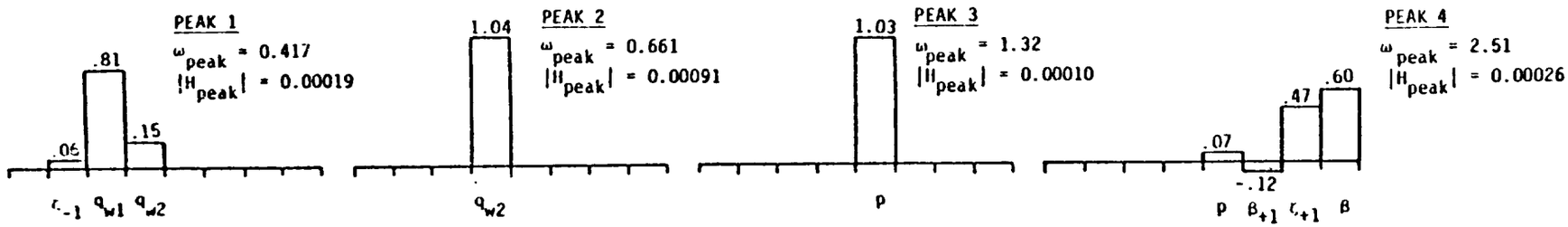

Figure 3.1 Modal Power Ratio; Wing Flaperon to Wing Chordwise Acceleration ($\ddot{q}_{w2}/\delta_f$), Cantilever Wing Transfer Function (Symmetric Motion)

modes are lightly damped and, therefore, of significant interest for flight test prediction.

In addition to the wing modes, there is another lightly damped mode whose response is important. This is the upper inplane mode, ζ_{+1}, although this mode is at a high frequency. These four modes are summarized with respect to frequency and damping in Table 3.3. The data in Table 3.3 is the "ideal" frequency and damping, based on an analysis of the characteristic equation. Stability parameters determined from various transfer functions will, in general, be different, as discussed below.

Of these four modes, further analysis was focused primarily on the q_{w1} and q_{w2} modes. The p mode has the greatest damping of the four at 0.058, and the analysis performed on the q_{w1} and q_{w2} modes

Table 3.3
Principal Symmetric Modes

MODE	w_D	ζ
ζ_{+1}	2.43 Per Rev (18.6 Hz)	0.02990
p	1.34 Per Rev (10.3 Hz)	0.05783
q_{w2}	0.666 Per Rev (5.09 Hz)	0.04258
q_{w1}	0.398 Per Rev (3.04 Hz)	0.04798

can be easily extended to the higher two modes when consideration of control excitation at their frequencies is desired (p at 10.3 Hz and ζ_{+1} at 18.6 Hz).

Observations about the transfer functions are made here primarily to point out modes <u>not</u> available in the wing bending transfer functions from instrumentation presently planned for the XV-15 ($\ddot{q}_{w1}/\delta_f$ and $\ddot{q}_{w2}/\theta_o$ are presently available). For example, it is difficult to obtain information on the upper inplane mode. Direct measurements of the inplane motion show a resonant peak in the frequency vicinity of the upper inplane mode (ζ_{+1}). However, the rotor coning mode (β) is very close to this frequency. Excitation of the inplane degrees of freedom by collective gives a response with magnitude 10^{-1}, but the collective also excites the β mode considerably (see Table 3.2). Excitation of the inplane degrees of freedom by the flaperon does not excite the β mode significantly; however, the resonant peak has a magnitude of only 10^{-2}. Cyclic inputs would excite the ζ_{+1} mode sufficiently without significant participation of the β mode. Resonant peaks with good information on the ζ_{+1} mode occur in the transfer functions of wing torsion (p) and rotor inplane motion ($\beta_{1C}^{(1)}$ and $\beta_{1S}^{(1)}$) to cyclic inputs (θ_{1C} and θ_{1S}). Thus, by measuring wing torsion, it would not be necessary to add strain gauges on the rotor blades to measure the ζ_{+1} mode.

Collective pitch to the rotor coning degree of freedom does not show sharply distinguished resonances for modal decomposition. Excitation of this degree of freedom with wing flaperon does show resonance; however, the β_{+1} mode corrupts the ζ_{+1} considerably (see Table 3.2). Also, this peak is rather small in magnitude (10^{-3}), again indicating that a rotor blade measurement would not add to the information available from present instrumentation.

Gimbal measurements excited by flaperon (δ_f) give no additional modes. Collective pitch (θ_o) does excite the ζ_{+1} mode; however, it is corrupted somewhat by the β mode (see Table 3.2). The rotor azimuth perturbation transfer functions give no additional modes.

Of the wing bending measurements presently instrumented on the XV-15, investigation of the cross transfer functions shows that $\ddot{q}_{w2}/\delta_f$ is quite attenuated, with peaks at a magnitude of 10^{-3} or below. However, $\ddot{q}_{w1}/\theta_o$ is actually more desirable than $\ddot{q}_{w1}/\delta_f$ for identifying the q_{w1} mode, showing a greater magnitude, greater modal power and also a greater modal power ratio (Table 3.2). Both measurements, $\ddot{q}_{w1}$ and $\ddot{q}_{w2}$, will be recorded when either θ_o or δ_f is excited. Obtaining the cross transfer functions ($\ddot{q}_{w1}/\theta_o$ or $\ddot{q}_{w2}/\delta_f$) is merely a matter of additional data processing. For identifying the damping of the q_1 mode, the estimates from the $\ddot{q}_{w1}/\delta_f$ and $\ddot{q}_{w1}/\theta_o$ transfer functions can be combined to give an improved estimate. The $\ddot{q}_{w1}/\delta_f$ transfer function can be used to identify the p mode. (There are other transfer functions where the p mode is excited more such as the gimbal angle, inplane bending, and torsion transfer functions, but these require additional instrumentation.) The $\ddot{q}_{w2}/\theta_o$ transfer function can be used to identify the β mode (given that the control system could be excited at this high frequency: 19.5 Hz). As with the p mode, the β mode could be identified from other transfer functions by adding measurements. The wing bending measurements excited with cyclic yield no additional modes (ζ_{+1} and β mode obscure each other).

Torsion measurements excited by either collective pitch or wing flaperon give no additional modes. The significant observation about a torsion measurement, however, is that the upper inplane mode ζ_{+1} can be identified with excitation by cyclic pitch (if the control system could be excited at this frequency: 18.6 Hz). A torsion measurement could be obtained from linear combinations of vertically aligned accelerometers on the fore and aft ends of the

pylon. This instrumentation would be much easier than adding a strain gauge to the rotor blades and passing the signal through a commutator at the rotor hub.

3.3 INPUT FREQUENCY REQUIREMENT

The overall system transfer function analysis of Sections 3.1 and 3.2 is now specialized to analysis of the wing transfer functions. From the results of Tables 3.1 and 3.2, wing response transfer functions are isolated which would give the best information about particular degrees of freedom.

The damping of modes from particular transfer functions is now presented from the frequency response data plotted in Figures C.1 to C.12. The method used is that suggested by Johnson in Ref. 6, Appendix E. A detailed derivation and explanation of the method is included in Appendix B of this report.

Table 3.4 shows the damping factors calculated for each mode using this method. The transfer function was selected using the modal power as a criterion. The table includes the effects of two different control lags--a first order and a fourth order lag--both with a bandwidth of 5 Hz. It is seen that, with existing wing input channels, wide band input frequencies can be used to isolate coning (β_o), upper blade out-of-plane (β_{+1}) and inplane (ζ_{+1}) modes, and wing torsion. Only wing vertical bending and chordwise bending can be excited with a one/rev limit on θ_o and δ_f. Note that the ζ_{+1} mode could be excited by a cyclic input (although at a high input frequency).

The calculation of the dampings of Table 3.4 was achieved by integrating over the frequency band 0.9 ω_n to 1.1 ω_n, where ω_n is the peak frequency. Damping obtained by this method was found very sensitive to this frequency band. A wider band, 0.8 ω_n - 1.2 ω_n was found too wide, introducing other modes and degrading the damp-

Table 3.4
Calculated Damping Values

MODE	TRANSFER FUNCTION SELECTED	FREQ. RANGE (PER REV)	MODELED VALUE OF ζ	FIRST ORDER CONTROL LAG AT 5 HERTZ			FOURTH ORDER CONTROL LAG AT 5 HERTZ		
				COMPUTED VALUE OF ζ	$\lvert H_{PEAK} \rvert$ NORMALIZED	MODAL POWER RATIO	COMPUTED VALUE OF ζ	$\lvert H_{PEAK} \rvert$ NORMALIZED	MODAL POWER RATIO
β_o	$\ddot{q}_{w_2}/\theta_o$	(2.19) (2.89)	0.0817	0.0785	0.338E-1	1.028	0.0708	0.599E-3	0.996
ζ_{+1}	p/θ_{1c}	(2.09) (2.81)	0.0299	0.0157	0.484E-1	1.119	0.0159	0.983E-3	1.098
β_{+1}	NONE	---	---	---	---	---	---	---	---
p	$\ddot{q}_{w_1}/\delta_f$	(1.15) (2.09)	0.0578	0.0559	0.122E-1	0.950	0.0506	0.137E-2	1.028
q_{w2}	$\ddot{q}_{w_2}/\theta_o$	(0.55) (0.84)	0.0426	0.0374	0.189	1.020	0.0277	0.132	1.028
q_{w1}	$\ddot{q}_{w_1}/\delta_f$	(0.33) (0.48)	0.0480	0.0444	0.316E-1	1.005	0.0363	0.308E-1	1.006
ζ_{-1}	NONE	---	---	---	---	---	---	---	---
β_{-1}	NONE	---	---	---	---	---	---	---	---

ing to 50% of the theoretical value for the q_{w1} and q_{w2} modes. Reducing the frequency bandwidth to the half-power value of 0.95 ω_n-1.05 ω_n further showed a degraded accuracy.

The response conclusions based on the transfer functions apply principally to input and measurement frequency requirements. Amplitude specifications for inputs and instrumentation are based on actuator and sensor limits not fully available at this time, but easily determined from the transfer functions of Appendix C. An important additional source of input requirement arises from the consideration of tunnel induced turbulence, discussed in the following Section 3.4.

3.4 THE EFFECT OF NOISE IN SELECTING INPUT AMPLITUDES

Having selected the transfer functions to identify the primary modes on a deterministic basis, we now address the effect of random disturbances in the wind tunnel in further specifying input amplitudes. There are two questions of interest here:

(1) What is the responsiveness (or susceptibility to disturbance) of a particular measurement to random gusts?

(2) Given a particular measurement excited by a particular input, what input magnitude is required to achieve a desired signal-to-noise ratio (SNR), or, alternately, minimize a noise-to-signal ratio (NSR)?

These questions can be answered by considering the model of the XV-15 dynamics

$$\dot{\underline{x}} = F\underline{x} + G\underline{u} + \Gamma\underline{v}$$

$$\underline{y} = H\underline{x} + D\underline{u}$$

We have been considering the steady state response to control excitation

$$y(j\omega) = [H(j\omega I - F)^{-1}G + D]\, u(j\omega)$$

The resulting Bode plot can be used to predict the magnitude and phase of the response to sinusoidal excitation (a discrete frequency) or band limited random excitation in a frequency range of interest. For example, the entire Bode plot would be the response to excitation of all frequencies in the range of the Bode plot or white noise limited to this range. Thus, we can consider random excitation in any frequency band; and, specifically, we can consider random excitation in the vicinity of a peak of interest.

It may be shown (Appendix B.2.3), that the noise-to-signal ratio in a frequency band $\omega_2 - \omega_1$ can be written

$$\frac{N}{S} = \frac{qX_n}{u_{rms}^2 X_s} + \frac{r(\omega_2 - \omega_1)}{u_{rms}^2 X_s} \qquad (3.1)$$

where

X_n is the noise power in the frequency band

X_s is the equivalent power from a sinusoidal signal in the same frequency band

q is the gust power spectral density

r is the measurement noise power spectral density

u_{rms} is the root-mean-square value of the input

The second term of this equation is negligible compared to high speed wind tunnel turbulence, and may be neglected. (Note that the effect of measurement noise can be simply added.)

Plots for the selected transfer functions of NSR, as a function of the rms input amplitude, are plotted as families of curves parameterized on the rms velocity of the gust in the wind tunnel and on the control actuator bandwidth (Figures 3.2 through 3.7). The results are presented for two cases.

(1) First order lagged control with the Dryden wind gust model (see Section 2.4).

(2) Fourth order lagged control with the Dryden wind gust model.

Two general observations are evident in the NSR plots (Figures 3.2-3.7). First, the 2 Hz control bandwidth case shows a greater deviation from the base case of 5 Hz than the 10 Hz control bandwidth case. This is to be expected since the 5 Hz break frequency is close to the upper limit of the wing modes under consideration, while the 2 Hz break frequency is completely below them. Second, the fourth order lagged control system makes the break frequency more significant, and indicates a significant increase in rms amplitude to achieve a desired NSR for a mode above the break frequency.

An example use of these charts is as follows. To achieve a NSR between 0.1 and 0.2 for the $\ddot{q}_{w2}/\theta_o$ transfer function when the expected total rms wind tunnel gust is 10 ft/sec, the following collective pitch input would be required:

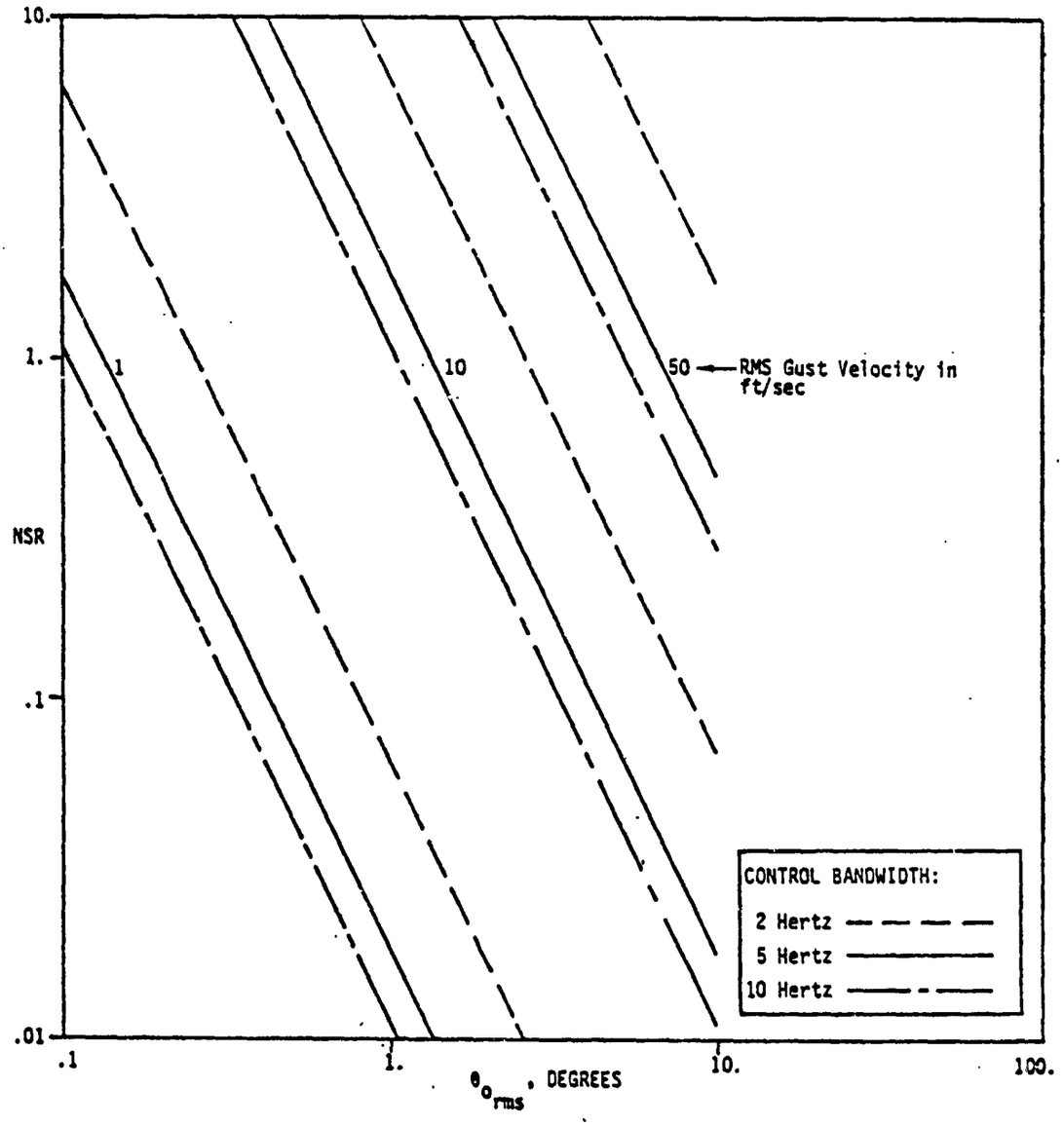

Figure 3.2 Noise-to-Signal Ratio--Collective Pitch to Wing Chordwise Acceleration ($\ddot{q}_{w2}/\theta_o$); Cantilever Wing Transfer Function (For Frequency Range 4.20 to 6.35 Hz)

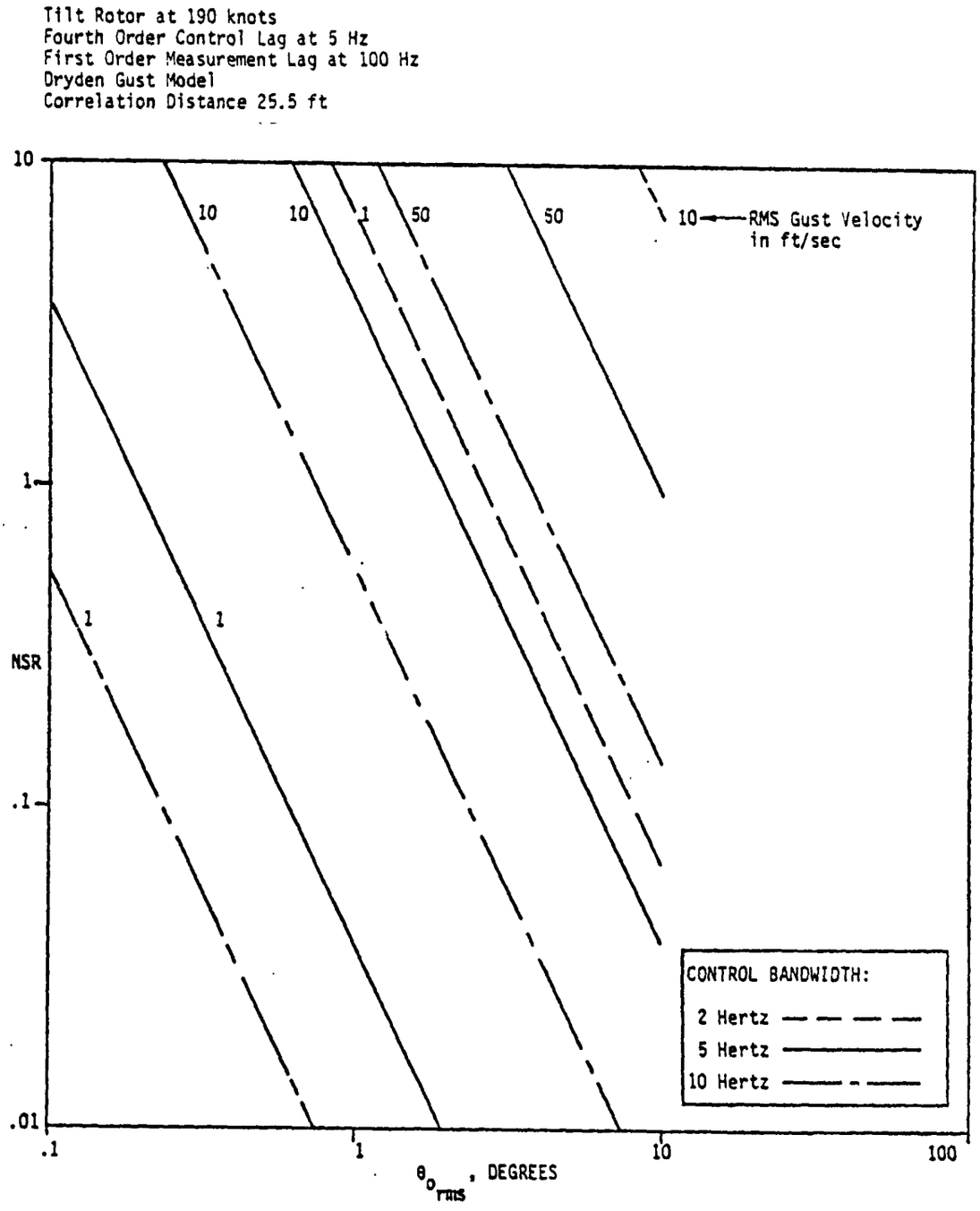

Figure 3.3 Noise-to-Signal Ratio--Collective Pitch to Wing Chordwise Acceleration ($\ddot{q}_{w2}/\theta_o$); Cantilever Wing Transfer Function (For Frequency Range 4.20 to 6.35 Hz)

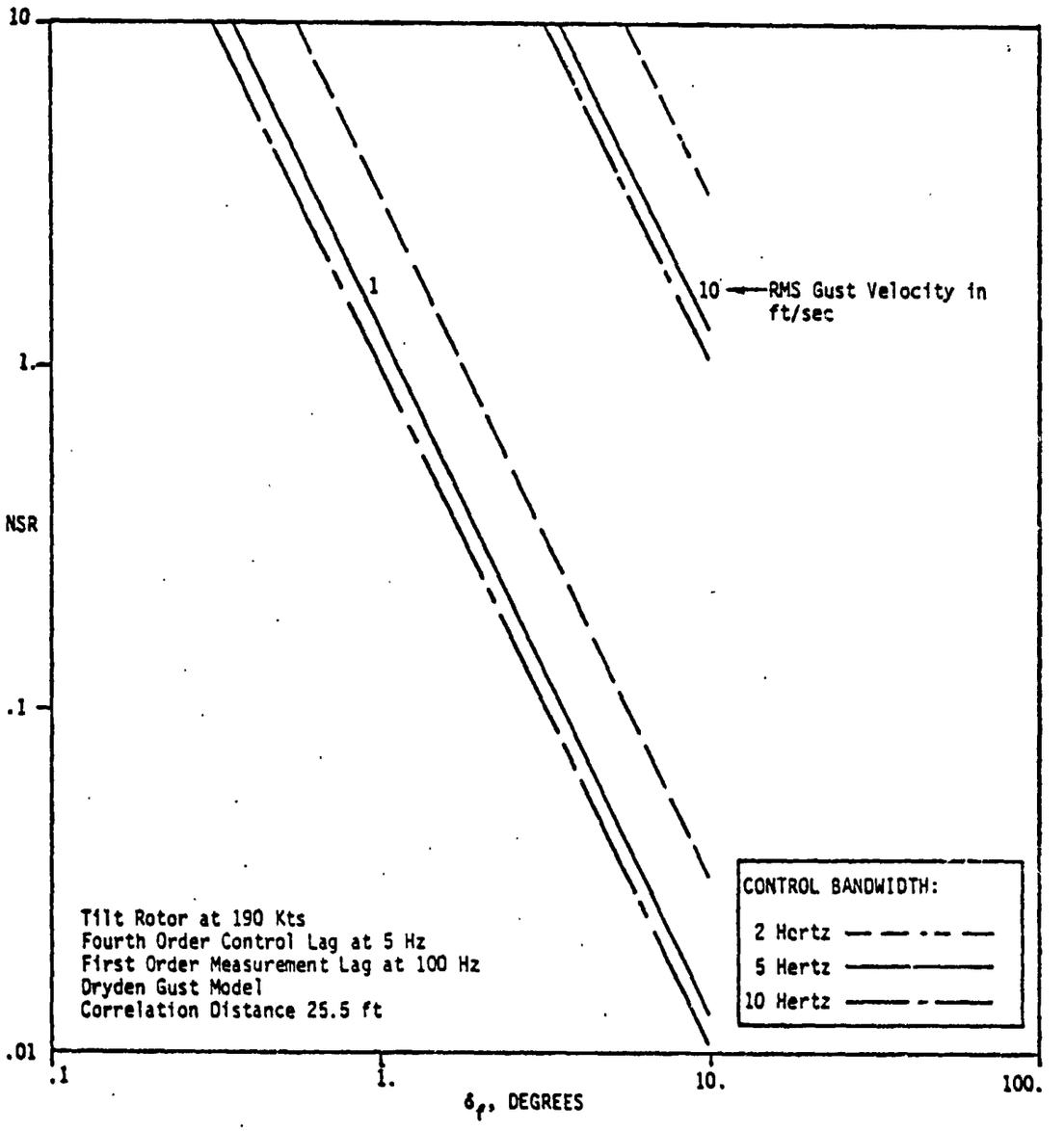

Figure 3.4 Noise-to-Signal Ratio--Wing Flaperon to Wing Vertical Acceleration ($\ddot{q}_{w1}/\delta_f$); Cantilever Wing Transfer Function (For Frequency Range 3.04 to 4.60 Hz)

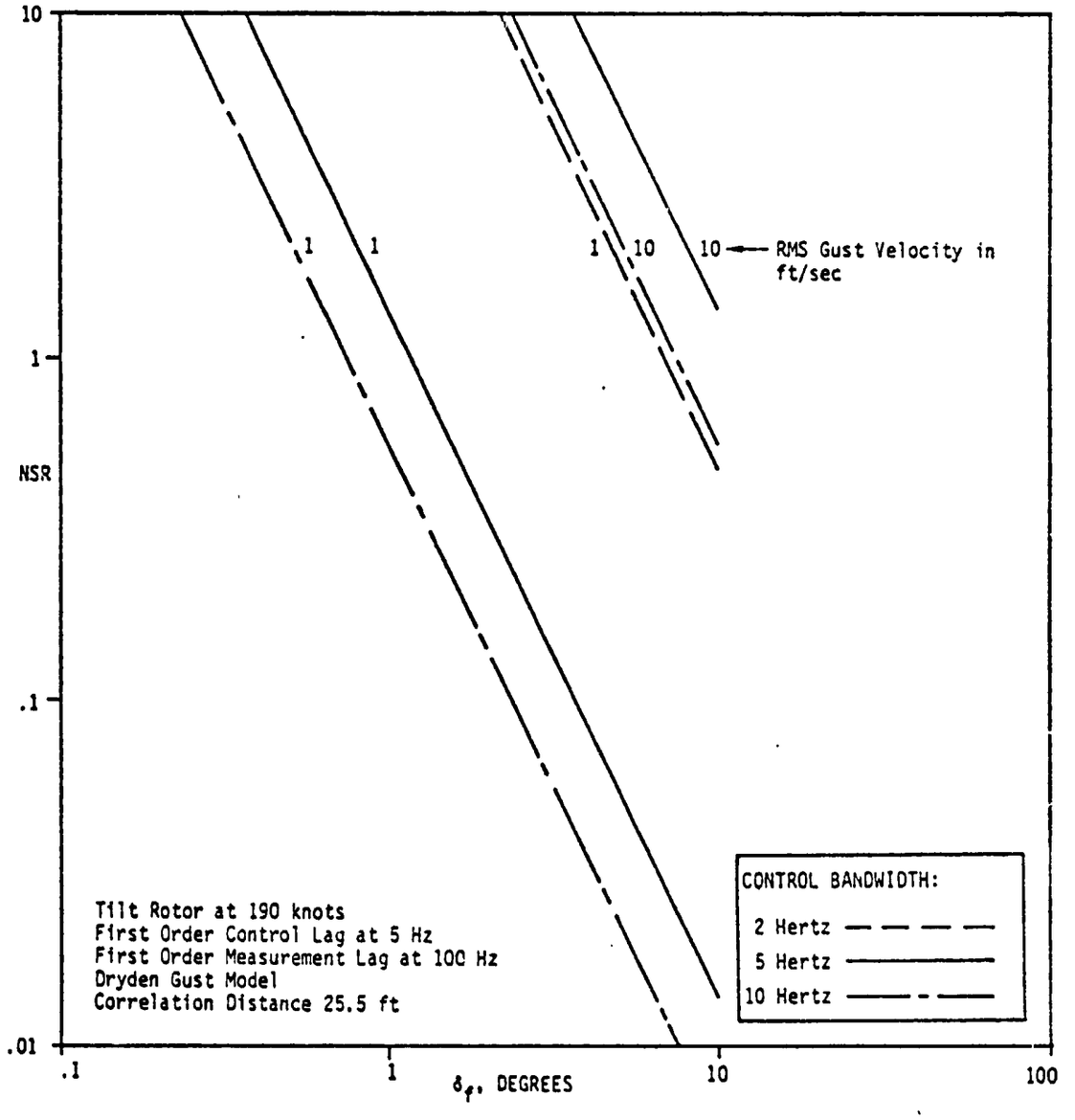

Figure 3.5 Noise-to-Signal Ratio--Wing Flaperon to Wing Vertical Acceleration ($\ddot{q}_{w1}/\delta_f$); Cantilever Wing Transfer Function (For Frequency Range 3.04 to 4.60 Hz)

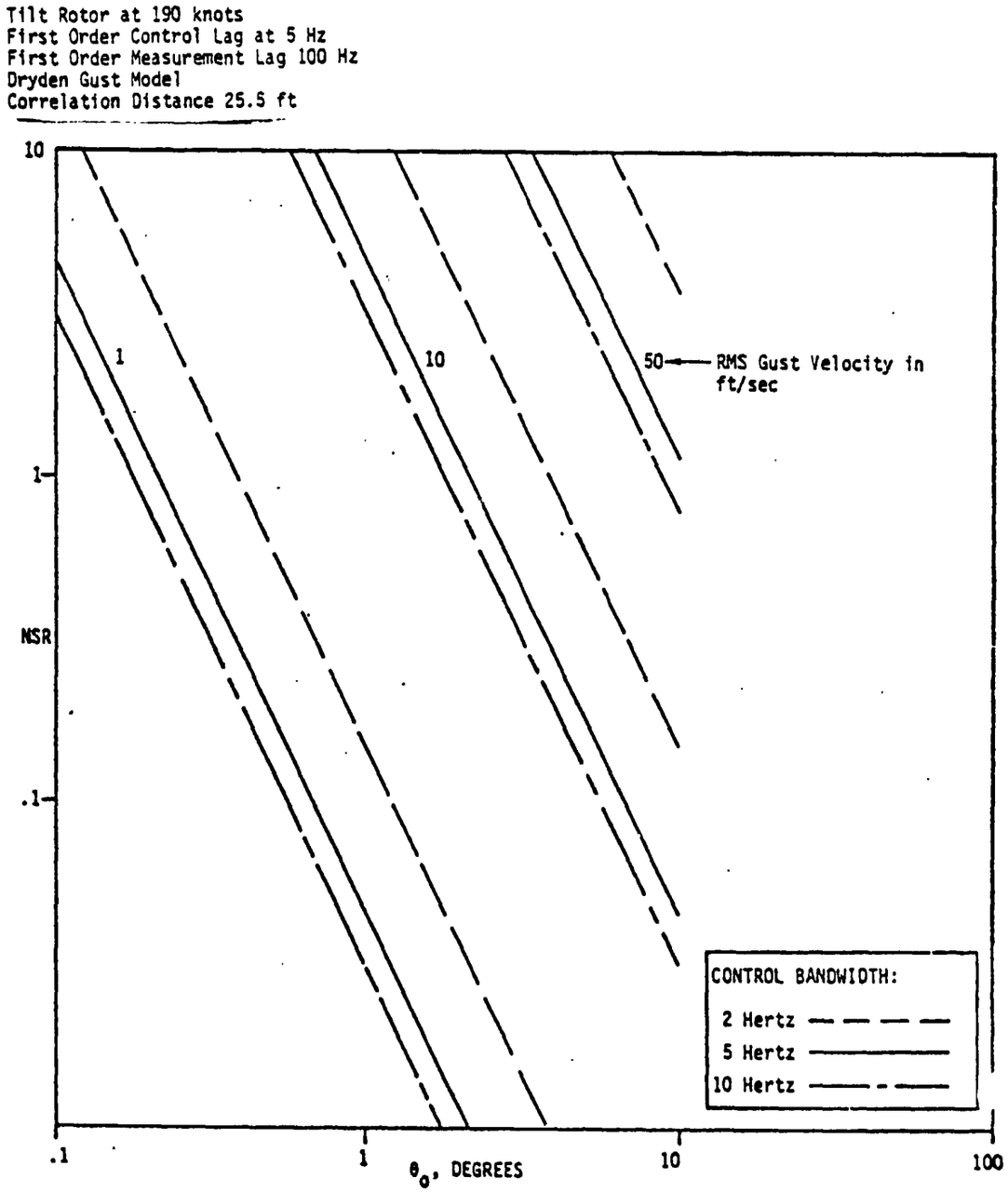

Figure 3.6 Noise-to-Signal Ratio--Collective Pitch to Wing Vertical Acceleration ($\ddot{q}_{w1}/\theta_o$); Transfer Function for Asymmetric Motion (For Frequency Range 3.33 to 5.29 Hz)

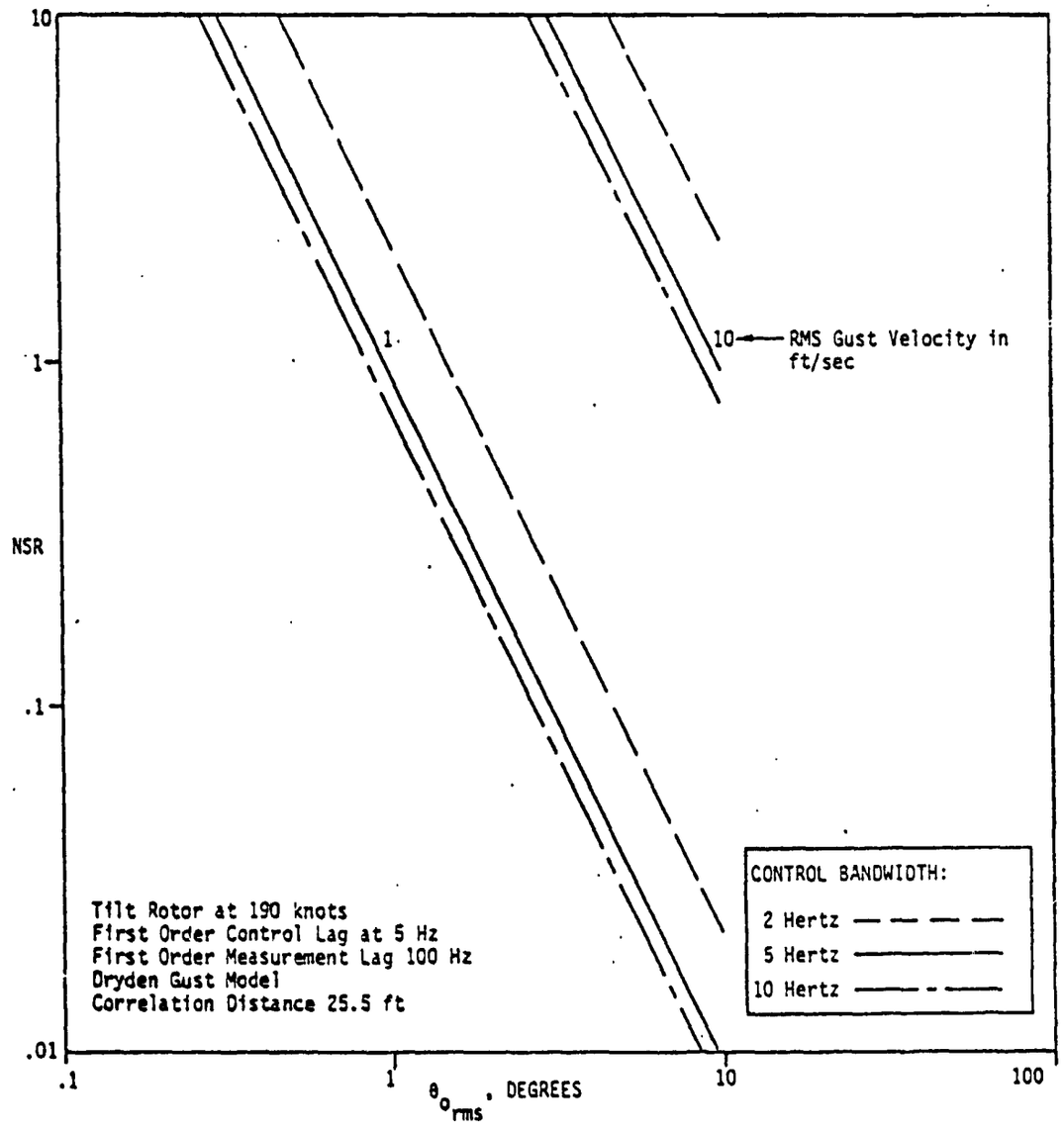

Figure 3.7 Noise-to-Signal Ratio--Collective Pitch to Wing Vertical Acceleration ($\ddot{q}_{wl}/\theta_o$); Transfer Function for Symmetric Motion (For Frequency Range 2.77 to 3.49 Hz)

CONTROL BANDWIDTH (HERTZ)	INPUT AMPLITUDE IN DEGREES - RMS (FIRST ORDER LAG IN CONTROL)
2	5.80 - 8.10
5	2.97 - 4.20
10	2.31 - 3.30

(From Figure 3.2)

The NSR plots can be used in the following manner (neglecting measurement noise):

(1) A range of acceptable SNR's and, hence, NSR's, and a range of expected rms longitudinal gust should be selected.

(2) The corresponding limiting upper and lower rms input amplitudes from the NSR plots give the required amplitude to achieve the desired SNR.

(3) These values should be determined for the first order lagged control model and the fourth order lagged model (at the desired break frequency) to give a best and worst case (as discussed in Section 2.6).

3.5 SUMMARY

This section has presented the results of a detailed study of a model of XV-15 rotor/cantilever wing dynamics at 190 knots. The objectives of this study have been the following:

(1) Calculation of transfer functions from the two principal controls (collective and flaperon) to the nine degrees-of-freedom of the model.

(2) Ranking of the transfer functions with respect to their utility in isolating principal modes, and input frequency bandwidth requirements.

(3) Quantification of the effects of tunnel noise on required input amplitudes.

It is concluded that the principal limitation to mode isolation for the nine degree-of-freedom model is input bandwidth. Instrumentation of the wing is sufficient to identify all but the ζ_{+1} and lower (-1) rotor modes if collective and flaperon input channels are used. To identify the ζ_{+1} mode, measurements of wing torsion excited by longitudinal cyclic would be effective. In all cases, however, input frequencies required to identify the upper (+1) rotor modes and wing torsion mode are above 1 per rev. The lower (-1) rotor modes are not identifiable with wing instrumentation because they are heavily damped and obscured by other modes.

Evaluations of the quality of transfer functions from this nine degree-of-freedom model are based on a control system bandwidth of 5 Hz. A first order and fourth order lag were used with this bandwidth. The principal effect of increased control system rolloff beyond 5 Hz is increase in input amplitude required to achieve an adequate noise-to-signal ratio of output data. Input amplitudes required to achieve a desired noise-to-signal ratio for different levels of wind gust were determined for a control system bandwidth of 2, 5, and 10 Hz.

IV. COUPLED WING DYNAMICS

This section presents the analytical evaluation of the coupled wing dynamics. Section 4.1 discusses the frequency response for the measurements presently available (both wing bending accelerations) excited by collective pitch and wing flaperon. Section 4.2 summarizes the modeling of calibration errors in measurement and excitation and discusses the results. Section 4.3 presents the effect of tunnel-induced random disturbances and the input amplitudes and frequency ranges which are required to identify principal modes of interest with particular noise-to-signal ratios.

4.1 FREQUENCY RESPONSE OF THE COUPLED WING MODEL

4.1.1 Computation of Coupled Wing Responses

The discussion of the coupled wing model will be limited to the $\ddot{q}_{w1}/\delta_f$ and $\ddot{q}_{w2}/\theta_o$ transfer functions for identification of the following modes:

q_{1S}: symmetric vertical wing bending mode

q_{1A}: asymmetric vertical wing bending mode

q_{2S}: symmetric chordwise bending mode

q_{2A}: asymmetric chordwise bending mode

As discussed in Section 2.3, the response of the right wing by excitation of the right wing has a symmetric and an asymmetric portion. Excitation of a wing, and measurement of that wing, is not sufficient to separate the symmetric and asymmetric coupled wing modes if they are "close in fre[illegible]." As discussed in Section 2.3 and again in Section 4.2, additional instrumentation makes it possible to separate the symmetric and asymmetric frequency

responses, except for some fraction of the opposite motion (asymmetric or symmetric) due to calibration errors.

The nine degree-of-freedom rotor/cantilever wing model can be used to analyze the coupled wing (e.g., right and left wing coupled modes) in the following manner:

(1) compute the symmetric transfer function, $T_S(j\omega)$, from the linear equations representing the symmetric motion;

(2) compute the asymmetric transfer function, $T_A(j\omega)$, similarly, and

(3) combine these transfer functions at discrete values of the frequency, ω, by the formula

$$T(j\omega) = \frac{1}{2} [T_S(j\omega) + T_A(j\omega)] \quad . \quad . \quad . \quad .$$

Because this new transfer function T now has twice as many modes in the same frequency range, more pronounced modal coupling occurs in a small frequency range and the phase may appear to be discontinuous (Appendix B.2.1). However, if a sufficiently small frequency increment were used, it would show the phase to be continuous, since both transfer functions are analytic.

Clearly, the coupled wing motion will exhibit characteristics of both the symmetric and asymmetric motions. The characteristics of the symmetric transfer functions were discussed in some detail in the previous chapter. Before continuing the discussion of the coupled wing motion, the characteristics of asymmetric motion will be presented briefly.

4.1.2 Asymmetric Mode Characteristics

The principal asymmetric modes are listed in Table 4.1. The asymmetric frequency responses for the wing bending accelerations are shown in Appendix C (Figures C.25 to C.28).

The linear model for the asymmetric motion differs from the symmetric motions in that the coupling due to the drive shaft between the two rotors introduces an oscillatory mode associated with the rotor speed perturbation. The wing stiffnesses, associated with the two asymmetric wing bending degrees of freedom, were increased to shift the q_{1A} and q_{2A} modes up in frequency from the q_{1S} and q_{2S} modes in order to distinguish them. The q_{2A} mode was shifted up such that it was almost coincident with the ζ_{cA} mode (the rotor speed perturbation mode). This was considered one type of worst case for analyzing the effect of the asymmetric mode on measured frequency and damping.

Table 4.1
Principal Asymmetric Modes

MODE	DAMPED FREQUENCY ω_D	DAMPING FACTOR ζ
ζ_{+1}	2.44 Per Rev 18.6 Hz	0.02978
p	1.42 Per Rev 10.8 Hz	0.05382
q_{w2}	0.727 Per Rev 5.55 Hz	0.02124
q_{w1}	0.562 Per Rev 4.29 Hz	0.05543

4.1.3 Coupled Wing Mode Characteristics

The transfer functions for the coupled wing responses are calculated from the plots presented in Appendix C. For the two principal modes of most interest, q_{w1} and q_{w2}, the q_{1S} and q_{1A} modes are practically unobscured and the q_{2S} and q_{2A} modes are obscured to a moderate and greater extent, respectively. This illustrates both extremes which can occur in the actual dynamics of the XV-15.

The $\ddot{q}_{w2}/\theta_o$ transfer function shows a prominent resonant peak for q_{2S} (at 0.66 per rev), but the q_{2A} mode (at 0.72 per rev) shows no resonant peak at all. It is obscured by the q_{2S} and ζ_{oA} modes. The q_{2S} peak itself is obscured somewhat by the ζ_{oA} mode (at 0.73 per rev), as is shown by the modal power ratio (MPR) in Figure 4.1. The symmetric and asymmetric flapping modes β_S and β_A are very close in frequency (β_S = 2.55 and β_A = 2.61 per rev), and although they are not principal modes, it is interesting to note their equal contributions to the second resonant peak on tl $\ddot{q}_{w2}/\theta_o$ transfer function from the MPR shown in Figure 4.1. Because the symmetric and asymmetric β modes result in a single resonant peak, these modes cannot be distinguished in this transfer function, which illustrates the value of being able to separate the symmetric and asymmetric motions.

The $\ddot{q}_{w1}/\delta_f$ transfer function shows distinct resonant peaks for the q_{1S} and q_{1A} modes and one resonant peak where the two torsion modes occur (p_S at 1.34 and p_A at 1.417 per rev). The MPR's for this transfer function, which are shown in Figure 4.2, indicate that q_{1S} is unobscured and that q_{1A} is slightly obscured by q_{1S}. The torsion modes obscure each other in the third peak as expected. The modal power ratio for collective pitch to wing vertical bending acceleration ($\ddot{q}_{w1}/\theta_o$) with coupled wing motion is shown in Figure 4.3.

At this point, it must be concluded that the difficulties with the coupled wing model are as follows:

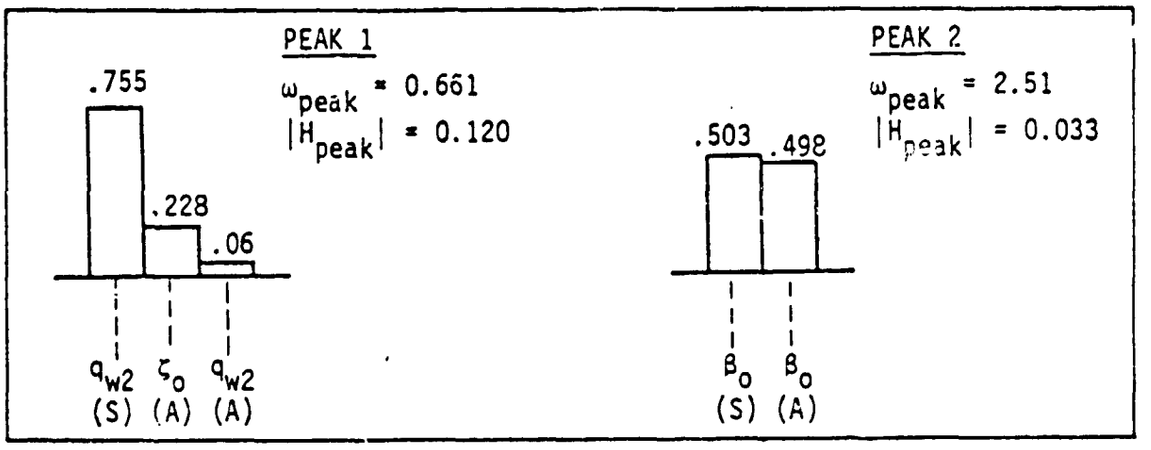

Figure 4.1 Modal Power Ratio (MPR)--Collective Pitch to Wing Chordwise Acceleration ($\ddot{q}_{w2}/\theta_o$); Coupled Wing Motion

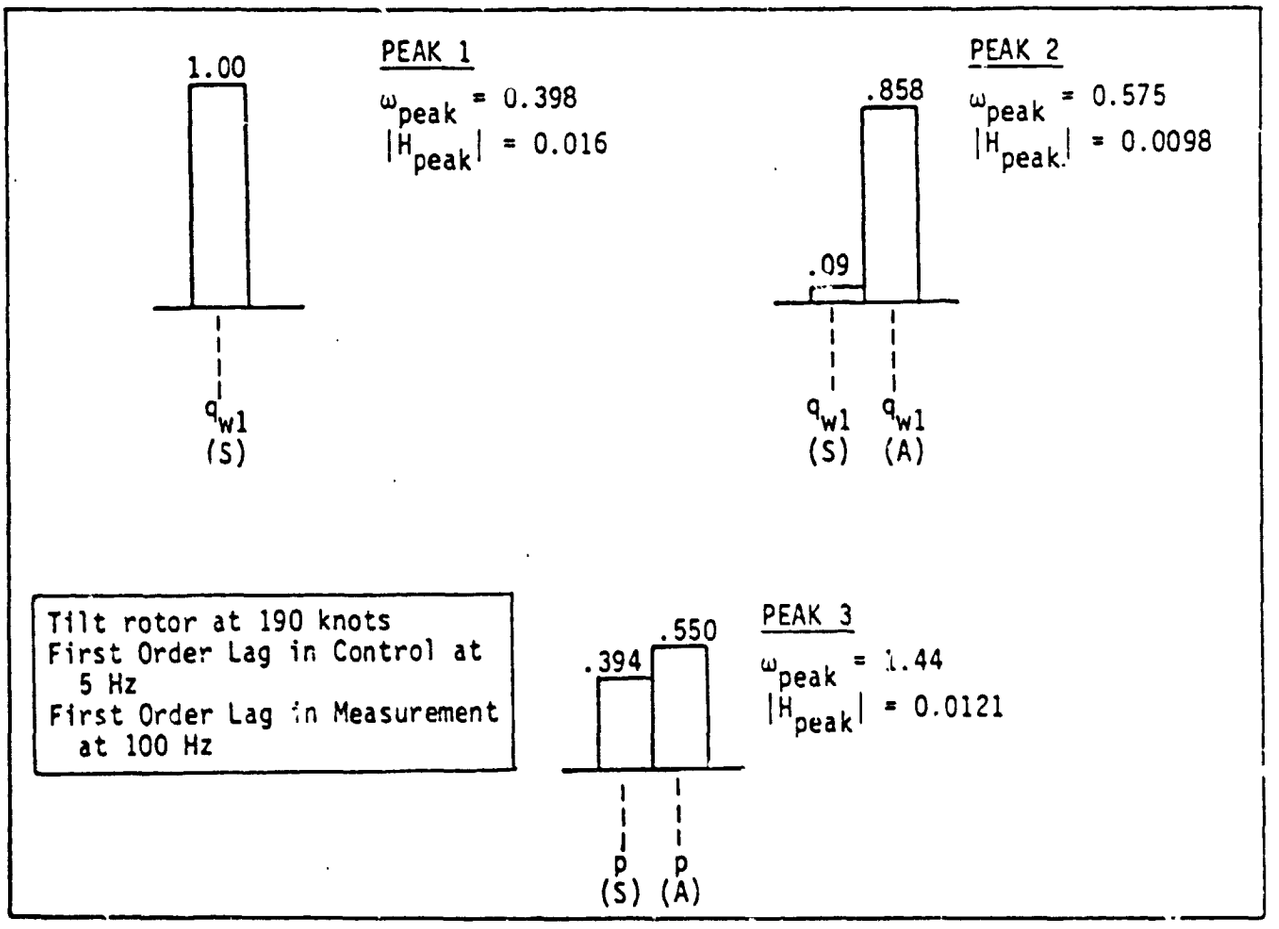

Figure 4.2 Modal Power Ratio (MPR)--Wing Flaperon to Wing Vertical Bending Acceleration ($\ddot{q}_{w1}/\delta_f$); Coupled Wing Motion

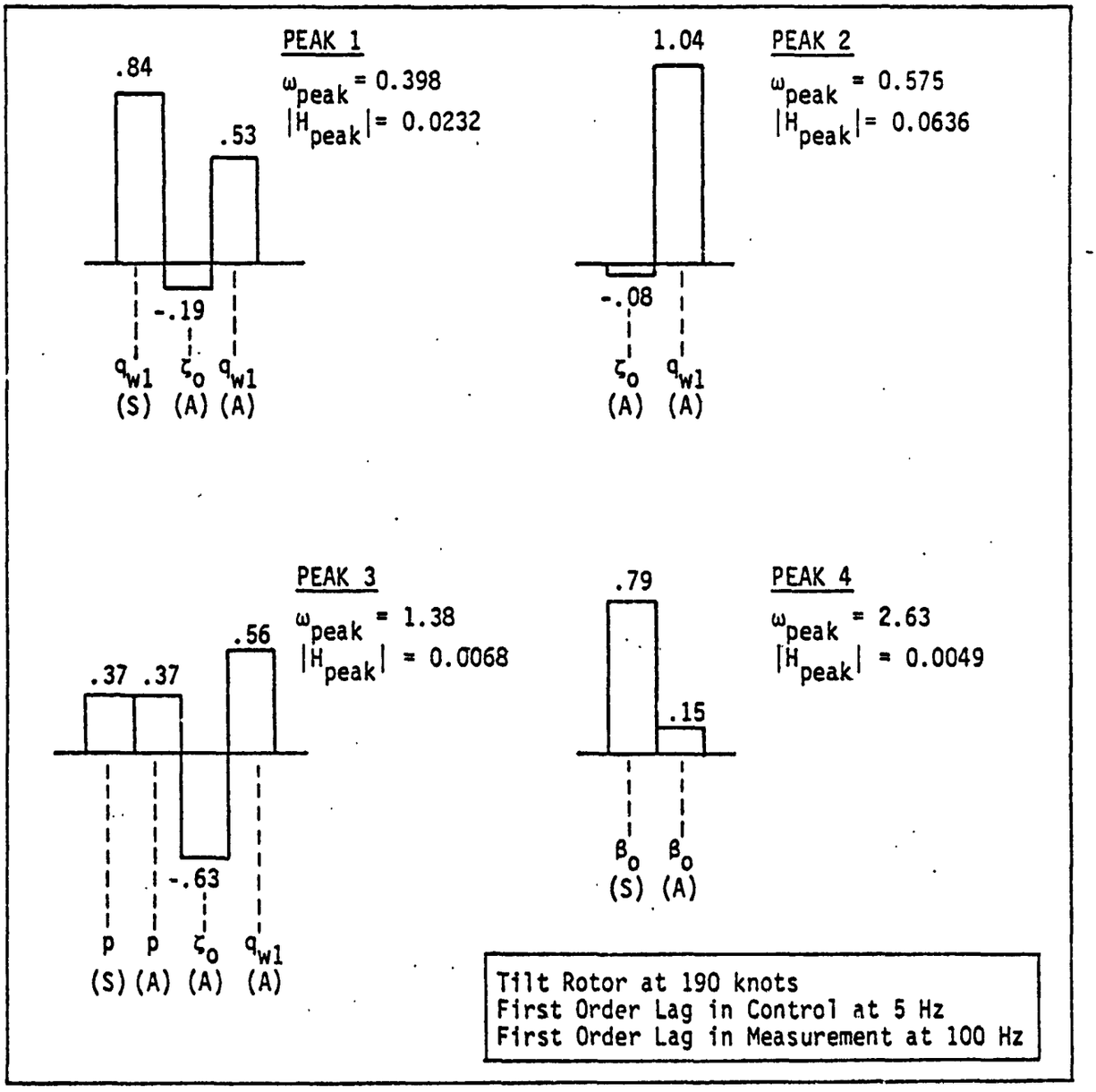

Figure 4.3 Modal Power Ratio (MPR)--Wing Vertical Bending Acceleration to Collective Pitch ($\ddot{q}_{w1}/\theta_o$); Coupled Wing Motion

(1) There are so many modes in the same frequency region that it is difficult to determine whether a particular resonant peak is due to symmetric or asymmetric motion (i.e., due to the excitation of the wing which is being measured, or the reaction force of the rest of the aircraft on the wing being measured).

(2) Even more importantly, given a particular resonant peak on the frequency response, one does not know how many, which one, or how much other modes are contributing to that peak. The modeled dynamics used in this analysis show examples where some principal modes are obscured and others are not. The measured dynamics of the XV-15 could be better or worse, but the significant point is that one will not be able to determine this unless the symmetric and asymmetric motions are separated. It is important to know whether a principal mode is obscured or not and to know how much. The damping calculated from a resonant peak could show the XV-15 to be quite stable, when in fact there are two or more modes contributing to this peak, one of which is safely stable, but another of which has very light damping that could become unstable in some flight conditions.

4.2 EVALUATION OF CALIBRATION ERRORS

The approach for modeling calibration errors for various wind tunnel test configurations (e.g., excite one wing and measure one wing, or excite one wing and measure both wings, etc.) is developed in Section 2.3. In this section, three test configurations are considered in detail to assess the effect of unwanted modes on the damping estimates of desired modes. The three cases are:

(1) the present test configuration (excite one wing and measure that wing);

(2) An improved test configuration which will separate symmetric and asymmetric motion (excite one wing and measure both wings); and

(3) the most accurate test configuration for separating symmetric and asummetric motion (excite both wings and measure both wings).

For each configuration, the actual environment is considered; that is, calibration errors in both measurements and controls are modeled.

First consider the effect of calibration errors in both measurement and control of the present test configuration. The notation of Section 2.3 is used here except that functional dependence on the Laplace complex variable s is not shown explicitly. The measured response of the right wing is

$$y_{R_m} = (1 + \eta_R)\, y_{R_a}$$

where η_R is the measurement calibration error and the actual response of the right wing is

$$y_{R_a} = T_S\, u_{S_a} + T_A u_{A_a}$$

Thus,

$$y_{R_m} = (1 + \eta_R)[T_S u_{S_a} + T_A u_{A_a}]$$

$$y_{R_a} = T_S \left\{ \frac{1}{2} \left[u_{R_m}(1 + \varepsilon_R) + u_{L_m}(1 + \varepsilon_L) \right] \right\}$$

$$+ T_A \left\{ \frac{1}{2} \left[u_{R_m}(1 + \varepsilon_R) - u_{L_m}(1 + \varepsilon_L) \right] \right\}$$

where ϵ_R and ϵ_L are the control calibration errors.

$$\frac{y_{R_m}}{u_{R_m}} = \frac{1}{2}(1 + \eta_R)(1 + \epsilon_R)[T_S + T_A]$$

$$= [1 + \epsilon_R + \eta_R + \eta_R \epsilon_R] \frac{1}{2} [T_S + T_A]$$

Thus, calibration errors in both excitation and measurement for the present configuration have the effect of scaling the measured transfer function by a gain factor, which does not affect the determination of the resonant peak frequencies. This gain factor also does not affect the damping calculation because the square of the gain enters in both the numerator and denominator and, therefore, cancels out.

Thus, for the present wind tunnel test configuration, calibration errors have a negligible effect in the calculation of the frequency and damping associated with a particular resonant peak on the frequency response. However, the difficulty with the present test configuration, as discussed in the previous section, is that the symmetric and asymmetric modes obscure each other, making the determination of the damping of principal modes for assessing the dynamic stability of the XV-15 ineffective.

Therefore, it is very desirable to separate the symmetric and asymmetric motion to determine with confidence which modes are present in the resonant peaks of the frequency response. This can be accomplished in three ways, as discussed in Section 2.3:

(1) Measure both wings exciting one wing.

(2) Measure one wing exciting both wings.

(3) Measure both wings exciting both wings.

It will be shown later that the third alternative, although it involves more test equipment and, hence, more cost, actually reduces the effect of calibration errors to a negligible level. The first alternative will be considered here since it is the easiest to implement.

Again, using the notation of Section 2.3,

$$y_{S_m} = \frac{1}{2}(y_{R_m} + y_{L_m}) = \frac{1}{2}\left[(1+\eta_R)y_{R_a} + (1+\eta_L)y_{L_a}\right]$$

Considering the case where the control input is to the right wing only (i.e., $u_L = 0$)

$$y_{S_m} = \frac{1}{2}\left\{(1+\eta_R)T_{RR}u_R(1+\varepsilon_R)+(1+\eta_L)T_{LR}u_R(1+\varepsilon_R)\right\}$$

$$= \frac{1}{2}\left\{(1+\eta_R)\left[\frac{1}{2}(T_S+T_A)\right] + (1+\eta_L)\left[\frac{1}{2}(T_S-T_A)\right]\right\}(1+\varepsilon_R)u_R$$

Under the assumption that products of errors may be neglected,

$$\frac{y_{S_m}}{u_{R_m}} = \frac{1}{2}\left\{\left(1+\frac{\eta_R+\eta_L+2\varepsilon_R}{2}\right)T_S + \left(\frac{\eta_R-\eta_L}{2}\right)T_A\right\} \qquad (4.1)$$

Likewise,

$$\frac{y_{A_m}}{u_{R_m}} = \frac{1}{2}\left\{\left(\frac{\eta_R-\eta_L}{2}\right)T_S + \left(1+\frac{\eta_R+\eta_L+2\varepsilon_R}{2}\right)T_A\right\} \qquad (4.2)$$

Since a gain constant times the measured transfer function does not affect the ability to identify the frequency and damping of principal modes, Eqs. (4.1) and (4.2) can be written as:

$$\frac{y_{S_m}}{u_{R_m}} = \frac{1}{2}[1+\frac{1}{2}(\eta_R+\eta_L+2\varepsilon_R)]\left\{T_S+\left(\frac{\eta_R-\eta_L}{2+\eta_R+\eta_L+2\varepsilon_R}\right)T_A\right\} \tag{4.3}$$

$$\frac{y_{A_m}}{u_{R_m}} = \frac{1}{2}[1+\frac{1}{2}(\eta_R+\eta_L+2\varepsilon_R)]\left\{\left(\frac{\eta_R-\eta_L}{2+\eta_R+\eta_L+2\varepsilon_R}\right)T_S+T_A\right\} \tag{4.4}$$

Let

$$\Delta \triangleq \frac{\eta_R-\eta_L}{2+\eta_R+\eta_L+2\varepsilon_R} \tag{4.5}$$

be called the "distortion factor" because it is this factor times the asymmetric transfer function in Eq. (4.3) which "distorts" the desired symmetric transfer function. Similarly, this same factor times T_S distorts T_A in Eq. (4.4). That is,

$$\frac{y_{S_m}}{u_{R_m}} \propto T_S + \Delta T_A \tag{4.6}$$

$$\frac{y_{A_m}}{u_{R_m}} \propto T_A + \Delta T_S \tag{4.7}$$

For values of the measurement and control scaling factors between -0.20 and +0.20, the distortion factor varies in the range

$$-0.25 \leq \Delta \leq +0.25$$

Clearly, the value of the distortion factor is most strongly dependent upon the difference of the calibration errors in the

right and left wing response measurements, n_R-n_L, and less upon the right control calibration error, ε_R. Figure 4.4 shows how Δ varies as a function of the right and left measurement calibration errors for discrete values of the control calibration error.

To study the effect of calibration errors on the damping estimates, the q_{w1} mode was chosen since both the q_{w1} symmetric and q_{w1} asymmetric modes are not obscured significantly by other modes. The symmetric or asymmetric transfer function was degraded by adding or subtracting the other transfer function with varying levels of distortion factor. The dampings calculated for these various levels of distortion factor are plotted in Figure 4.5. As can be seen, calibration errors do not have a significant effect on the calculated values of the q_{1S} and q_{1A} modal damping. The error in the calculated value is primarily due to the influence of other modes which are present even when the calibration errors are zero.

There are two important considerations to be kept in mind concerning the effect of calibration error on the calculated damping values. First, the calculated damping values presented here are empirical in the sense that the complete algorithm for accurately determining ζ is a subject for further study. Naturally, there are several data processing considerations affecting the accuracy at ζ (see Appendix B for a discussion of the method used to calculate damping). These considerations include the distance between the frequency response data points (a function of the data record length), the size of the bandwidth about the peak used in the calculations, and with actual data, the signal-to-noise ratio of each data record and the number of data records averaged. It was found that the damping value (ζ) was somewhat sensitive to the size of the bandwidth chosen about the peak. Too wide a bandwidth included too much influence from other modes and tended to underestimate ζ; too narrow a bandwith did not contain sufficient information and also underestimated ζ. Better damping values could be produced by

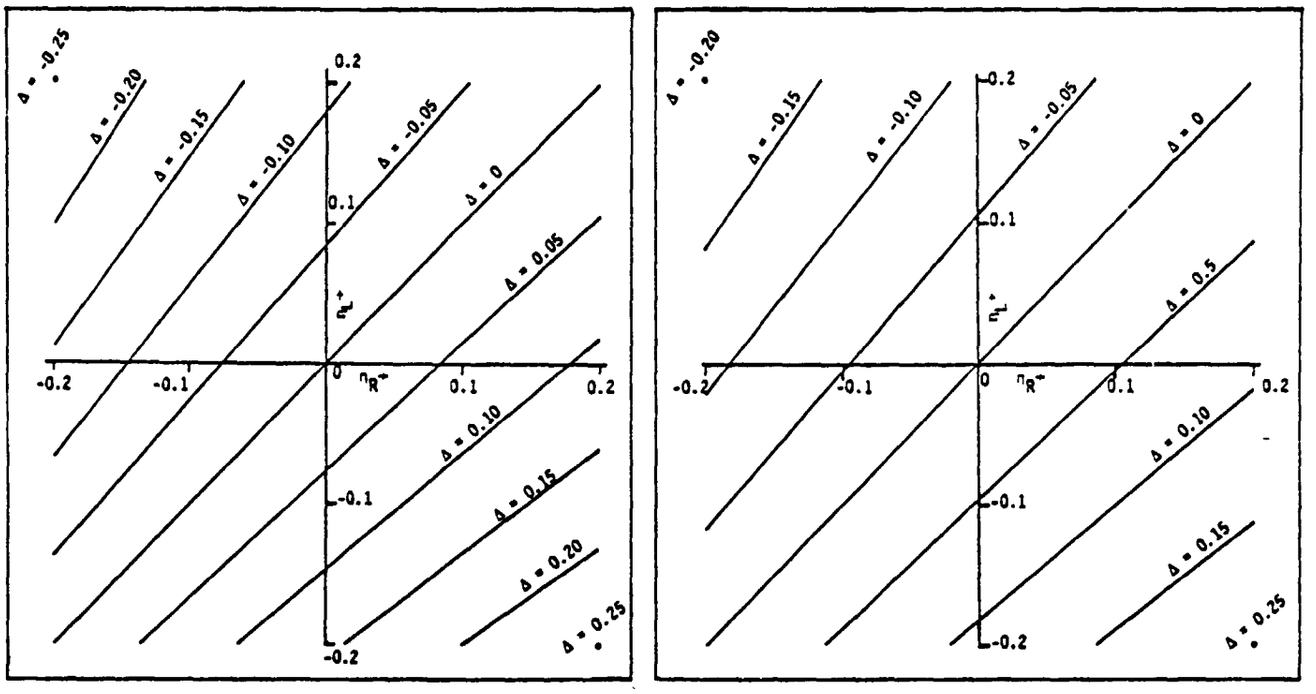

(a) $\varepsilon_R = -0.2$ (b) $\varepsilon_R = 0$

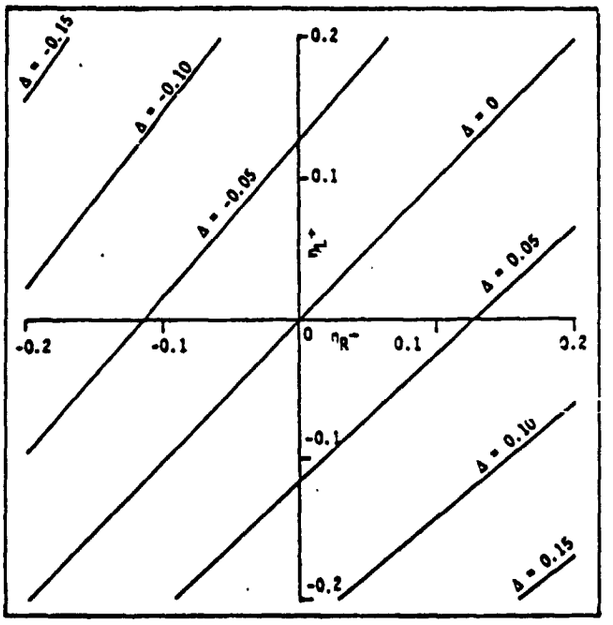

(c) $\varepsilon_R = +0.2$

Figure 4.4 Distortion Factor for Various Values of Control Calibration Error

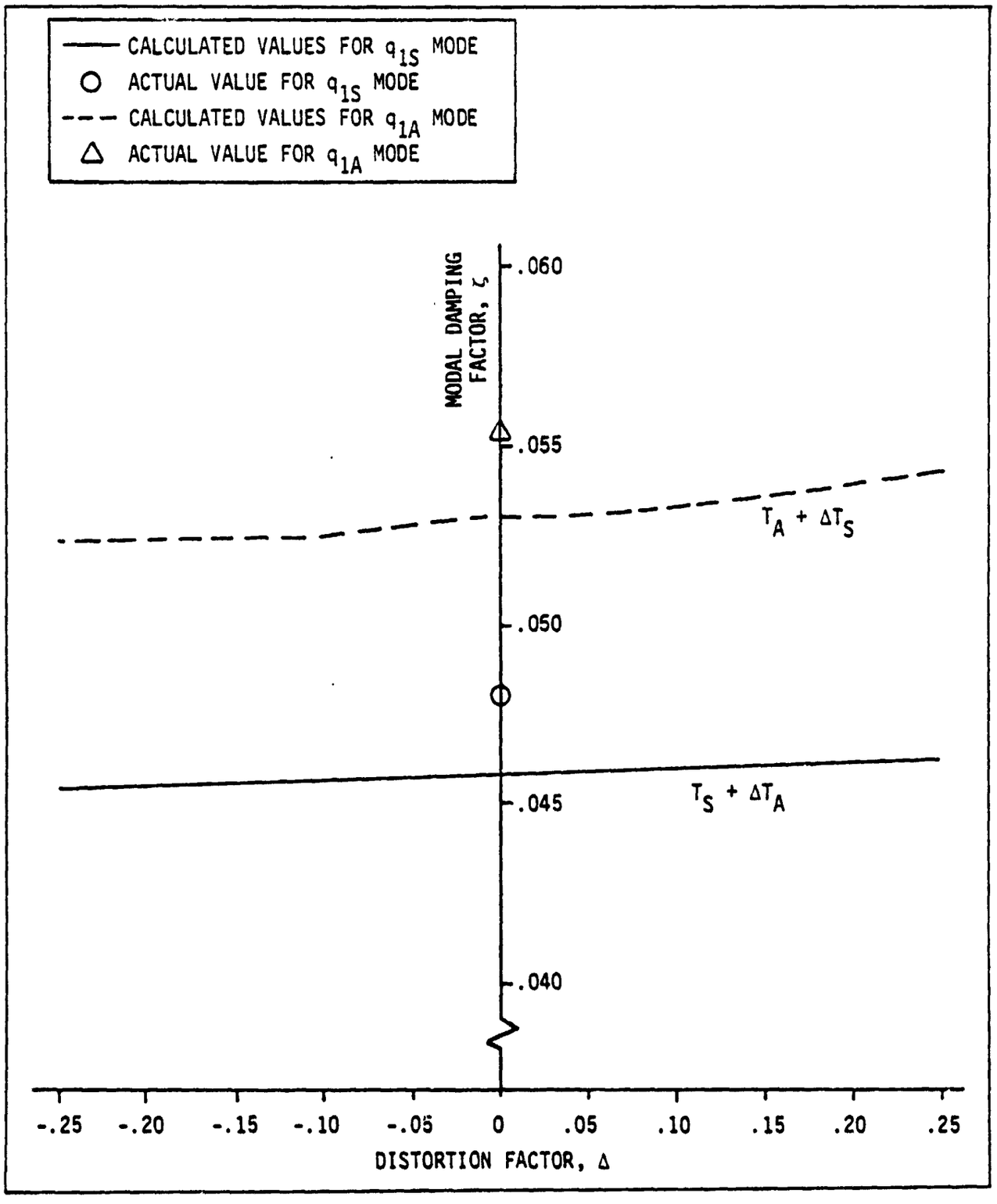

Figure 4.5 The Influence of Calibration Errors on the Calculated Values of Damping for the q_{w1} Mode from the $\ddot{q}_{w1}/\theta_o$ Transfer Function

calculating the transfer function with smaller frequency increments, and varying the bandwidth used for each peak (within what is known to be a reasonable range from the plot of the frequency response) to achieve an accurate value for ζ. The purpose of results presented here is to provide sufficient information to evaluate various test instrumentation configurations.

A second problem in analyzing the effect of calibration errors on calculated damping values is knowing what mode is actually being measured from a particular resonant peak. The q_{w2} asymmetric (q_{2A}) peak gives an excellent example of what happens to the damping calculation when a mode is being obscured by other modes. The q_{2A} mode (at 0.72 per rev) is obscured somewhat by the q_{2S} mode (at 0.66 per rev) and significantly by the rotor speed perturbation, which is an asymmetric mode (at 0.73 per rev). It is not valuable to plot the damping of the q_{2A} mode as a function of calibration errors since it is obscured by other modes. However, the calculated values for the damping for different levels of distortion are given in Table 4.2 for reference.

Table 4.2
Calculated Values of Damping for q_{2A} Mode
from $\ddot{q}_{w2}/\theta_o$ Transfer Function

DISTORTION FACTOR	CALCULATED ζ
0.0	0.0429
0.25	0.0439
1.0	0.0426
Actual Value of ζ = 0.0212	

The effect of calibration errors on the most complete test instrumentation configuration will now be discussed. Measuring both wings while exciting both wings with calibration errors on both measurement and control will be called the full test instrumentation configuration.

It follows from the expression for the theoretical transfer function in the above case in Table 2.3.1 that

$$\frac{y_{S_m}}{u_{S_m}} = k \left\{ T_S + \frac{(\varepsilon_R - \varepsilon_L)\ (\eta_R - \eta_L)}{(2+\varepsilon_R+\varepsilon_L)\ (2+\eta_R+\eta_L)}\ T_A \right\}$$

$$\frac{y_{A_m}}{u_{A_m}} = k \left\{ \frac{(\varepsilon_R - \varepsilon_L)(\eta_R - \eta_L)}{(2+\varepsilon_R+\varepsilon_L)\ (2+\eta_R+\eta_L)}\ T_S + T_A \right\}$$

where

$$k = 1 + \frac{1}{2}\ (\eta_R+\eta_L+2\varepsilon_R)$$

The distortion factor here becomes

$$\Delta = \frac{(\varepsilon_R - \varepsilon_L)(\eta_R - \eta_L)}{(2+\varepsilon_R+\varepsilon_L)(2+\eta_R+\eta_L)}$$

Considering that each calibration is 20% and that they are combined in the worst case, the magnitude of Δ is bounded at 4%. For the previous test configuration (measure both wings, excite one wing) the magnitude of Δ was bounded at 25%. Thus, by exciting both wings, even though an additional source of calibration error is introduced, the maximum distortion factor is reduced by a factor of six. Based on the variation observed in the damping as a function of the distortion factor in the previous discussion, it is concluded that the effect of calibration error on damping determin-

ations is negligible using this full test instrumentation configuration.

4.3 REQUIRED INPUT AMPLITUDES TO ACHIEVE A DESIRED SIGNAL-TO-NOISE RATIO FOR THE COUPLED WING

The input amplitude necessary to achieve a desired noise-to-signal ratio will be discussed using the vertical wing bending symmetric (q_{1S}) and asymmetric (q_{1A}) modes as examples. It is assumed that the symmetric and asymmetric motions are not decoupled; that is, the transfer functions from which these results were obtained are the sum of the symmetric and asymmetric transfer functions. This simulates the case when only one wing is excited and only one wing measured.

The noise-to-signal (NSR) ratio calculation for a particular mode is based upon the frequency response to the desired control and the frequency response to gusts in a frequency band about the resonant peak for that mode. This calculation is described in Appendix B. For example, assume information on the q_{1S} mode is sought from the frequency response of the vertical bending acceleration to flaperon input (i.e., the $\ddot{q}_{w1}/\delta_f$ transfer function). The bandwidth about the q_{1S} resonant peak for which the NSR calculations apply is 2.53 to 3.83 Hz (0.335 to 0.501 per rev).

The result is shown in Figure 4.6. From this figure, it can be seen, for example, that, if the root-mean-square gust velocity is 1 ft/sec, a noise-to-signal ratio of 0.1 would require 3.6 degrees rms flaperon input. As another example, for a gust velocity of 10 ft/sec rms, the same flaperon input results in a noise-to-signal ratio of 10. (These examples are for a first order control lag with a break frequency at 5 Hz).

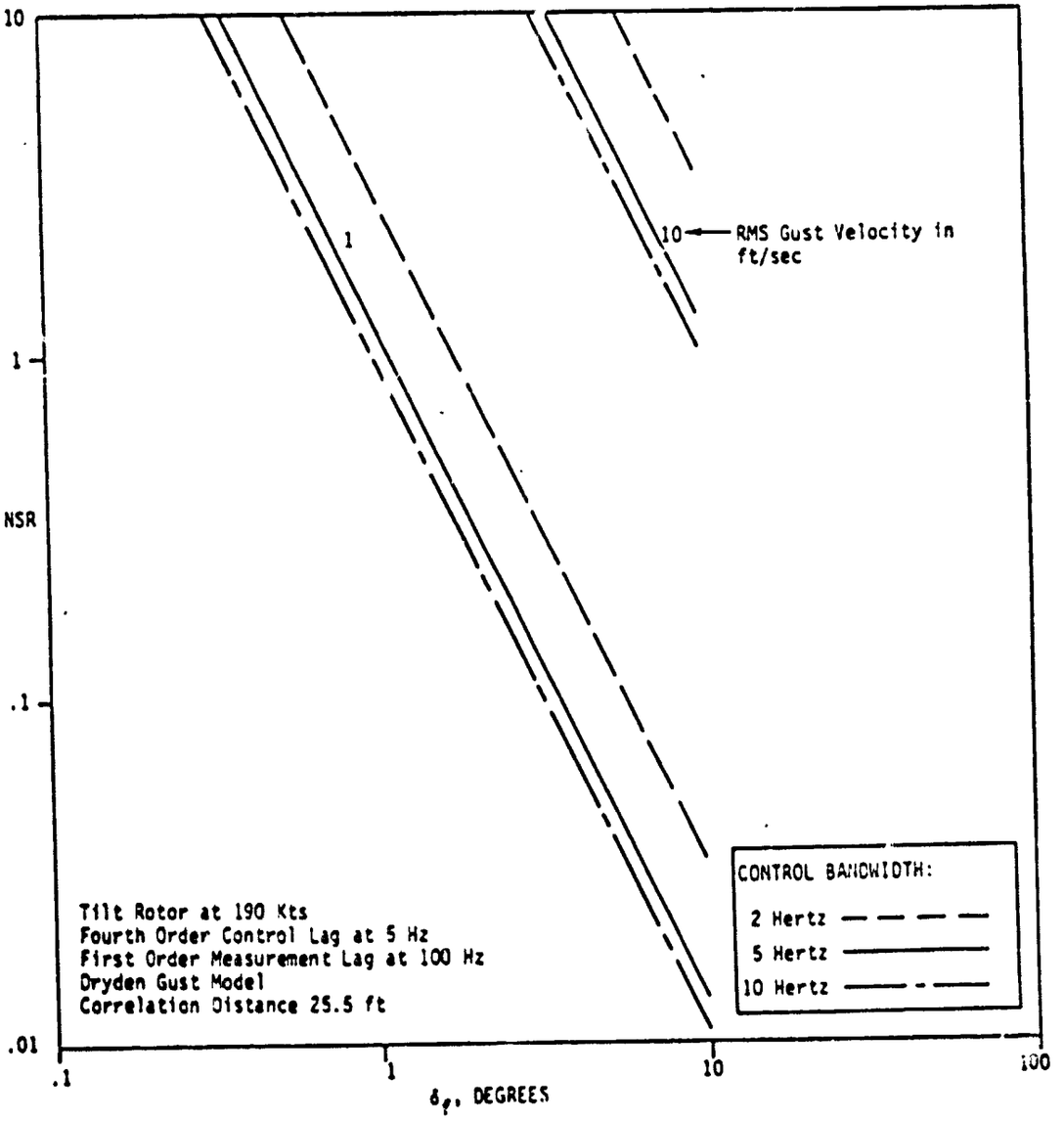

Figure 4.6 Noise-to-Signal Ratio for Symmetric Vertical Wing Bending (q_{1S}) Mode from $\ddot{q}_{w1}/\delta_f$ Transfer Function (For Frequency Range 2.53 to 3.83 Hz About the q_{1S} Peak)

Next, assume information on the q_{1A} mode is sought from the same $\ddot{q}_{w1}/\delta_f$ transfer function. Therefore, the calculations are based on a bandwidth about the q_{1A} resonant peak (3.83 to 4.82 Hz). The results are shown in Figure 4.7.

A comparison of Figures 4.6 and 4.7 shows that the same rms flaperon input in the presence of the same rms gust velocity would mean a higher (i e., worse) noise-to-signal ratio (NSR) for the q_{1A} mode than for the q_{1S} mode. This was to be expected because the q_{1A} resonant peak has a lower amplitude than the q_{1S} resonant peak. Large inputs are required to lift the signal above the noise.

A more favorable situation exists when information on the q_{1A} mode is sought from the response of $\ddot{q}_{w1}$ to collective pitch inputs because the resonant peak of the q_{w1} mode has a higher amplitude in the $\ddot{q}_{w1}/\theta_o$ transfer function. The NSR results for this case, shown in Figure 4.8, are considerably improved over the results in Figure 4.7, which were based on the $\ddot{q}_{w1}/\delta_f$ transfer function.

4.4 SUMMARY

The test configuration of exciting one wing and measuring that wing does not allow separation of the symmetric and asymmetric modal responses. It follows that determination of frequency and damping of particular modes is difficult, requiring very specialized input designs or more complicated instrumentation.

If both wings are excited and/or the responses of both wings are measured, symmetric and asymmetric motions can be separated. In this configuration, control and measurement calibration errors will result in some fractional part of unwanted modes to be present with desired modes.

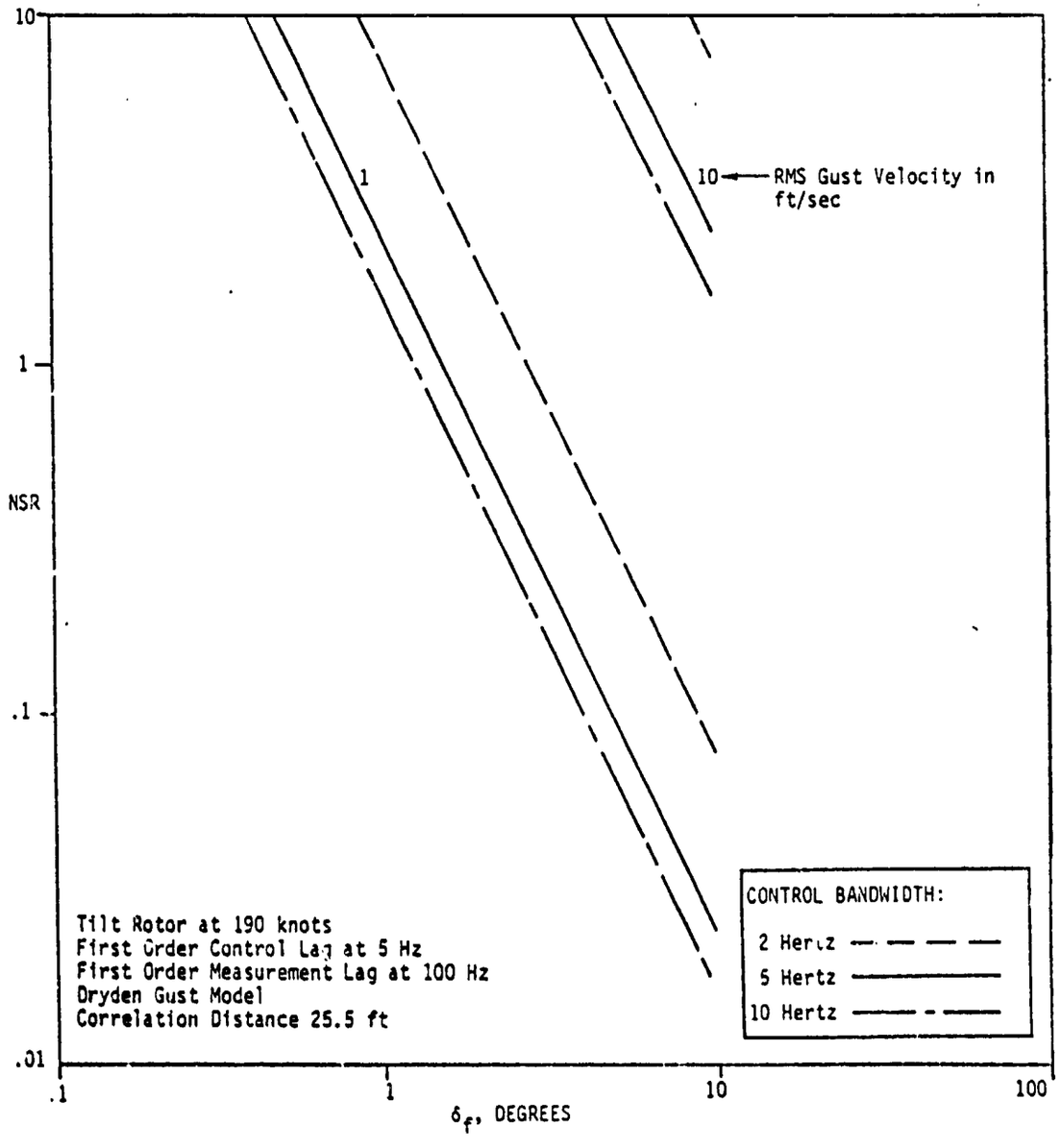

Figure 4.7 Noise-to-Signal Ratio for Asymmetric Vertical Wing Bending (q_{1A}) Mode from $\ddot{q}_{w1}/\delta_f$ Transfer Function (For Frequency Range 3.83 to 4.82 Hz About the q_{1A} Peak)

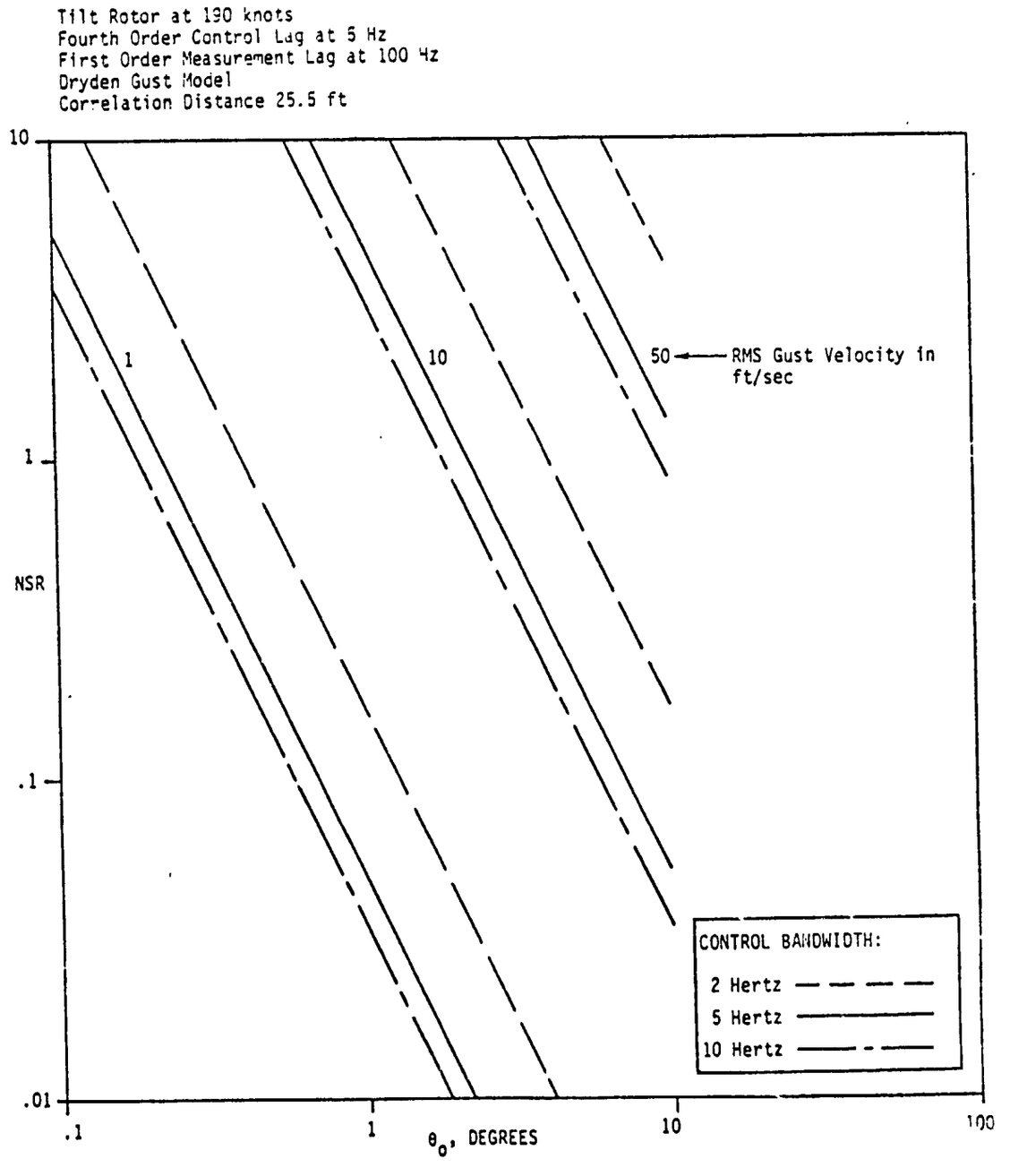

Figure 4.8 Noise-to-Signal Ratio for Asymmetric Vertical Wing Bending (q_{1A}) Mode from $\ddot{q}_{w1}/\theta_o$ Transfer Function (For Frequency Range 3.49 to 5.29 Hz About the q_{1A} Peak)

Measurement and control calibration errors less than 20% do not produce significant error in calculating damping values compared to the attenuation effects of wing cross-coupling.

V. EXAMPLES OF EVALUATION OF METHODS FOR MODAL IDENTIFICATION FROM DATA

The preceding two sections have summarized analytical results on input and measurement system requirements for XV-15 wind tunnel tests. For any specified test configuration, however, the final accuracy of the modal frequency and damping from test data depends on the processing methods used. This section discusses a preliminary evaluation of two such methods--spectral analysis and maximum likelihood parameter identification.

The objective of this phase of the study was twofold. First, it was desired to use the digital simulation as a data generator for evaluating algorithms to obtain more accurate estimates of frequency and damping. Second, use of an advanced parameter identification algorithm was to be performed on such data, and compared with the more conventional spectral analysis approaches.

5.1 SUMMARY OF ALGORITHMS

The spectral analysis of this data was performed by a Time Series Analysis Program, which computes an estimate of the transfer function, $\tilde{H}(f)$, by dividing the estimated cross-spectrum of the input and output channels by the estimated auto-spectrum of the input channel. That is,

$$\tilde{H}(f) = \frac{\tilde{S}_{uy}(f)}{\tilde{S}_{uu}(f)}$$

The spectra were computed by the Fast Fourier Transform algorithm. Details of this computer program are found in Reference 7.

The maximum likelihood parameter identification was performed with a modification of an existing program, SCIDNT [8]. The modification was to use a simplified model of a second order frequency-damping model with measurements only of acceleration. Note that, in general, it is necessary to perform a determination of transfer function order prior to actual identification. Development and programming of an analysis to do this for the current problem is beyond the scope of this program, and so the assumption of the second order model was used. For the purposes of this study, this model was considered satisfactory.

The model was as follows:

$$\begin{bmatrix}\dot{x}_1\\ \dot{x}_2\end{bmatrix} = \begin{bmatrix}0 & \omega\\ -\omega & -2\zeta\omega\end{bmatrix}\begin{bmatrix}x_1\\ x_2\end{bmatrix} + \begin{bmatrix}0\\ g\end{bmatrix} u, \quad x(0) = \begin{bmatrix}x_1(0)\\ x_2(0)\end{bmatrix}$$

$$\left(\hat{\ddot{q}}_2\right)_{meas} = \hat{y} = [-\omega \quad -2\zeta\omega]\begin{bmatrix}x_1\\ x_2\end{bmatrix} + gu$$

where the parameters to be identified are ζ, ω, g, and possibly the initial conditions, $x_1(0)$ and $x_2(0)$.

Note that this model differs from the standard state variable model for a second order system (where $F_{12} = 1$ and $F_{21} = -\omega^2$). This form is more amenable to identification than the standard canonical form.

5.2 SIMULATED TEST DATA

The data were generated by a digital computer simulation based on the XV-15 mathematical model discussed in Chapter II. It was assumed that a means existed which allowed separation of the sym-

metric and asymmetric responses of the coupled wing motion. That is, either both wings were excited or the responses of both wings were measured. Hence, the simulation used the equations of motion for the nine degree-of-freedom symmetric model. Two test cases were generated. In the first simulation case, a Gaussian random input in collective pitch was passed through a first order lag with a break frequency of 5 Hz (0.654 per rev). This lag was introduced to approximate the dynamics of the control system. The data length was 20 revolutions of the rotor, and data samples were taken every 0.04 of a revolution (0.25 rad).

In the second case, the collective pitch input was the sum of five sine waves whose frequencies were in the neighborhood of the resonant peak (specifically, they were 0.615, 0.628, 0.698, 0.739, and 0.785 per rev). The steady state response to this input was simulated for 12 revolutions of the rotor and the data sampled every 0.0239 of a revolution (0.15 rad).

5.3 RESULTS

The spectral analysis method was only used on the first set of test data (e.g., random input). When applied to the measurement of wing chordwise acceleration, an estimate of the $\ddot{q}_{w2}/\theta_o$ transfer function was obtained. It displayed a resonant peak for the q_{w2} mode at 0.663 per rev with an associated damping factor 0.091. The actual values in the simulation for the q_{w2} modal frequency and damping were 0.666 per rev and 0.043, respectively.

The maximum likelihood method was applied to the same data. This identification method resulted in an estimated q_{w2} modal frequency of 0.671 per rev and damping of 0.036. These estimates compare favorably to the true values used in the simulation.

Figure 5.1 shows the time histories for the collective pitch random input and the wing chordwise acceleration measurement from the nine degree-of-freedom simulated data. Superimposed on the $\ddot{q}_{w2}$ measurement is the estimated measurement time history from the simple second order model.

Since no data windows were used for the time series analysis method, it should be concluded that the apparent discrepancy of the result (relative to the simulated and maximum likelihood estimates) could be reduced significantly.

In order to evaluate the maximum likelihood method further, the second set of data (using sum of sines inputs) were processed. The results were an estimated q_{w2} modal frequency of 0.663 per rev and damping of 0.033. These results and those of the spectral analysis are summarized in Table 5.1.

Table 5.1
Frequency and Damping Estimates of q_{w2} Mode

	ω	ζ
Values used in simulation	0.666	0.043
Values from spectral analysis of random input case	0.663	0.091
ML values identified from random input case	0.671	0.036
ML values identified from sum of 5 sines input case	0.663	0.033

5.4 CONCLUSIONS

This brief example has demonstrated:

(1) the possibility and usefulness of generating simulated wind tunnel data as a data base for which the true values of modal frequency and damping are known,

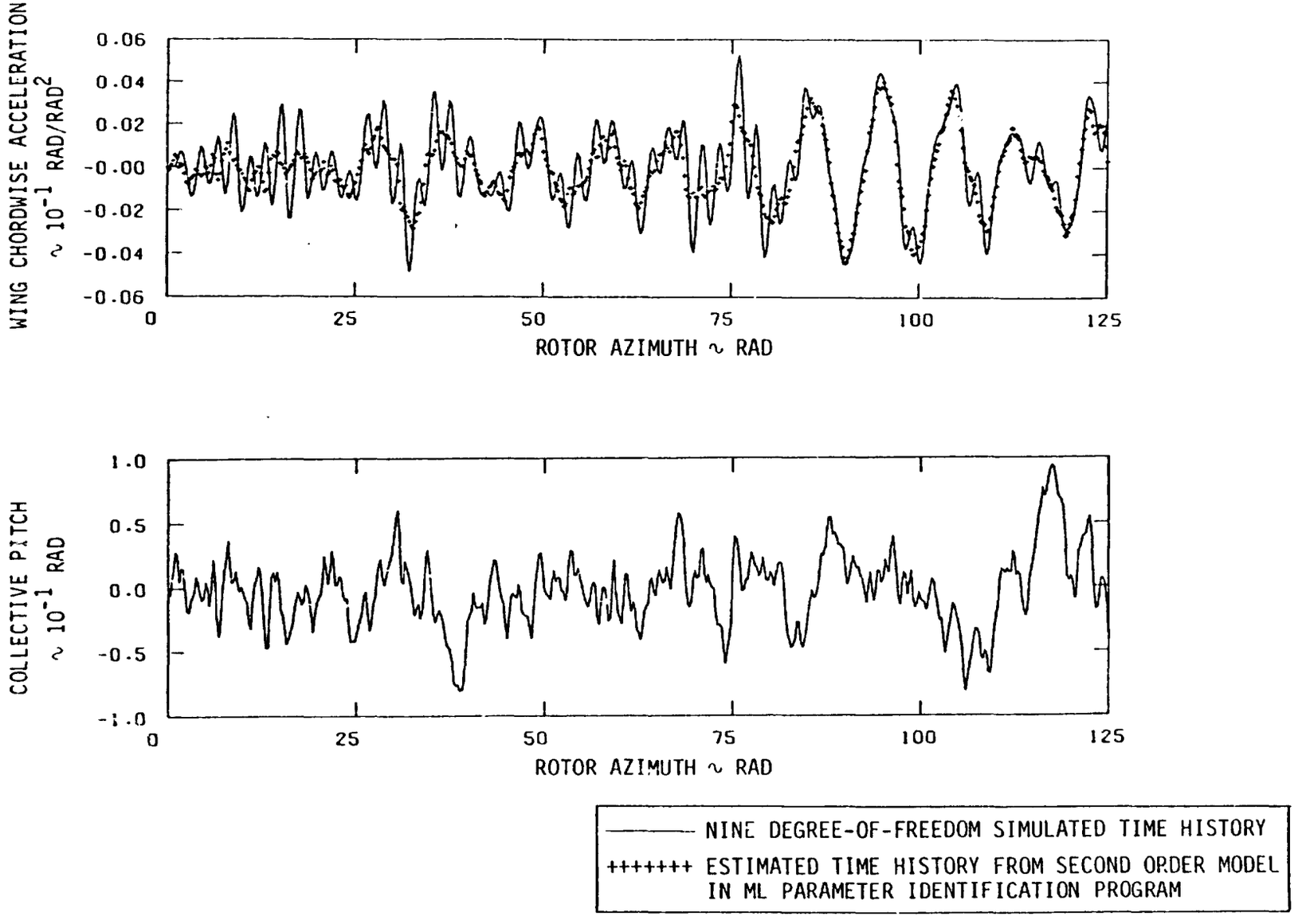

Figure 5.1 Time History Fit of Reduced Order Model to Nine Degree-of-Freedom Simulated Data

(2) a procedure for assessing the accuracy of methods (e.g., spectral analysis or parameter identification) for estimating modal frequencies and damping factors, and

(3) the ability to assess which types of control inputs will result in better estimates (random and sinusoidal inputs were used above).

Furthermore, the introduction of aerodynamic gust effects to the simulation, which was demonstrated in Chapter II, adds the possibility of studying their effects on the results of various data reduction techniques.

VI. RECOMMENDATIONS

This study has achieved the following objectives. First, several advanced analytical tools have been successfully demonstrated on the XV-15 mathematical model, including high order transfer function evaluation and maximum likelihood parameter identification techniques. Second, the application of this analysis has produced a preliminary guideline for selecting test inputs and instrumentation. Third, specific problems have been isolated which may limit the information which can be extracted from the tunnel tests.

It is recommended that several aspects of this preliminary study be expanded. These include the following:

(1) Incorporation of existing computer programs to determine the sensitivity of transfer functions (e.g., frequency response) to particular parameters such as tunnel velocity, wing stiffness, collective pitch, or measurement error. This would produce a valuable guide to estimating the most significant error sources in determination of frequency or damping.

(2) Investigation of the effects of nonlinearities in wing structural parameters, the control system, or aerodynamics. These nonlinearities would include backlash, hysteresis, or deadband.

(3) Determination of effects of fuselage modes on wing response. The present support admittedly limits the effect of fuselage coupling, but these couplings may be important in analyses of flight data.

One further recommendation is for the development of an advanced technique for processing data to determine, on-line, frequency and damping. This recommendation is based on the results of Chapters III to IV of this report, and evaluation of existing methods of spectral analysis. The basic requirement is to develop the capability to determine an estimate of the required analytical model structure and parameters which best approximate a multivariable modal response. A fundamental result of this report, for example, is that multivariable response poses a difficult problem in establishing modal contributions from a particular transfer function. This problem will be further magnified by the requirement to determine frequency and damping from multivariable response data.

The following procedure is, therefore, suggested to implement this recommendation:

(1) Develop algorithms which provide on-line estimates of model structure (e.g., transfer function) and parameters of that model.

(2) Evaluate this algorithm on the simulation discussed in Chapter II, and the transfer function evaluation of Appendix B.

(3) Implement the algorithm on-line at Ames Research Center and evaluate it on helicopter model data.

(4) Perform any modifications or further extensions of the algorithm.

It is anticipated that successful development of such a technique, combined with the results of this report, will produce a state-of-the-art technology for improving the results of advanced rotorcraft tunnel testing.

APPENDIX A

SUPPORT EQUATIONS OF MOTION

The addition of the support degrees of freedom to the equations of motion is accomplished in a manner very similar to the inclusion of the wing degrees of freedom as described in Ref. 3. The equations of motion of the support and wing will be found as functions of the forces and moments acting on the hub due to the rotor. These can then be combined with existing equations (in Ref. 3) of motion for the rotor, which require the motion of the hub, to complete the equations.

The equations for the wing and support degrees of freedom may be found by use of Lagrange's equation

$$\frac{d}{dt}\left(\frac{\partial L}{\partial \dot{\xi}_i}\right) - \frac{\partial L}{\partial \xi_i} = F_i \qquad (A.1)$$

where

L = T-V

T = Kinetic energy of the system

V = Potential energy of the system

F_i = Generalized force for ith generalized variable

ξ_i = ith generalized coordinate

Computing the kinetic energy of the system requires the inertial linear and rotational velocities of the pylon center of mass and the fuselage center of mass, which are computed below.

Figure A.1 shows the geometry and coordinates of the wing and fuselage system. The z_o axis is the rotational axis of the ψ_{sup}

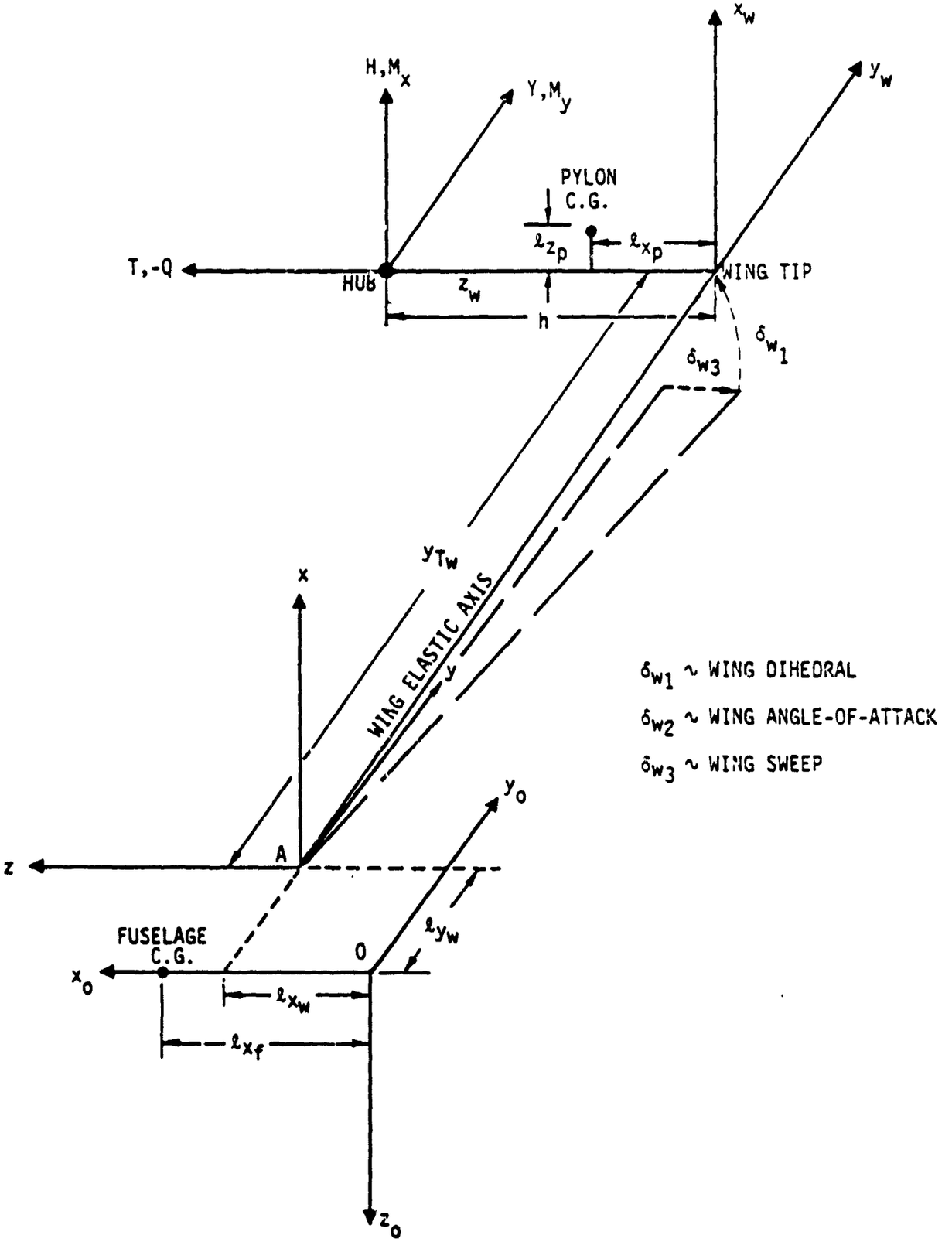

Figure A.1 Support and Cantilever Wing Geometry

degree of freedom. The fusealage center of gravity is a distance ℓ_{x_f} forward of this axis. The cantilever root restraint of the wing elastic axis is at point A, which is ℓ_{x_w} forward and ℓ_{y_w} laterally (positive right) from the z_o axis. The wing has sweep angle δ_{w_3} (positive aft), dihedral δ_{w_1} (positive up), and incidence angle δ_{w_2} (positive leading edge up). The wing semi-span is y_{T_w}. At the wing tip the δ_{w_1}, δ_{w_2}, δ_{w_3} angles are reversed so that the rotor hub axis, z_w, is parallel to x_o. The rotor forces and moments acting at the hub are T, H, Y, Q, M_x, M_y, as shown.

The system degrees-of-freedom are:

x_s = translation in x_o direction

y_s = translation in y_o direction

ψ_{sup} = rotation about z_o axis

q_{w_1} = lowest mode wing vertical bending (positive up)

q_{w_2} = lowest mode wing chordwise bending (positive up)

p = lowest mode wing torsion (positive leading edge up)

The inertial reference frame is taken to be colinear with the frame centered at point O as shown in Figure A.1 and fixed in inertial space.

Given the position of a point expressed in the A frame, denoted $\underset{A}{x}$, its position in the inertial frame is:

$$\underset{I}{x} = \begin{bmatrix} x_s \\ y_s \\ 0 \end{bmatrix} + \begin{bmatrix} c\psi_s & -s\psi_s & 0 \\ s\psi_s & c\psi_s & 0 \\ 0 & 0 & 0 \end{bmatrix} \left\{ \begin{bmatrix} \ell_{x_w} \\ \ell_{y_w} \\ 0 \end{bmatrix} \begin{bmatrix} 0 & 0 & 1 \\ 0 & 1 & 0 \\ -1 & 0 & 0 \end{bmatrix} \right\} \underset{A}{x} \qquad (A.2)$$

Similarly, given an angular position vector expressed in the A frame, denoted $\underset{A}{\alpha}$, it is expressed in the inertial frame as

$$\underset{I}{\alpha} = \begin{bmatrix} 0 \\ 0 \\ \psi_s \end{bmatrix} + \begin{bmatrix} 0 & 0 & 1 \\ 0 & 1 & 0 \\ -1 & 0 & 0 \end{bmatrix} \underset{A}{\alpha} \tag{A.3}$$

Using these two equations and equations in Refs. 1 and 2, which express the position of the hub, pylon c.g., and an arbitrary element of mass in the wing with respect to the A frame, it is straightforward to express these positions in the inertial frame.

The task of computing the kinetic energy will be much simpler if $\underset{I}{\dot{x}^T}\underset{I}{\dot{x}}$ is first calculated for an arbitrary $\underset{A}{x}$. Later, the pylon and wing positions, $\underset{A^p}{x}$ and $\underset{A^w}{x}$, will be substituted for $\underset{A}{x}$.

Let $\underset{A}{x^T} = [x, y, z]$, then from Eq. (A.1)

$$\underset{I}{x} = \begin{bmatrix} x_s + (z+\ell_{x_w})c\psi_s - (y+\ell_{y_w})s\psi_s \\ y_s + (z+\ell_{x_w})s\psi_s + (y+\ell_{y_w})c\psi_s \\ -x \end{bmatrix} \tag{A.4}$$

$$\underset{I}{\dot{x}} = \begin{bmatrix} \dot{x}_s+\dot{z}c\psi_s-\dot{y}s\psi_s-\dot{\psi}_s((z+\ell_{x_w})s\psi_s+(y+\ell_{y_w})c\psi_s) \\ \dot{y}_s+\dot{z}s\psi_s+\dot{y}c\psi_s+\dot{\psi}_s((z+\ell_{x_w})c\psi_s-(y+\ell_{y_w})s\psi_s) \\ -\dot{x} \end{bmatrix} \tag{A.5}$$

The position of the pylon center of mass in the A frame is:

C-2

$$
{}^{x}_{A^p} = \begin{bmatrix}
y_{T_w}\delta_{w_1} + q_{w_1}\,(y - h_p\eta\delta_3) + q_{w_2}\,(-y\delta_2 + h_p\eta\delta_1) \\
\quad + p_w[h_p + (h_{EA} - h_p) + z_{EA}\delta_2] \\
\hline
y_{T_w} + q_{w_1}[+h_p\eta\delta_2 - y\delta_1] + q_{w_2}[h_p\eta - y\delta_3] + p_w[-h_p\delta_1 + h_p\delta_3\delta_2] \\
\hline
-y_{T_w}\delta_3 - q_{w_1}y\delta_2 - q_{w_2}y + p_w[-((h_{EA} - h_p)\delta_2 + z_{EA})] + h_p
\end{bmatrix}
\tag{A.6}
$$

where the shorthand notation of Ref. 3 has been adopted. Similarly,

$$
{}^{\alpha}_{I^p} = \begin{bmatrix}
-\eta q_1 + \eta\delta_2 q_2 - \delta_3 p \\
-\eta\delta_3 q_1 + \eta\delta_1 q_2 + p \\
\psi_{sup} + \eta\delta_2 q_1 + \eta q_2 - \delta_1 p
\end{bmatrix}
\tag{A.7}
$$

To compute the kinetic energy of the wing, the velocity of a differential mass element will be found, and the result integrated over the wing. Let this differential element be a distance z ahead of the elastic axis and a distance r from the root measured along the elastic axis. Then the position of this element in the A frame is:

$$
{}^{x}_{A^w} = \begin{bmatrix}
r\delta_{w_1} + z\delta_{w_2} + q_{w_1}(\eta(r) - z\eta'(r)\delta_3) + q_{w_2}(-\eta(r)\delta_2 + z\eta'(r)\delta_1) \\
\quad + p_w(\xi(r) - \xi_w(y_{B_w})r\delta_3) \\
\hline
r + q_{w_1}(z\eta'(r)\delta_2 - \eta(r)\delta_1) + q_{w_2}(z\eta'(r) - \eta(r)\delta_3) - p_w\xi(r)\delta_1 + z\delta_3 \\
\hline
-r\delta_{w_3} + z - q_{w_1}\eta(r)\delta_2 - q_{w_2}\eta(r) - p_w\xi(y_{B_w})r\delta_1
\end{bmatrix}
\tag{A.8}
$$

Finally, the position of the fuselage in the inertial frame is

$$\underset{I}{x}_f = \begin{bmatrix} x_s \\ y_s \\ 0 \end{bmatrix} \tag{A.9}$$

$$\underset{I}{\alpha}_f = \begin{bmatrix} 0 \\ 0 \\ \psi_{sup} \end{bmatrix} \tag{A.10}$$

All the parts are now available to compute the kinetic energy. The positions in the A frame must be expressed in the inertial frame through Eqs. (A.2) and (A.3). Then the positions must be differentiated with respect to time, and the resulting velocities substituted into the kinetic energy of the system, which is

$$T = \frac{1}{2} m_p \dot{x}_p^T \dot{x}_p + \frac{1}{2} m_f \dot{x}_f^T \dot{x}_f + \frac{1}{2} \omega_p^T I_p \omega_p + \frac{1}{2} \omega_f^T I_f \omega_f$$

$$+ \frac{1}{2} \int_0^{y_{T_w}} \int_{T.E.}^{L.E.} \Delta m_w \dot{x}_w^T \dot{x}_w \, dz \, dr \tag{A.11}$$

The potential energy is simply

$$V = \frac{1}{2} K_{q_1} q_1^2 + K_{q_2} q_2^2 + K_p p^2 + K_{x_s} x_s^2 + K_{y_s} y_s^2 +$$

$$+ K_{\psi_{sup}} \psi_{sup}^2 \tag{A.12}$$

The generalized forces include aerodynamic forces on the wing and fuselage and structural damping terms. The aerodynamic forces for the wing were derived in Ref. 3. The aero forces on the fuselage will be neglected because they are small by comparison to the wing and rotor forces.

By substituting Eqs. (A.11) and (A.12) into Eq. (A.1) and performing the indicated differentiation and by neglecting small terms, the following vector equation results:

$$a_2\ddot{x}_w + a_1\dot{x}_w + a_o x_w = b'\delta_f + b'_G g + \tilde{a}F \qquad (A.13)$$

where

$$x_w = [q_{w_1} \quad q_{w_2} \quad p_w \quad \psi_{sup} \quad x_s \quad y_s]^T$$

δ_f = wing flaperon deflection

$$g = \begin{bmatrix} u_G \\ v_G \\ w_G \end{bmatrix} \quad \begin{matrix} \text{longitudinal gust} \\ \text{lateral gust} \\ \text{vertical gust} \end{matrix}$$

$$F = \frac{\gamma}{\sigma a}[C_T \quad 2C_H \quad 2C_y \quad C_Q \quad 2C_{M_y} \quad 2C_{M_x}]^T$$

$$b = \begin{bmatrix} b \\ \hline 0 \end{bmatrix} \quad \begin{matrix} 3 \times 4 \text{ matrix from p ... of Ref. 3.} \\ 3 \times 4 \text{ matrix} \end{matrix}$$

$$b'_G = \begin{bmatrix} b_G \\ \hline 0 \end{bmatrix} \quad \begin{matrix} 3 \times 3 \text{ matrix from p ... of Ref. 3.} \\ 3 \times 3 \text{ matrix} \end{matrix}$$

and the matrices a_2, a_1, a_o, and $\tilde{a}$ are given on the following pages.

$$a_2 = \begin{bmatrix}
m_p^* + I_{q_w}^* & 0 & S_w^* & m_p^*(1+\ell_{y_w}^*)\delta_{w_2} & -m_p^*\delta_{w_2}/y_{T_w} & -m_p^*\delta_{w_1}/y_{T_w} \\
0 & I_{q_{w_s}}^* + I_{p_x}^* n'^2_w + m_p & -S_w^*\delta_{w_2} & m_p^*(1+\ell_{y_w}^*) & -m_p^*/y_{T_w} & -m_p^*\delta_{w_3}/y_{T_w} \\
S_w^* & -S_w^*\delta_{w_2} & I_{p_w}^* + I_{p_y}^* & -I_{p_x}^*\delta_{w_1} & 0 & 0 \\
m_p^*(1-\ell_{y_w}^*)\delta_{w_2} & m_p^*(1+\ell_{y_w}^*) & -I_{p_x}^*\delta_{w_1} & I_s^* & -m_p^*(1+\ell_{y_w}^*)y_{T_w} & 0 \\
-m_p^*\delta_{w_2}/y_{T_w} & -m_p^*/y_{T_w} & 0 & -m_p^*(1+\ell_{y_w}^*)/y_{T_w} & \frac{m_p^*+m_w^*+m_f^*}{y_{T_w}^2} & 0 \\
-m_p^*\delta_{w_1}/y_{T_w} & -m_p^*\delta_{w_3}/y_{T_w} & 0 & 0 & 0 & \frac{m_p^*+m_w^*+m_f^*}{y_{T_w}}
\end{bmatrix}$$

$$a_1 = \begin{bmatrix}
C_{q_1}^* - \gamma C_{q_1}\dot{q}_1 & -\gamma C_{q_1}\dot{q}_2 & -\gamma C_{q_1}\dot{p} & 0 & 0 & 0 \\
-\gamma C_{q_2}\dot{q}_1 & C_{q_2}^* - \gamma C_{q_2}\dot{q}_2 & -\gamma C_{q_1}\dot{p} & 0 & 0 & 0 \\
-\gamma C_p\dot{q}_1 & -\gamma C_p\dot{q}_2 & C_p^* - \gamma C_{pp}\dot{} & 0 & 0 & 0 \\
0 & 0 & 0 & C_{\psi_s}^* & 0 & 0 \\
0 & 0 & 0 & 0 & C_{x_s}^* & 0 \\
0 & 0 & 0 & 0 & 0 & C_{y_s}^*
\end{bmatrix}$$

$$a_o = \begin{bmatrix} K^*_{q_1} - \gamma C_{q_1 q_1} & -\gamma C_{q_1 q_2} & -\gamma C_{q_1 p} & 0 & 0 & 0 \\ -\gamma C_{q_2 q_1} & K^*_{q_2} - \gamma C_{q_2 q_2} & -\gamma C_{q_2 p} & 0 & 0 & 0 \\ C^*_{pq} \gamma\gamma \frac{2C_T}{\sigma a} - \gamma C_{pq_1} & -\gamma C_{pq_2} & K^*_p - \gamma C_{pp} & 0 & 0 & 0 \\ 0 & 0 & 0 & K^*_{\psi_s} & 0 & 0 \\ 0 & 0 & 0 & 0 & K^*_{x_s} & 0 \\ 0 & 0 & 0 & 0 & 0 & K^*_{y_s} \end{bmatrix}$$

$$\tilde{a} = \begin{bmatrix} -2y_{T_w}\delta_2 & y_{T_w} - h\eta\delta_{w_3} & y_{T_w}\delta_{w_1} - h\eta\delta_{w_2} & 2\eta & -\eta\delta_{w_3} & \eta\delta_{w_2} \\ -2y_{T_w} & -y_{T_w}\delta_{w_2} + h\eta\delta_{w_1} & -h\eta + y_{T_w}\delta_{w_3} & -2\eta\delta_{w_2} & \eta\delta_{w_1} & \eta \\ 2z_{EA} + 2(h-h_{EA})\delta_{w_2} & h + z_{EA}\delta_{w_2} + (h_{EA}-h) & h\,\delta_{w_1} & 2\delta_{w_3} & 1 & -\delta_{w_1} \\ -2(y_{T_w}+\ell_{y_w}) & 0 & -h - \ell_{x_w} + y_{T_w}\delta_{w_3} & 0 & 0 & -1 \\ 2 & 0 & 0 & 0 & 0 & 0 \\ 0 & 0 & -1 & 0 & 0 & 0 \end{bmatrix}$$

$$I_s^* = \frac{I_s}{\frac{N}{2} I_b}$$, I_s is total yaw moment of the aircraft exclusive of the rotors.

$$m_w^* = \frac{m_w y_{T_w}^2}{\frac{N}{2} I_b}$$, m_w is mass of the wing

$$m_f^* = \frac{m_f y_{T_w}^2}{\frac{N}{2} I_b}$$, m_f is mass of the fusealage

$\ell_{y_w}^* = \ell_{y_w}/y_{T_w}$, ℓ_{y_w} is lateral component of distance from wing root elastic axis to c.g.,

$\ell_{x_w}^* = \ell_{x_w}/y_{T_w}$, ℓ_{x_w} is longitudinal component of distance from wing root elastic axis to aircraft, c.g.,

and all other parameters are as defined in Ref. 3.

The total equations of motion are found by combining the rotor equations and Eq. (A.13) as described in Ref. 3.

The numerical results of Chapter II were generated with the following simplifications:

(a) $\psi_{sup} \doteq 0$ (no torsion of supports)

(b) $\ell_{y_w} \doteq 0$ (wing cantilever attachement at c.g.)

APPENDIX B
TRANSFER FUNCTION ANALYSIS

B.1 REVIEW OF MATHEMATICAL FORMULATION

As explained in Chapter II, the mathematical model for the XV-15, as developed by Johnson [2-5], expressed in vector notation, is

$$\dot{\underline{x}} = F\underline{x} + G\underline{u} + \Gamma\underline{v}$$

$$\underline{y} = H\underline{x} + D\underline{u} \quad \text{(measurements excited by the control)}$$

$$\underline{y}' = H\underline{x} + D'\underline{v} \quad \text{(measurements excited by random gust)}$$

There is an F, G, Γ, D, and D' associated with the symmetric motion of the rotor/cantilever wing, and another F, G, Γ, D, and D' associated with asymmetric motion of the rotor/cantilever wing. The symmetric and asymmetric models are combined (as explained in Section 2.3) for a complete description of the dynamics at the left and right side of the aircraft.

The frequency responses

$$\frac{\underline{y}(s)}{\underline{u}(s)} = H(sI-F)^{-1}G + D \quad \text{(referred to as signal transfer functions)} \qquad \text{(B.1)}$$

and

$$\frac{\underline{y}'(s)}{\underline{v}(s)} = H(sI-F)^{-1}\Gamma + D' \quad \text{(referred to as noise transfer functions)} \qquad \text{(B.2)}$$

were calculated using the Leverrier method [9,10] to evaluate the adjoint. The transfer function was the primary analytical tool

used to evaluate the dynamics of the XV-15 and, hence, evaluate the instrumentation requirements and test guidelines for the wind tunnel testing of the XV-15 tilt rotor aircraft.

B.2 DERIVATION OF FORMULAE

Transfer functions for measurement of the states or linear coordinates of the states were used in several ways:

(1) The transfer function indicates if a particular measurement excited by a particular control shows a resonant peak to identify a desired mode.

(2) To study the stability of the XV-15, estimates of the damping (ζ) of the least damped modes are desired. Formulae used for calculating ζ from transfer function data are discussed in Section B.2.1.

(3) To quantify the value of different transfer functions for identifying the frequency and damping of a desired mode, and to clarify which modes contribute substantially to a resonant peak (when more than one mode are close to the peak frequency), the modal power and modal power ratio were derived. These formulae are presented in Section B.2.2.

(4) To analyze the effect of various gust levels in the wind tunnel on the ability to identify the frequency and damping of a desired mode, the noise-to-signal ratio was derived as explained in Section B.2.3. The signal power and noise power were calculated from the signal and noise transfer functions over the same frequency range.

B.2.1 Damping Calculation [6]

To evaluate the damping of a particular mode, the transfer function is approximated by a general second-order system in a region about the resonant peak for that mode. The second order system is

$$m\ddot{x} + c\dot{x} + kx = f \tag{B.3}$$

where

$\omega_n = \sqrt{k/m}$ is the natural frequency

$\zeta = c/2\omega_n m$ is the damping factor

f = control input.

This equation may be rewritten as

$$m\ddot{x} + c\dot{x} + m\omega_n^2 x = f \tag{B.4}$$

The transfer function from f to the system acceleration, $a = \ddot{x}$, is

$$\frac{a(s)}{f(s)} = T(s) = \frac{s^2}{ms^2 + cs + m\omega_n^2} \tag{B.5}$$

The Bode magnitude plot requires the magnitude of this function evaluated on the $j\omega$ axis of the s-plane.

$$T(j\omega) = \frac{-\omega^2}{m(\omega_n^2 - \omega^2) + jc\omega} \tag{B.6}$$

$$|T(j\omega)|^2 = \frac{\omega^4}{m^2(\omega_n^2-\omega^2)^2 + c^2\omega^2} \tag{B.7}$$

Eqs. (B.6) and (B.7) may be combined to yield

$$T(j\omega) = -\frac{|T(j\omega)|^2}{\omega^2}\left[m(\omega_n^2-\omega^2) - jc\omega\right] \tag{B.8}$$

This form is preferred over Eq. (B.6) because the complex denominator is eliminated.

Taking the imaginary parts of both sides of Eq. (B.8), integrating both sides, and solving for the average value of c gives

$$\bar{c} = \frac{\int_{\omega_1}^{\omega_2} \frac{Im(T)}{\omega}\, d\omega}{\int_{\omega_1}^{\omega_2} \frac{|T|^2}{\omega^2}\, d\omega} \tag{B.9}$$

where the interval (ω_1,ω_2) is chosen such that ω_n is at its midpoint and for which the approximation of the frequency response curve by the second-order system is valid (e.g., $\omega_1 = 0.8\ \omega_n$ and $\omega_2 = 1.2\ \omega_n$). The frequency at the peak, ω_p, is used as the estimate of ω_n, which is reasonable for small values of ζ since

$$\omega_p = \omega_n \sqrt{1-2\zeta^2} \tag{B.10}$$

for a second order system.

It is now necessary to compute an average value for m in order to compute the damping factor from

$$\zeta = \frac{\bar{c}}{2\omega_n \bar{m}} \tag{B.11}$$

To this end, Eq. (B.5) is written as

$$T(s) = \frac{s^2/m}{s^2 + 2\zeta\omega_n s + \omega_n^2} \tag{B.12}$$

This leads to an equation analogous to Eq. (B.7); that is,

$$|T(j\omega)|^2 = \frac{1}{m^2} \frac{\omega^4}{(\omega_n^2-\omega^2)^2 + (2\zeta\omega_n\omega)^2} \tag{B.13}$$

Substituting $2\zeta\omega_n m$ for c in Eq. (B.8) gives

$$T(j\omega) = -\frac{|T(j\omega)|^2}{\omega^2}\left[m(\omega_n^2-\omega^2) - j2\zeta\omega_n m\omega\right] \tag{B.14}$$

Substituing Eq. (B.13) into (B.14) for $|T(j\omega)|^2$ and then taking the imaginary parts of both sides of Eq. (B.14), integrating both sides, and solving for the average value of m gives

$$\bar{m} = \frac{I}{\int_{\omega_1}^{\omega_2} \frac{Im(T)}{\omega}\, d\omega} \tag{B.15}$$

where

$$I = I(\zeta) = \int_{\omega_1}^{\omega_2} \frac{2\zeta\omega_n\omega^2}{(\omega_n^2-\omega^2)^2 + (2\zeta\omega_n\omega)^2}\, d\omega \tag{B.16}$$

This integral may be computed analytically as follows:

$$I(\omega,\zeta) = \left[\tan^{-1}\left(\frac{2\zeta\omega_n\omega}{\omega_n^2-\omega^2}\right) + \frac{\zeta}{2\sqrt{1-\zeta^2}}\ln\left(\frac{\omega_n^2+\omega^2-2\omega\omega_n\sqrt{1-\zeta^2}}{\omega_n^2+\omega^2+2\omega\omega_n\sqrt{1-\zeta^2}}\right)\right]_{\omega_1}^{\omega_2}$$

Finally, substituting Eqs. (B.9) and (B.15) into Eq. (B.11) results in an implicit equation for the damping,

$$\zeta = \frac{1}{2\omega_n I(\zeta)} \cdot \frac{\left\{\int_{\omega_1}^{\omega_2} \frac{\mathrm{Im}(T)}{\omega}\, d\omega\right\}^2}{\int_{\omega_1}^{\omega_2} \frac{|T|^2}{\omega^2}\, d\omega} \qquad (B.17)$$

or

$$\zeta = \frac{P}{I(\zeta)} \qquad (B.18)$$

where P is defined appropriately from Eq. (B.17). P is a function of the transfer function between the integration limits of ω_1 and ω_2, and is <u>not</u> a function of ζ. Therefore, ζ may be found by iterative use of Eq. (B.18). It was found that, given a good initial guess for ζ, convergence was achieved in three of four iterations.

A good initial value for ζ is

$$\zeta_o = \frac{\pi}{20} - \frac{1}{10}\sqrt{\left(\frac{\pi}{2}\right)^2 - 20\cdot P} \qquad (B.19)$$

which was found from Eq. (B.18) by expanding the analytic expression for $I(\zeta)$ in a power series and neglecting second and higher order terms in ζ.

The transfer function $T(j\omega)$ was approximated by a second order system in the region of the resonance. A second order system has a phase angle of -90° at the peak. Thus, the effect of other modes on the resonance can be lessened by shifting the phase of the measured transfer function before applying Eq. (B.17). This phase shift is performed by the following equation:

$$T_{new} = T \cdot \quad -j \frac{T_p}{|T_p|} \tag{B.20}$$

where T_p is the measured response at the resonant peak.

Data Processing

The calculated value of ζ is a function of bandwidth since other modes interfere as the bandwidth increases and the accuracy of the integrals (averages) used in the calculations may deteriorate as bandwidth decreases, particularly if the number of data points in the bandwidth is small. To investigate this dependency, the following procedure was used.

Using the $\ddot{q}_{w1}/\delta_f$ transfer function as an example, $T(j\omega)$ was computed for 100 values of ω between 0.35 and 0.45 per rev for the symmetric case (q_{1s} is 0.398 per rev), and 100 values of ω between 0.49 and 0.62 for the asymmetric case (q_{1A} is 0.562 per rev). Using these data, ζ was calculated for various bandwidths containing each peak. The results are summarized in Table B.1.

The calculated values of damping presented in the body of this report were based typically on 10 to 15 data points in the frequency range of integration (i.e., in the bandwidth $\omega_2-\omega_1$). The purpose of obtaining 100 points in this small range was to reduce the numerical errors in the calculation to a negligible level. Therefore, the error in the calculated values of ζ are due to the interference of other modes and to the approximations in the theoretical method

Table B.1

Calculated Damping as a Function of Frequency Bandwidth Used for Integration

BANDWIDTH		ζ FOR q_{w1} MODE FROM $\ddot{q}_{w1}/\delta_f$ TRANSFER FUNCTION	
ω_1	ω_2	SYMMETRIC MOTION $\omega_p = 0.4002$	ASYMMETRIC MOTION $\omega_p = 0.5616$
$0.99\omega_p$	$1.01\omega_p$	0.04098	0.04200
$0.98\omega_p$	$1.02\omega_p$	0.04331	0.04619
$0.97\omega_p$	$1.03\omega_p$	0.04486	0.04977
$0.96\omega_p$	$1.04\omega_p$	0.04567	0.05194
$0.95\omega_p$	$1.05\omega_p$	0.04584*	0.05302
$0.94\omega_p$	$1.06\omega_p$	0.04578	0.05348
$0.93\omega_p$	$1.07\omega_p$	0.04503	0.05361*
$0.92\omega_p$	$1.08\omega_p$	0.04537	0.05359
$0.91\omega_p$	$1.09\omega_p$	0.04511	0.05349
$0.90\omega_p$	$1.10\omega_p$	0.04483	0.05336
True Value of ζ		0.04800	0.05540
% Error (Based on Best Value of ζ)		5.0%	3.2%

*Maximum value of ζ

of the calculation. Further study of data processing techniques should include investigation of other methods, such as that suggested by Kenney and Pancu [11].

It was found that with 10 to 15 data points in the region 0.8 ω_p to 1.2 ω_p that 0.9 ω_p to 1.1 ω_p gave the best value for damp-

ing and with 100 data points in the 0.8 ω_p to 1.2 ω_p band, that 0.95 ω_p to 1.05 ω_p gave the best value for damping. Given a small frequency increment between data points, the calculated damping does not vary significantly in the range 0.9 ω_p - 1.1 ω_p to 0.95 ω_p - 1.05 ω_p.

This analysis was performed on the q_{1s} (0.398 per rev) and q_{1A} (0.562 per rev) modes. The trends shown in Table B.1 may change somewhat for high frequency modes (such as the ζ_{+1} mode at 2.43 per rev), where the same frequency ratio about ω_p gives a bandwidth several times greater.

B.2.2 Modal Power and Modal Power Ratio

To best identify particular modes from the frequency responses of the system, it was desired to:

- Quantify the quality of different transfer functions to identify a particular mode
- Quantify the extent to which a mode is obscured when more than one are contributing to a resonant peak on the frequency response.

The quantification of a particular mode's contribution to the transfer function can be accomplished in the following manner. Consider the response of a transfer function to sinusoidal excitation and express this response in terms of the response to an impulse function. In other words, express the steady state response to a sinusoidal forcing function in terms of transient response quantities, namely the residues at the poles of the particular transfer function.

The response to these two inputs will be expanded in a partial fraction expansion. Let the subscripts t denote transient, associated withan impulse input; s denote sinusoidal, associated with a sinusoidal input; and ss denote steady state, associated with a sinusoidal input after the transients have died out.

For an nth order system,

$$y_t(s) = T(s)\mathcal{L}\{\delta(t)\} = T(s) \equiv \frac{N(s)}{D(s)} \tag{B.21}$$

$$y_t(s) = \sum_{i=1}^{n} \frac{k_i}{(s-\lambda_i)} \tag{B.22}$$

where N(s) and D(s) are the numerator and denominator polynomials, respectively, and the λ_i's are the poles of T(s) and the k_i's are the residues at those poles.

Forcing the system with a complex sinusoid of unit magnitude gives

$$y_s(s) = T(s)\,\mathcal{L}\left\{e^{j\omega_o t}\right\} =$$

$$= \frac{T(s)}{(s-j\omega_o)} = \frac{N(s)}{(s-j\omega_o)D(s)} \tag{B.23}$$

$$= \left[\sum_{i=1}^{n} \frac{k_i'}{(s-\lambda_i)}\right] + \frac{k_{ss}}{(s-j\omega_o)} \tag{B.24}$$

From Eqs. (B.21) and (B.23), it is seen that

$$y_t(s) - (s-j\omega_o)y_s(s) = 0 \tag{B.25}$$

The next step is to substitute Eq. (B.22) for y_t and Eq. (B.24) for y_s in Eq. (B.25) and to express the result as the ratio of two polynomials, whose numerator polynomial must be =0 identically for all values of s. Hence, the coefficient of each power of s must = 0. The following relationships result.

$$k_{ss} = \sum_{i=1}^{n} k_i' \tag{B.26}$$

$$k_i' = \frac{k_i}{\lambda_i - j\omega_o} \tag{B.27}$$

Therefore,

$$k_{ss} = - \sum_{i=1}^{n} \frac{k_i}{\lambda_i - j\omega_o} \tag{B.28}$$

The steady state response is then

$$y_{ss}(s) = k_{ss} e^{j\omega_o t} = e^{j\omega_o t} \sum_{i=1}^{n} \frac{-k_i}{\lambda_i - j\omega_o} \tag{B.29}$$

A complex sinusoid was used because it simplifies the algebra. The steady state response to a purely sinusoidal excitation, $u = \sin \omega_o t$, can be obtained by merely taking $\mathrm{Im}[y_{ss}(s)]$.

The magnitude of the steady state response is

$$|T(j\omega_o)| = k_{ss} \tag{B.30}$$

where T(s) is the system transfer function. The power in an interval (ω_2, ω_1) about a resonant peak is defined as

$$P \triangleq \int_{\omega_1}^{\omega_2} |T(j\omega)|^2 \, d\omega$$

$$= \int_{\omega_1}^{\omega_2} \vec{T}(j\omega) \cdot \vec{T}(j\omega) \, d\omega \qquad \text{(B.31)}$$

where $\vec{T}(j\omega)$ is a vector in the complex plane and $(\cdot)$ indicates the vector inner (dot) product.

From Eqs. (B.29) and (B.30),

$$\vec{T}(j\omega) = \sum_{i=1}^{n} \vec{T}_i(j\omega) \qquad \text{(B.32)}$$

where

$$\vec{T}_i(j\omega) = \frac{k_i}{\lambda_i - j\omega} \qquad \text{(B.33)}$$

This is equivalent to saying that the total system response at frequency ω is the sum of the responses of the individual modes (i.e., λ_i's).

For each oscillatory mode, there exists a conjugate complex pair of poles, which will be denoted λ_i and $\lambda_\ell = \bar{\lambda}_i$, whose associated residues are k_i and $k_\ell = \bar{k}_i$. Let

$$\vec{T}_i^* = \vec{T}_i + \vec{T}_\ell$$

$$= - \frac{k_i}{\lambda_i - j\omega} - \frac{\bar{k}_i}{\bar{\lambda}_i - j\omega} \qquad \text{(B.34)}$$

Then the contribution of this oscillatory mode to the total power is

$$P_i \triangleq \int_{\omega_1}^{\omega_2} \vec{T}_i^*(j\omega) \cdot \vec{T}(j\omega)\, d\omega \qquad (B.35)$$

and ratio of this fractional power to the total power (Eq. (B.31)) is called the modal power ratio for the ith oscillatory mode:

$$MPR = \frac{P_i}{P} \qquad (B.36)$$

B.2.3 Noise-to-Signal Ratio

The transfer functions given in Section B.1

$$\frac{y(s)}{u(s)} \rightarrow H_s(j\omega) \quad \text{(signal transfer function)}$$

$$\frac{y'(s)}{v(s)} \rightarrow H_n(j\omega) \quad \text{(noise transfer function)}$$

give the gain and phase of the system when excited at a discrete frequency, and since the model is linear, any number of frequency responses can be added to give the response to the sum of the inputs. Theoretically, white noise would give the entire transfer function since it includes all frequencies.

Thus, to establish the ratio of how a particular measurement responds to random gusts in the tunnel compared to how it responds to commanded controls. The signal squared, or power of the two transfer functions, can be compared in the frequency range of interest.

$$S/N = \frac{\int_{\omega_1}^{\omega_2} |u|^2 \, |H_s|^2 \, d\omega}{\int_{\omega_1}^{\omega_2} q \, \phi_n \, d\omega + r(\omega_2 - \omega_1)}$$

where q is the gust covariance and r is the measurement covariance (considered as white noise in the frequency range of interest)

$$q = 2 \, T_{corr} \, \chi(t)$$

where

T_{corr} is the correlation time of the noise = L/u_o (correlation distance divided by the wind velocity)

$\chi(t)$ is the autocorrelation of the noise

$\chi(0) = v_{rms}^2$

ϕ_n is a composite power spectrum obtained in the following way:

$$\phi_{1_{out}} = \phi_{1_{in}} \, |H_1|^2$$

$$\phi_{2_{out}} = \phi_{2_{in}} \, |H_2|^2$$

$$\phi_{3_{out}} = \phi_{3_{in}} \, |H_3|^2$$

where ϕ_1, ϕ_2, ϕ_3 correspond to the longitudinal, lateral, and vertical spectrum, respectively, of the Dryden model, and H_1, H_2,

H_3 are the gust transfer functions from these three sources to the desired measurement. Assuming the gust from the three directions is uncorrelated means that the power from these three signals can be added in an RMS sense; therefore, these sums can be integrated

$$\phi_n = \sum_{i=1}^{3} \phi_{i_{out}}$$

$$S/N = \frac{u_{rms}^2 \int_{\omega_1}^{\omega_2} |H|^2 \, d\omega}{\int_{\omega_1}^{\omega_2} \phi_n \, d\omega + r(\omega_2 - \omega_1)} \tag{B.37}$$

The reciprocal of this relationship, the noise-to-signal ratio (NSR), is more convenient to work with since the gust effects can be studied alone without the measurement noise.

$$N/S = \frac{q \, X_n}{u_{rms}^2 X_s} + \frac{r(\omega_2 - \omega_1)}{u_{rms}^2 X_s} \tag{B.38}$$

where X_n and X_s are the power under the noise and signal power spectra. The noise-to-signal ratio for the measurement can be added in if it's characteristics are known. It should be pointed out that this is the noise-to-signal ratio for one data record. Normally, k records are recorded and averaged in the frequency domain, where the signal adds and the random noise tends to cancel, greatly improving the signal-to-noise ratio. Bendat and Piersol [12] suggest using 10 records or more. The principal restriction is the total sample time.

The point to be emphasized is that the signal-to-noise ratio in Eq. (10) is for one record, and thus all the noise-to-signal (NSR) plots in Chapters III and IV are for one data record.

APPENDIX C
TRANSFER FUNCTION FREQUENCY RESPONSES

This appendix presents the Bode plots for the rotor/cantilever wing and coupled wing models. These plots are outputed from the transfer function analysis program. Other data outputed are the poles, zeroes, and residues of these transfer functions. These latter outputs are not presented here.

Each Bode plot is given with a reference scale which indicates, according to the poles of the transfer function, which degree of freedom is predominant at a particular frequency.

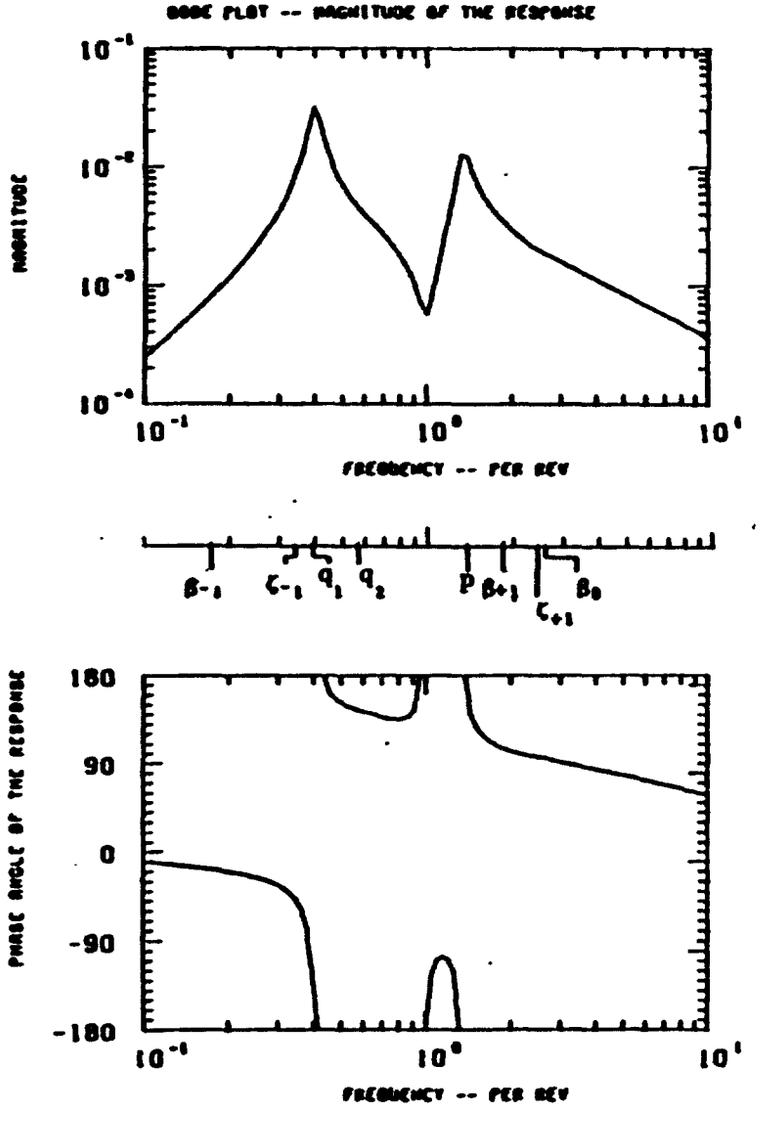

Figure C.1 $\ddot{q}_{w1}/\delta_f$ - Wing Vertical Acceleration to Flaperon (Symmetric)

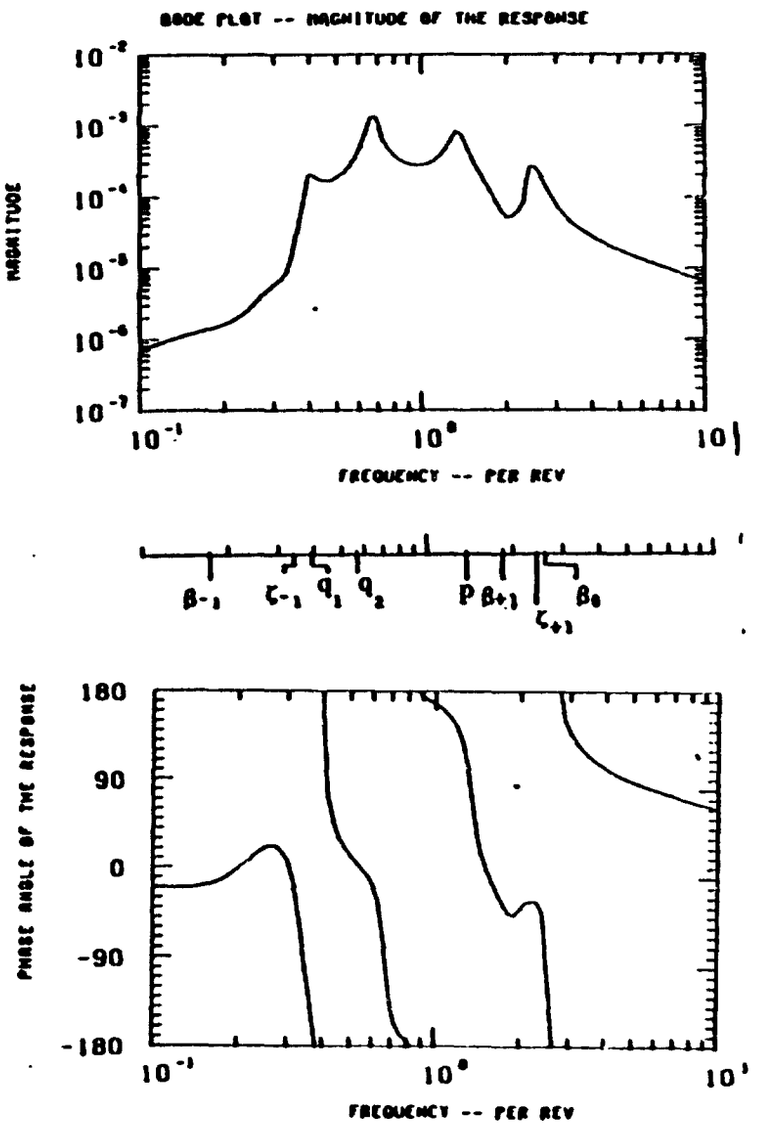

Figure C.2 $\ddot{q}_{w2}/\delta_f$ - Wing Chordwise Acceleration to Flaperon (Symmetric)

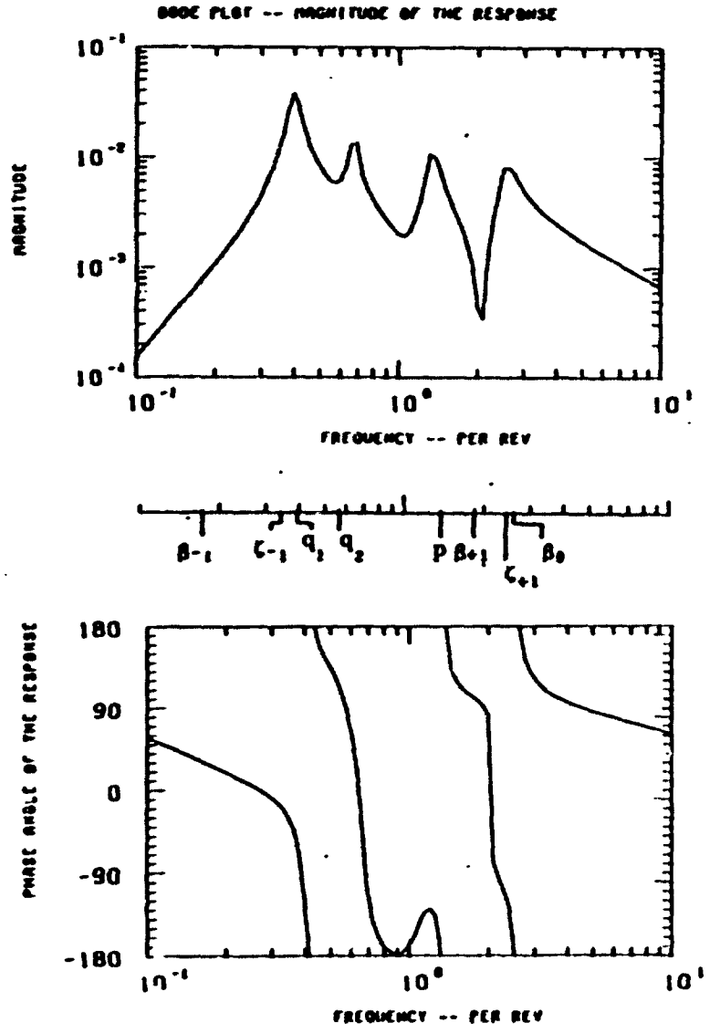

Figure C.3 $\ddot{q}_{w1}/\theta_o$ - Wing Vertical Acceleration to Collective (Symmetric)

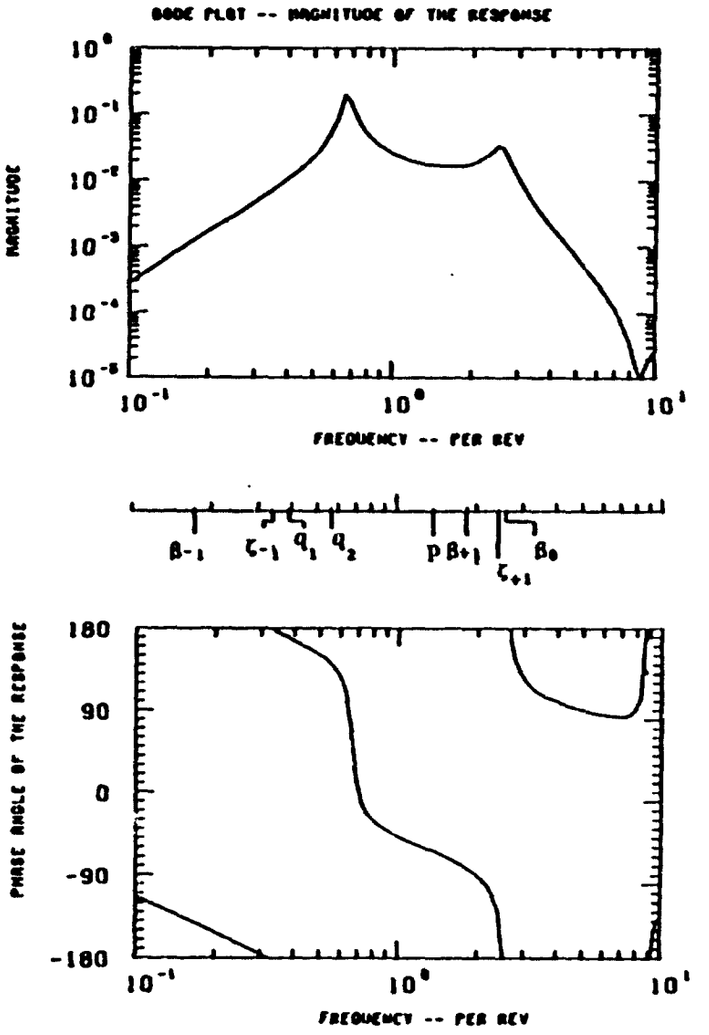

Figure C.4 $\ddot{q}_{w2}/\theta_o$ - Wing Chordwise Acceleration to Collective (Symmetric)

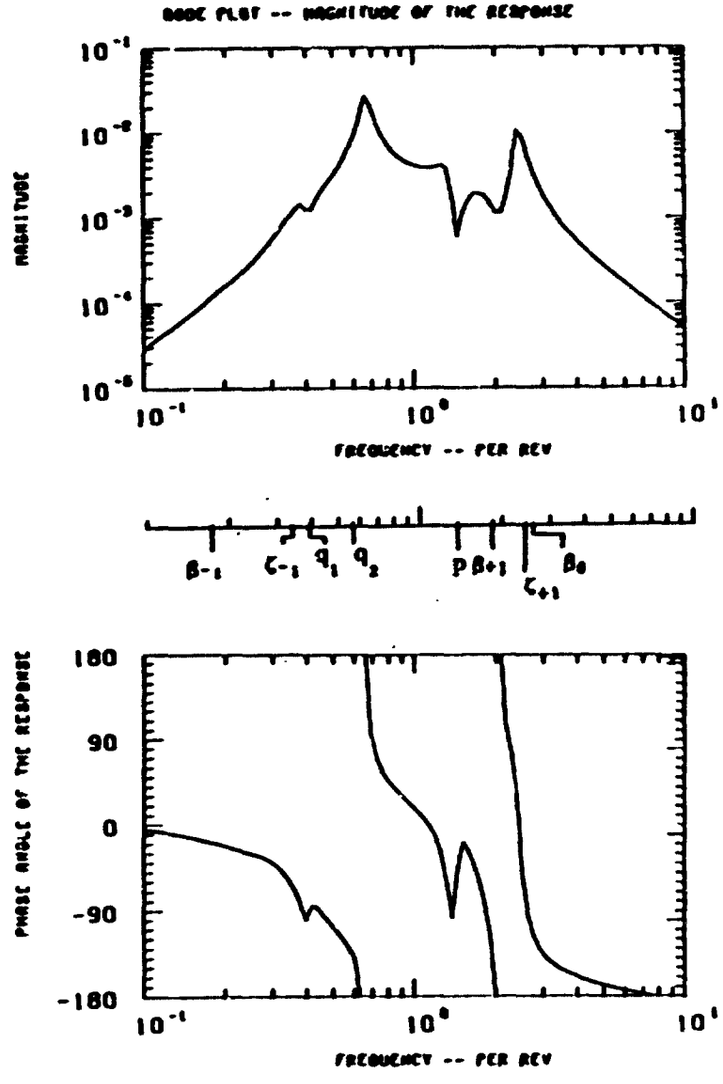

Figure C.5 $\ddot{q}_{w2}/\theta_{1s}$ - Wing Chordwise to Longitudinal Cyclic (Symmetric)

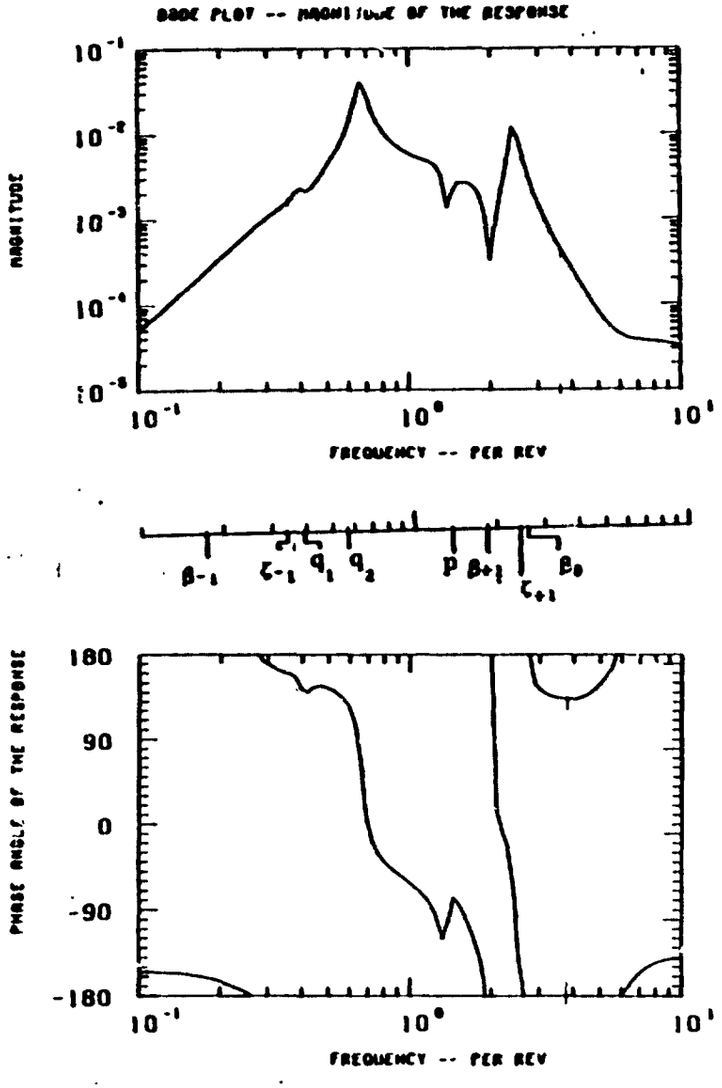

Figure C.6 $\ddot{q}_{w2}/\theta_{1c}$ - Wing Chordwise to Lateral Cyclic (Symmetric)

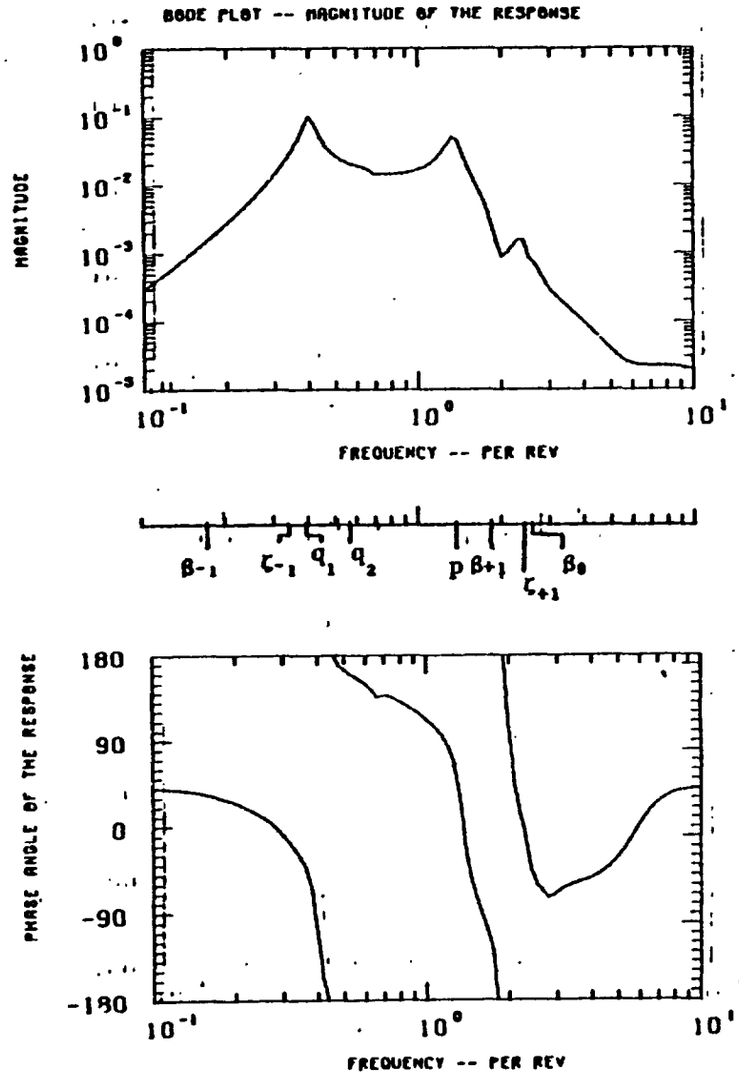

Figure C $\ddot{q}_{w1}/\theta_{1s}$ - Wing Vertical Acceleration to Longitudinal Cyclic (Symmetric)

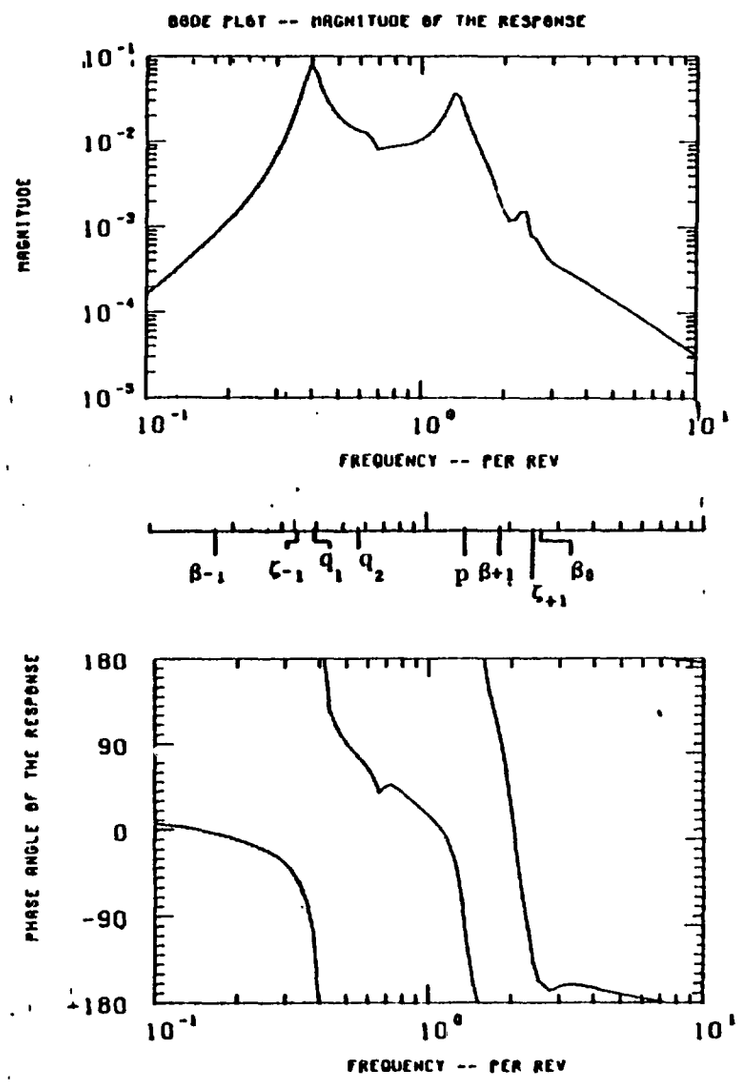

Figure C.8 $\ddot{q}_{w1}/\theta_{1c}$ - Wing Vertical Acceleration to Lateral Cyclic (Symmetric)

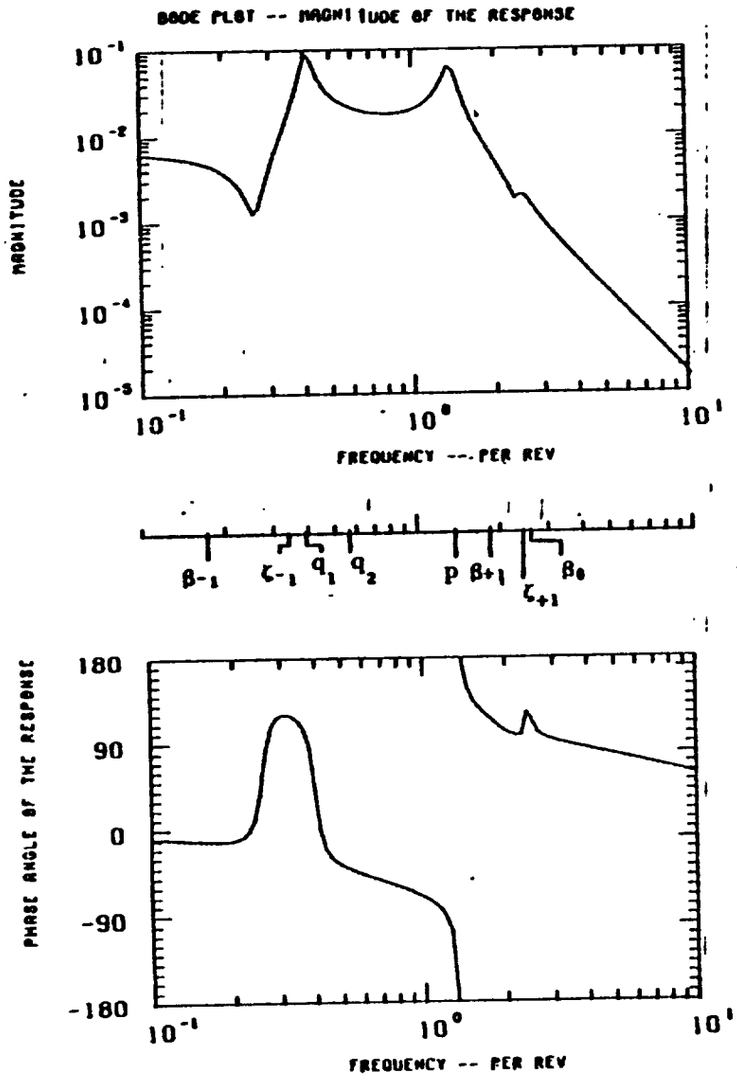

Figure C.9 p/δ_f - Wing Torsion to Flaperon (Symmetric)

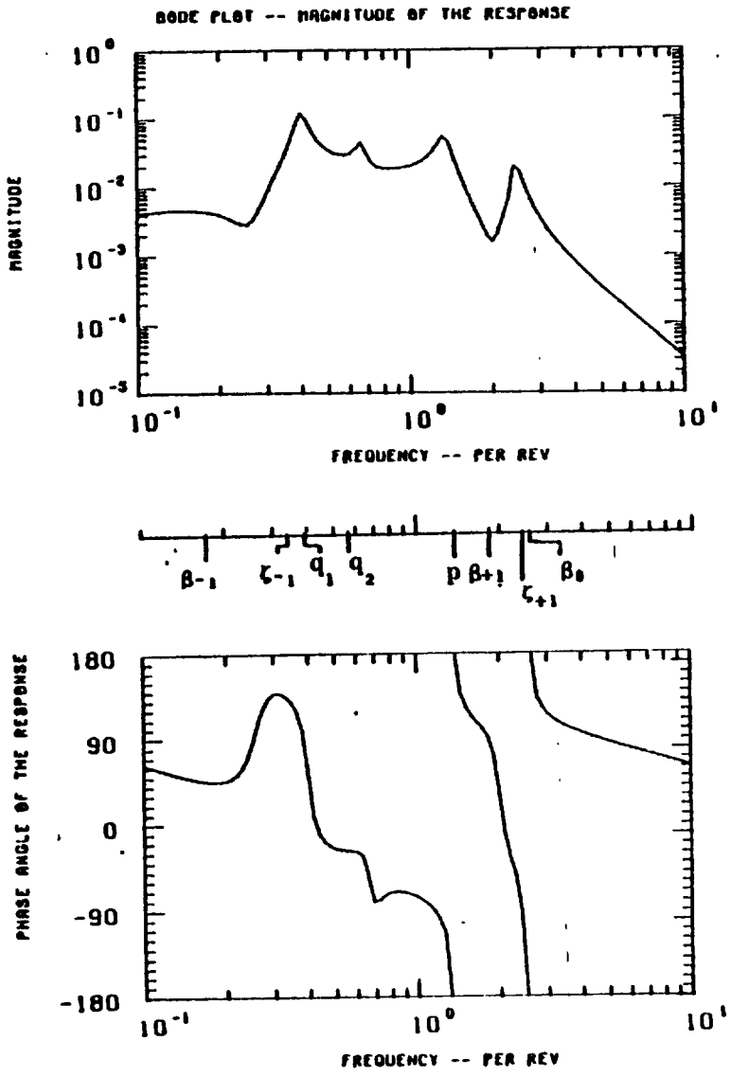

Figure C.10 p/θ_o - Wing Torsion to Collective (Symmetric)

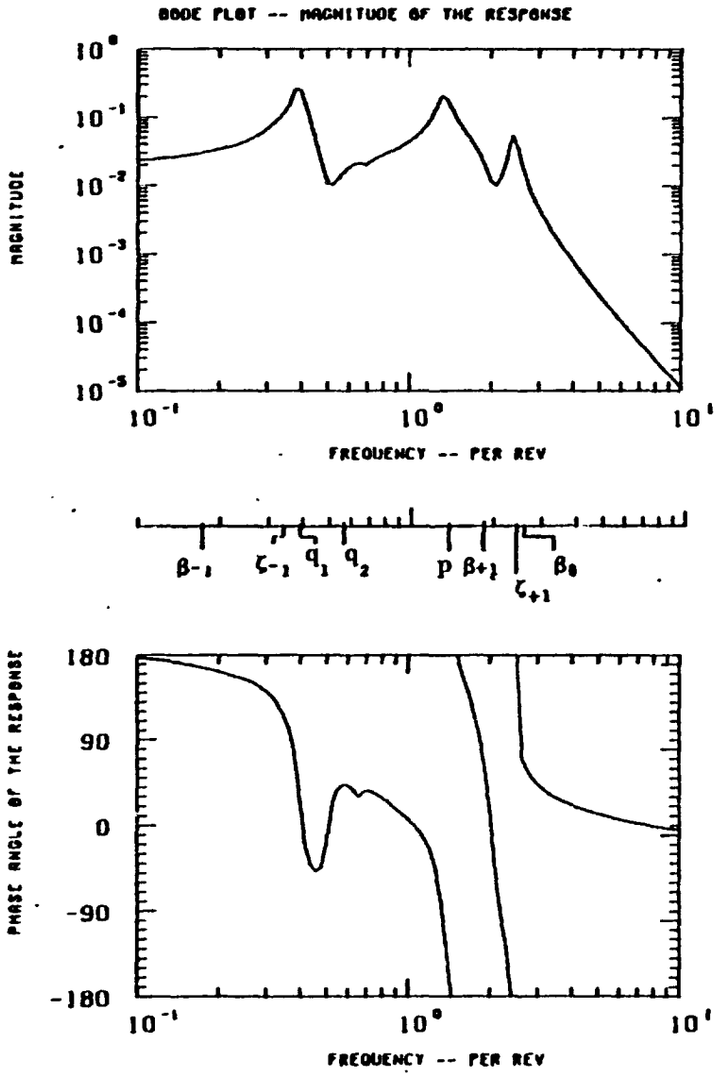

Figure C.11 p/θ_{1c} - Wing Torsion to Lateral Cyclic (Symmetric)

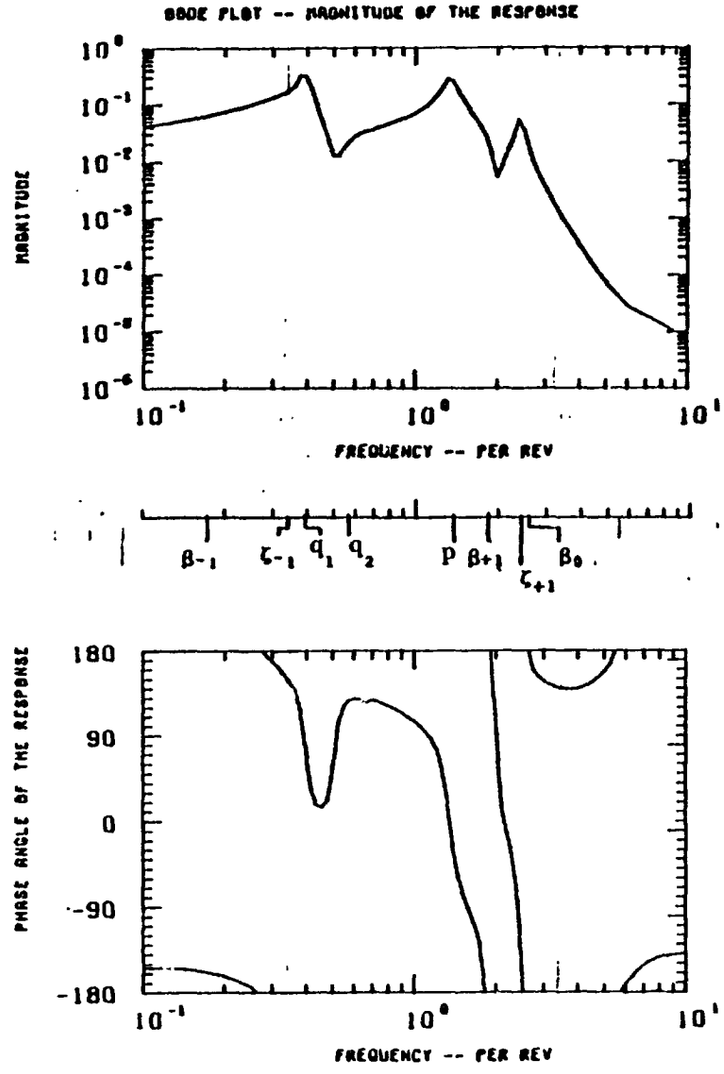

Figure C.12 p/θ_{1s} - Wing Torsion to Longitudinal Cyclic (Symmetric)

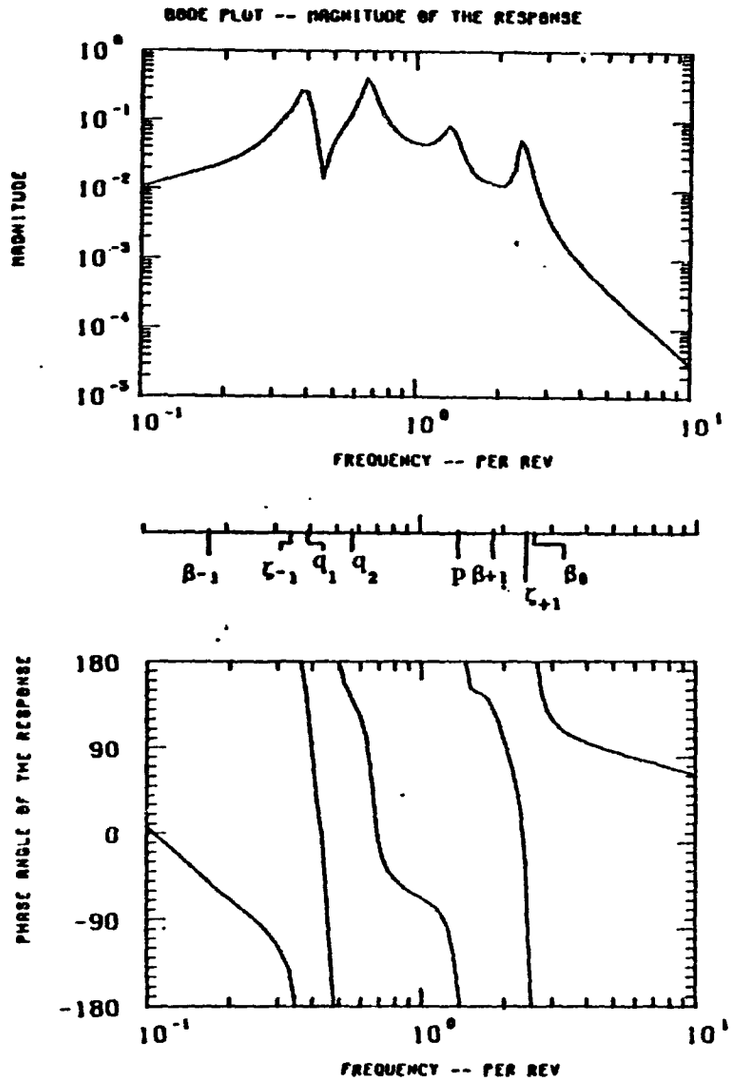

Figure C.13 β_{GC}/θ_o - Fore/Aft Gimbal Flapping to Collective (Symmetric)

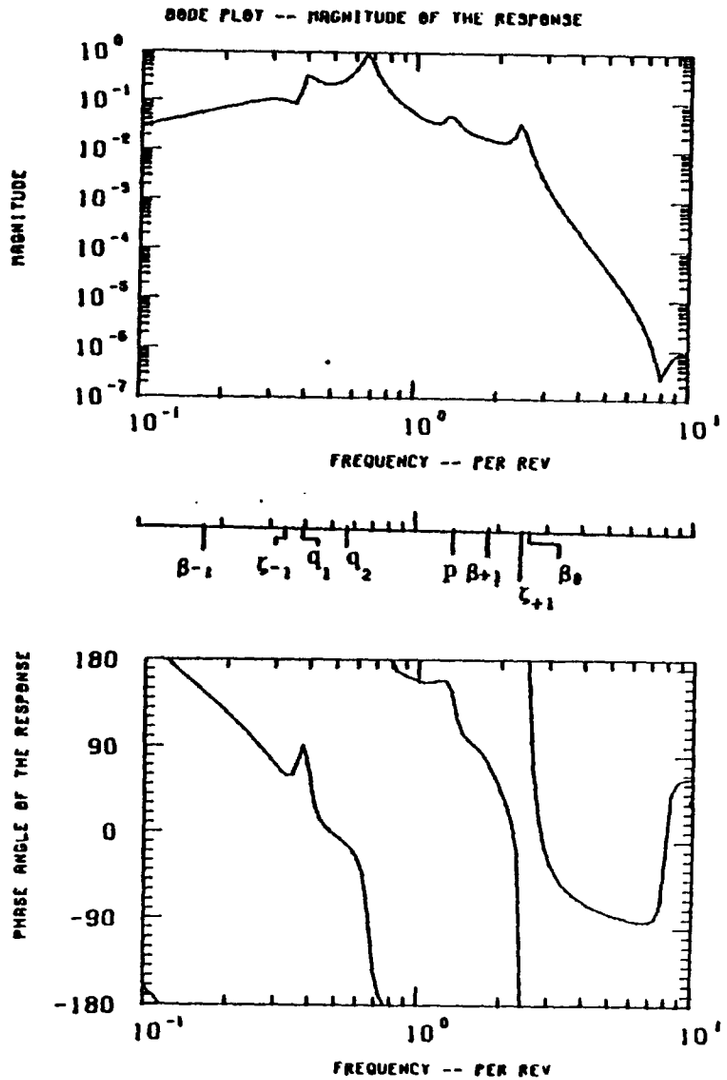

Figure C.14 β_{GS}/θ_o - Lateral Gimbal Flapping to Collective (Symmetric)

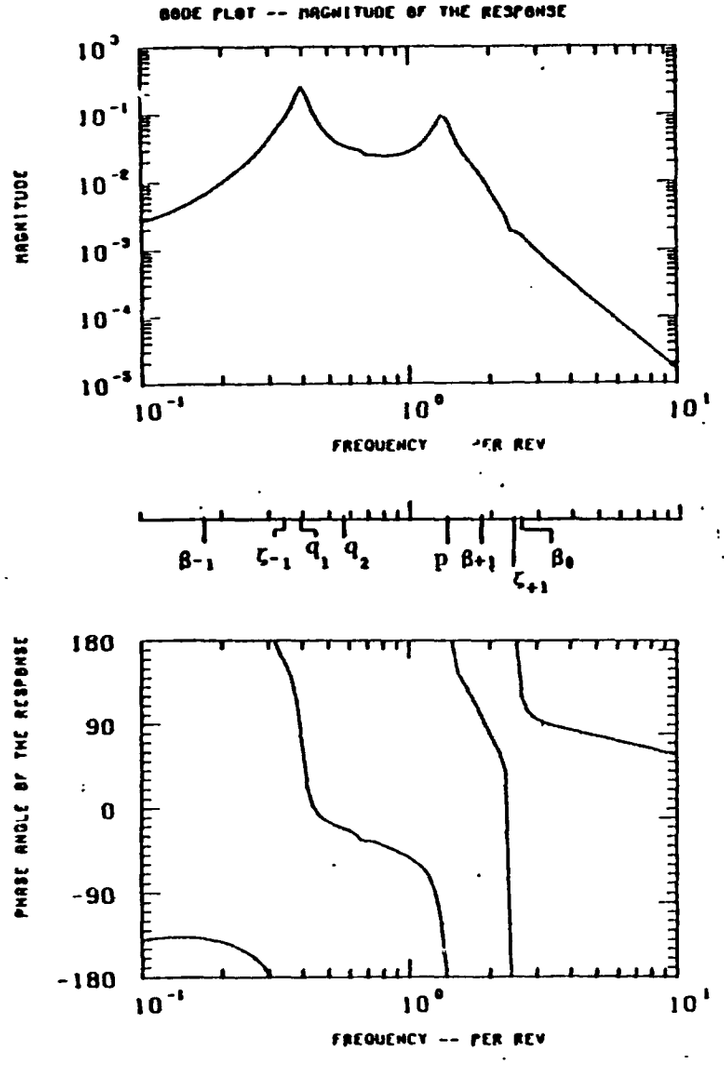

Figure C.15 β_{GC}/δ_f - Fore/Aft Gimbal Flapping to Flaperon (Symmetric)

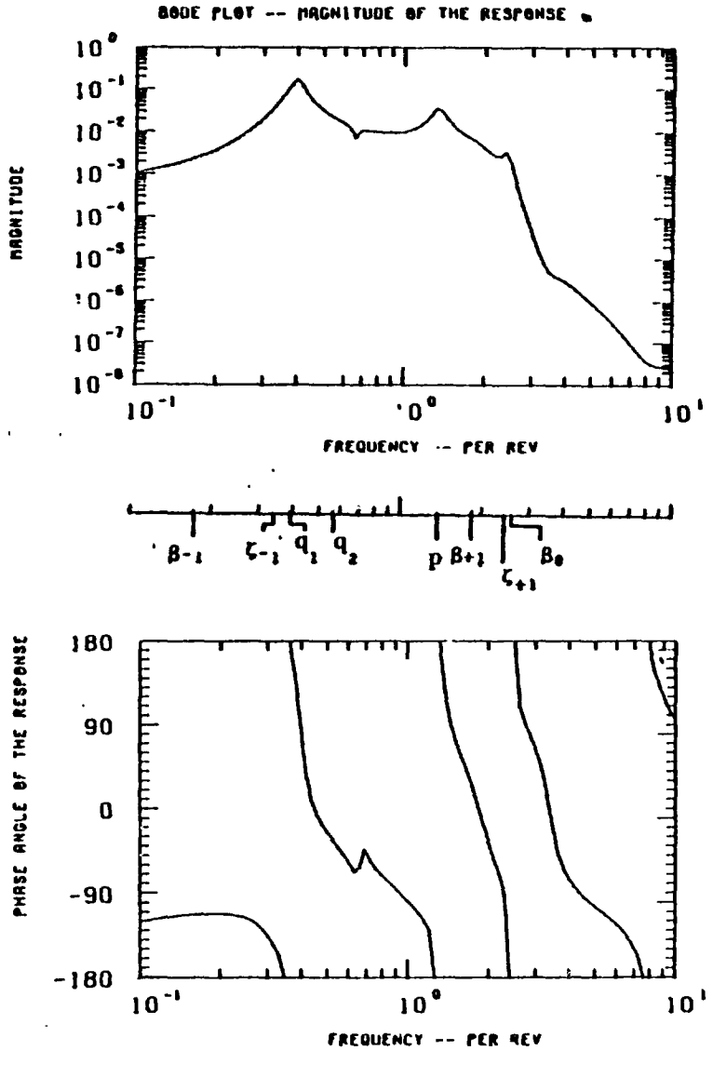

Figure C.16 β_{GS}/δ_f - Lateral Flapping to Flaperon (Symmetric)

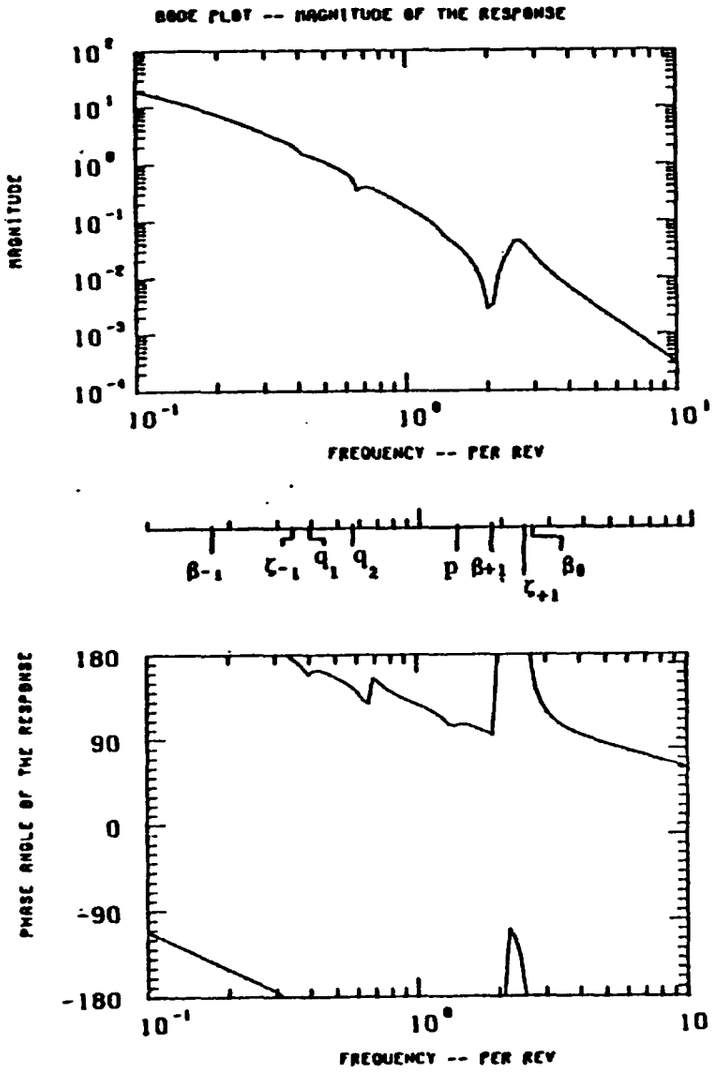

Figure C.17 ψ_s/θ_o - Rotor Perturbation to Collective (Symmetric)

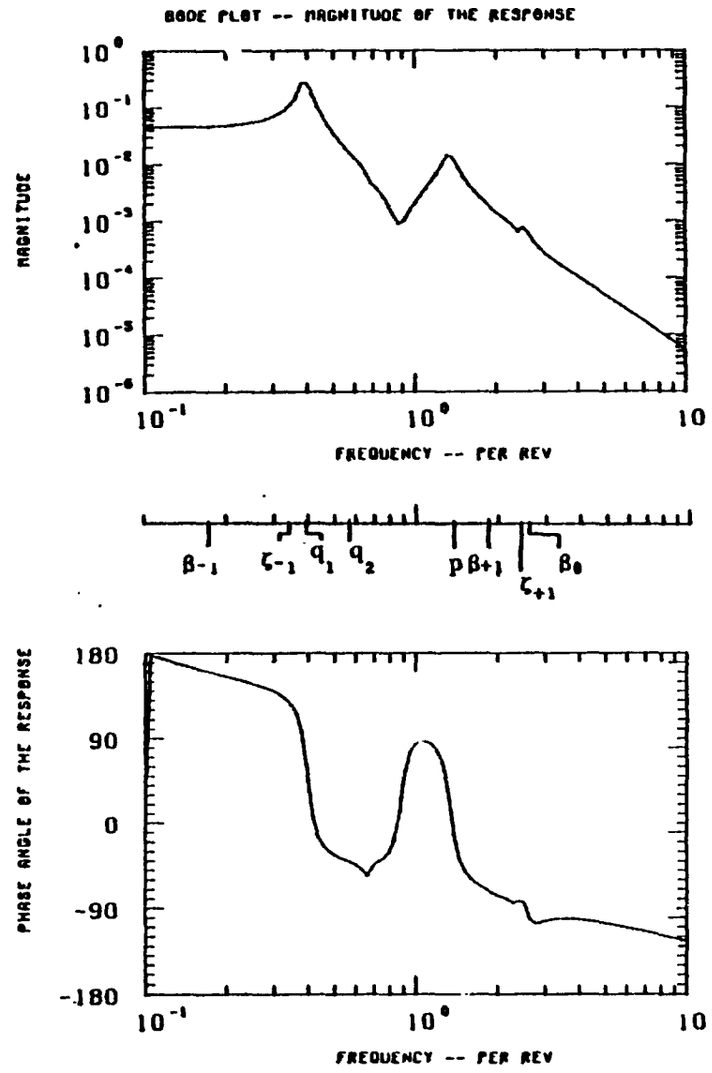

Figure C.18 ψ_s/δ_f - Rotor Perturbation to Flaperon (Symmetric)

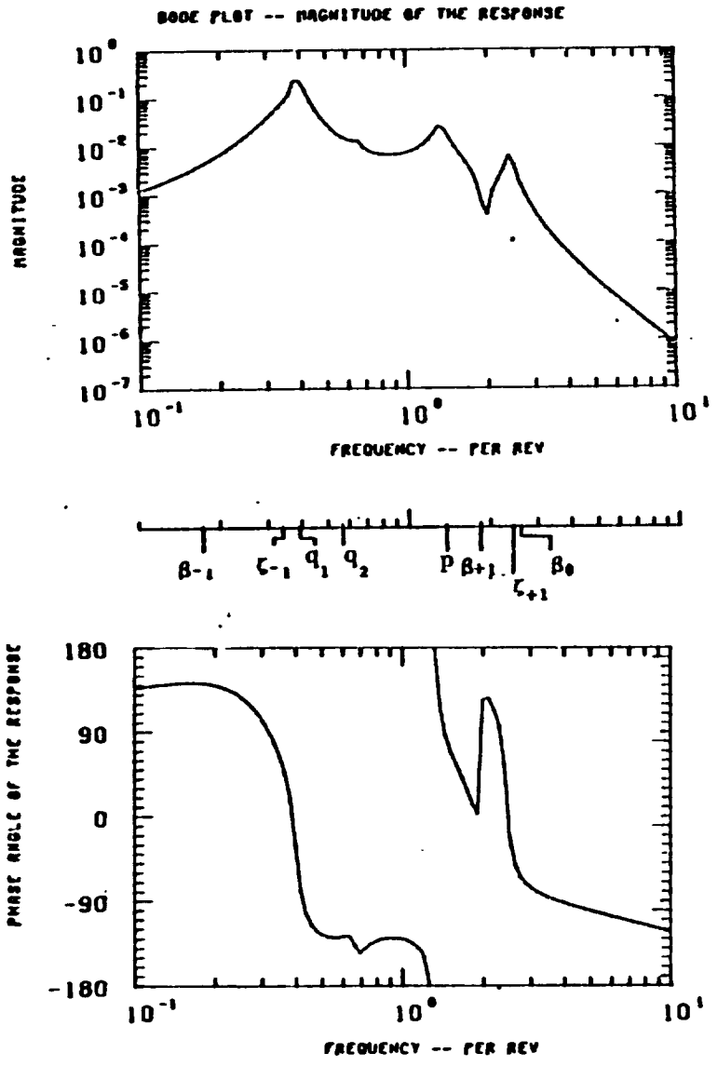

Figure C.19 $\beta_{1s}^{(1)}/\delta_f$ - Blade Lead-Lag to Flaperon (Symmetric)

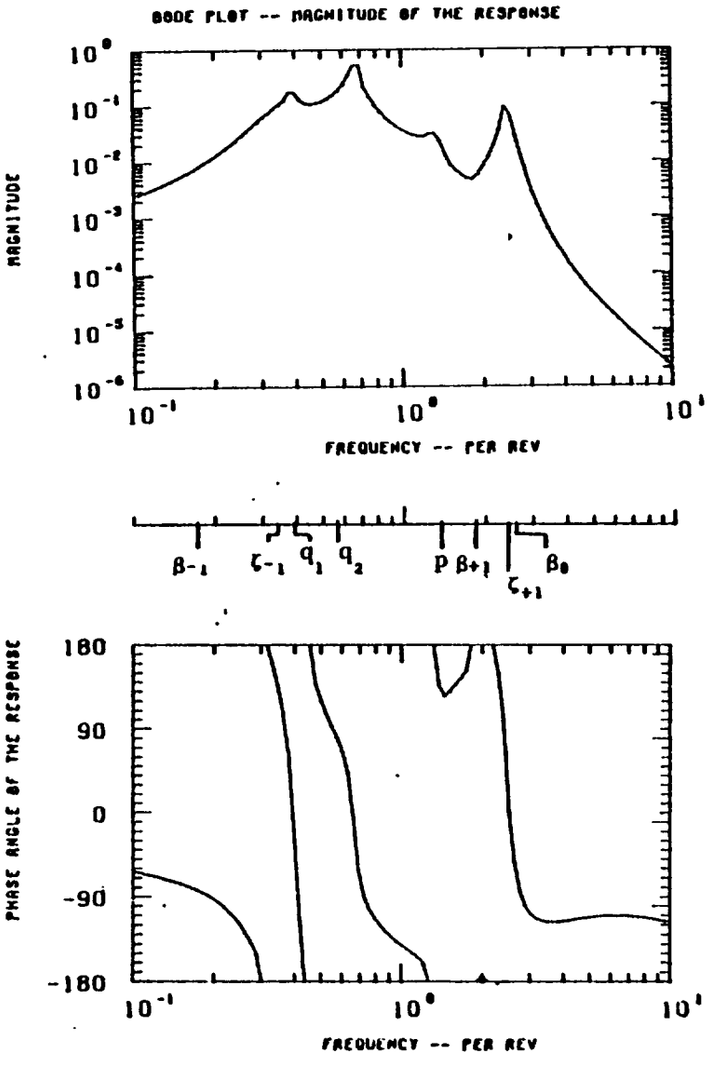

Figure C.20 $\beta_{1s}^{(1)}/\theta_o$ - Blade Lead-Lag to Collective (Symmetric)

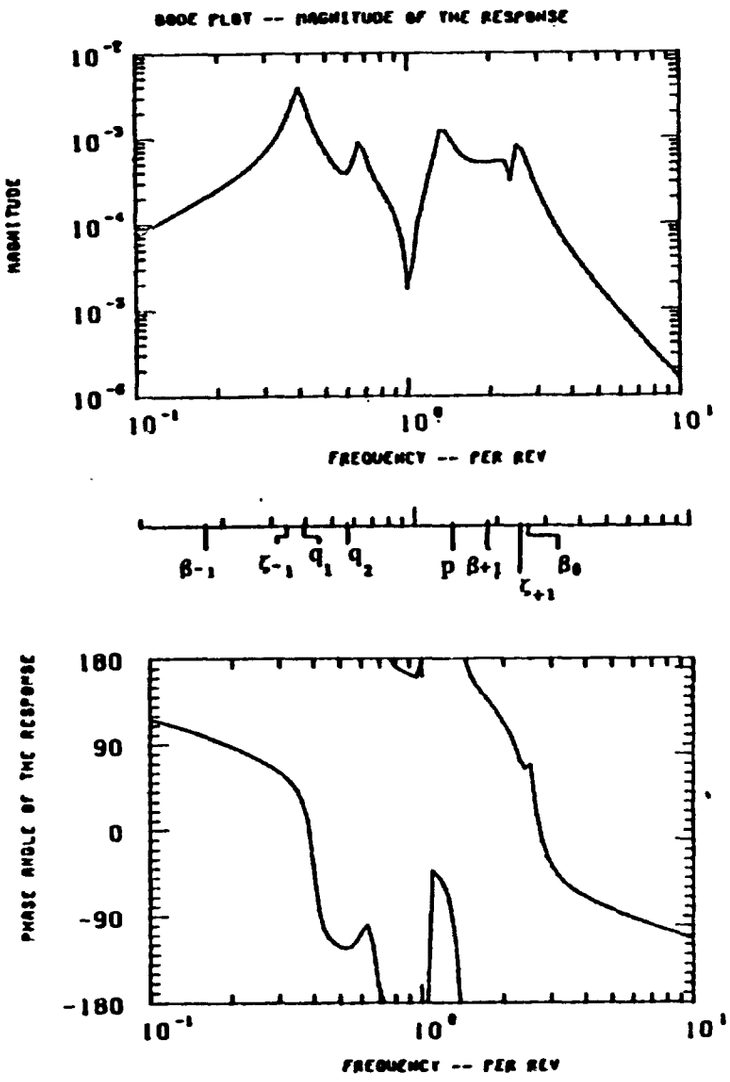

Figure C.21 $\beta_o^{(2)}/\delta_f$ - Out-of-Plane Coning to Flaperon (Symmetric)

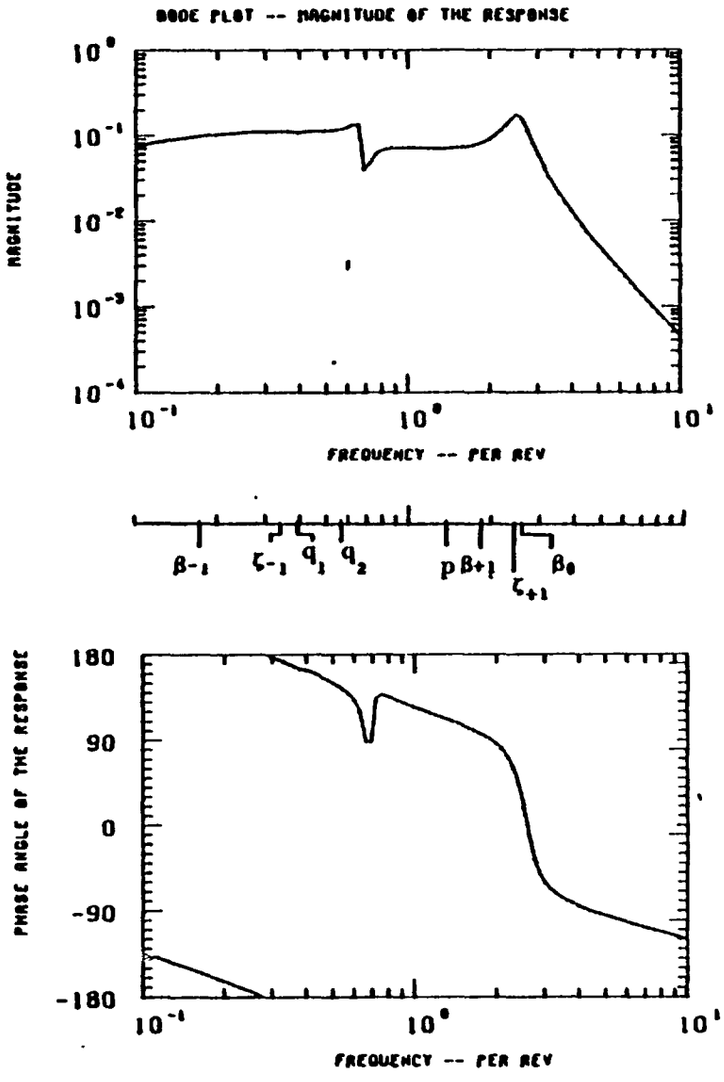

Figure C.22 $\beta_o^{(2)}/\theta_o$ - Out-of-Plane Coning to Collective (Symmetric)

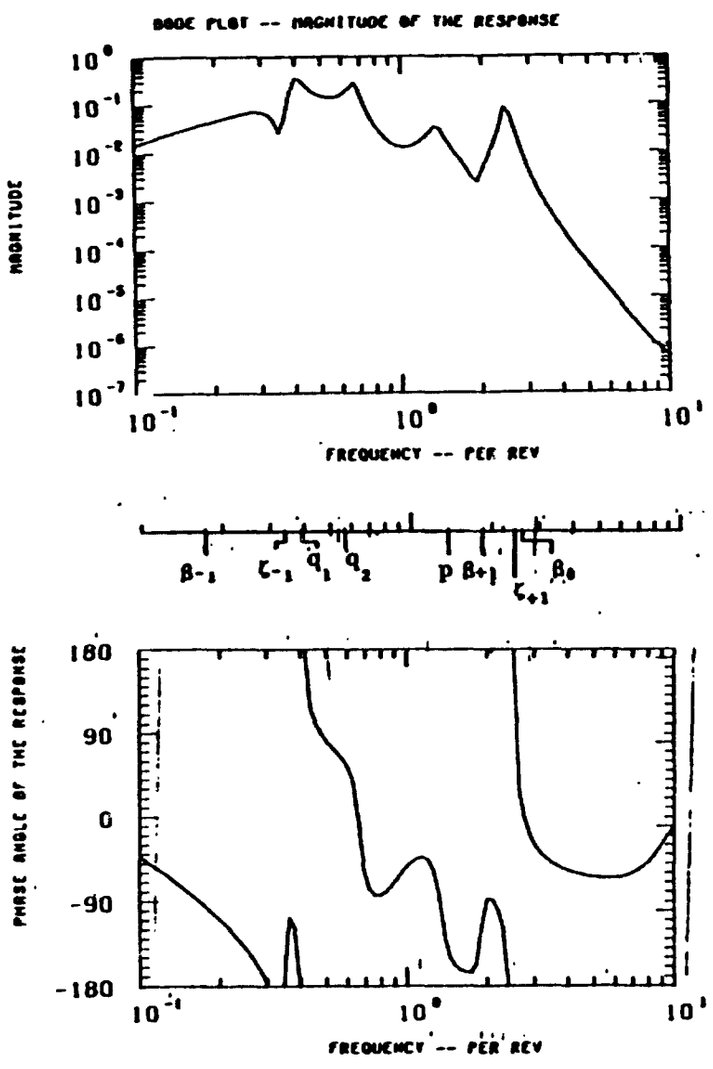

Figure C.23 $\beta_{1c}^{(1)}/\theta_o$ - Blade Lead-Lag to Collective (Symmetric)

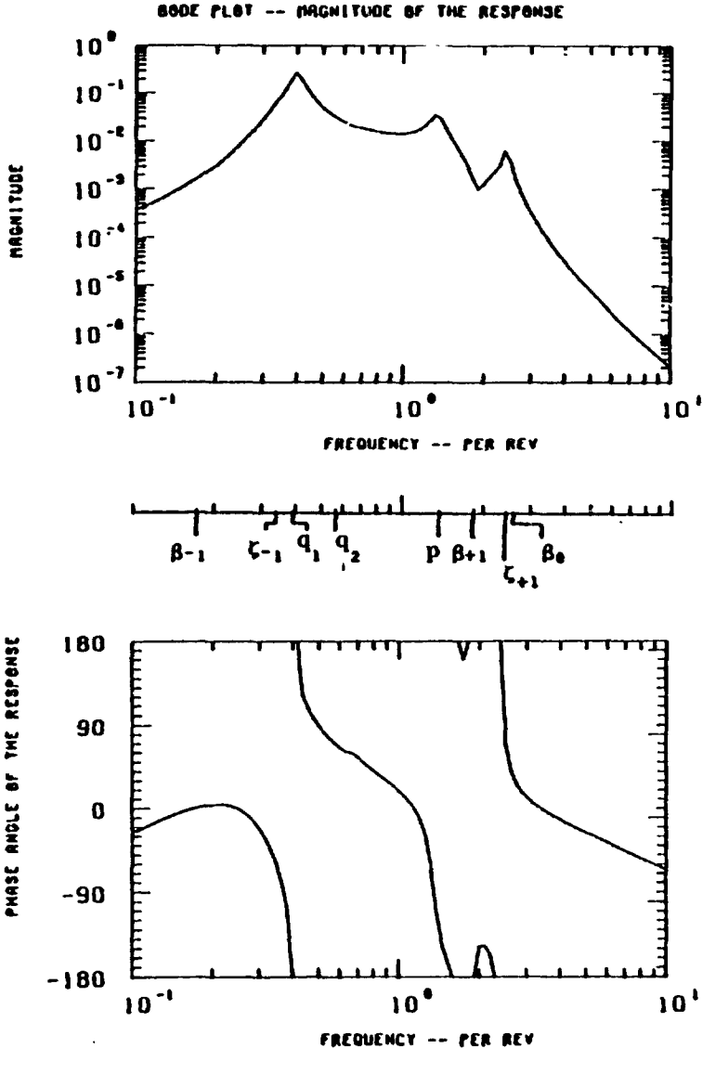

Figure C.24 $\beta_{1c}^{(1)}/\delta_f$ - Blade Lead-Lag to Flaperon (Symmetric)

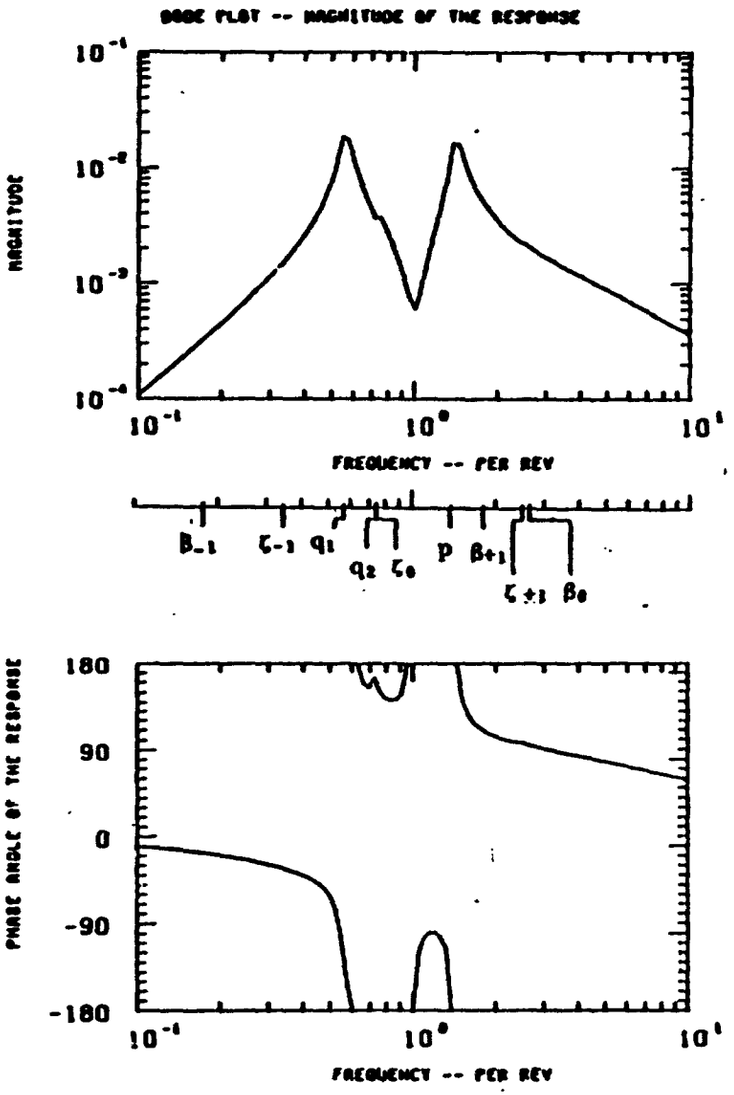

Figure C.25 $\ddot{q}_{w1}/\delta_f$ - Wing Vertical Acceleration to Flaperon (Asymmetric)

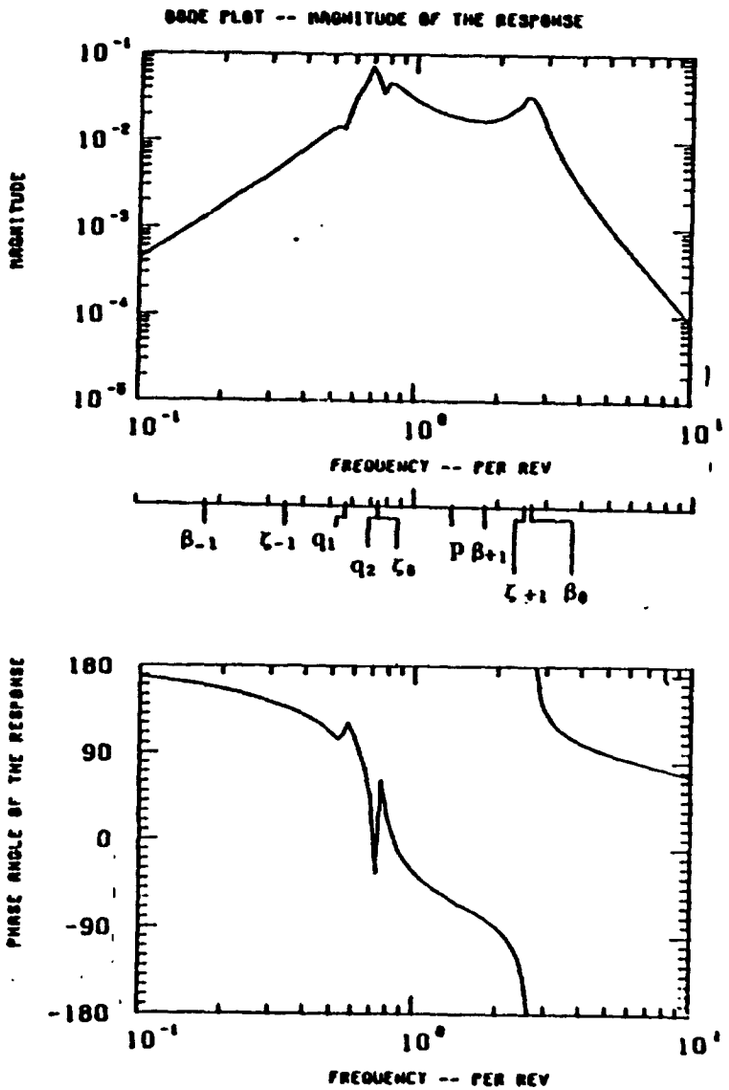

Figure C.26 $\ddot{q}_{w2}/\theta_o$ - Wing Chordwise Acceleration to Collective (Asymmetric)

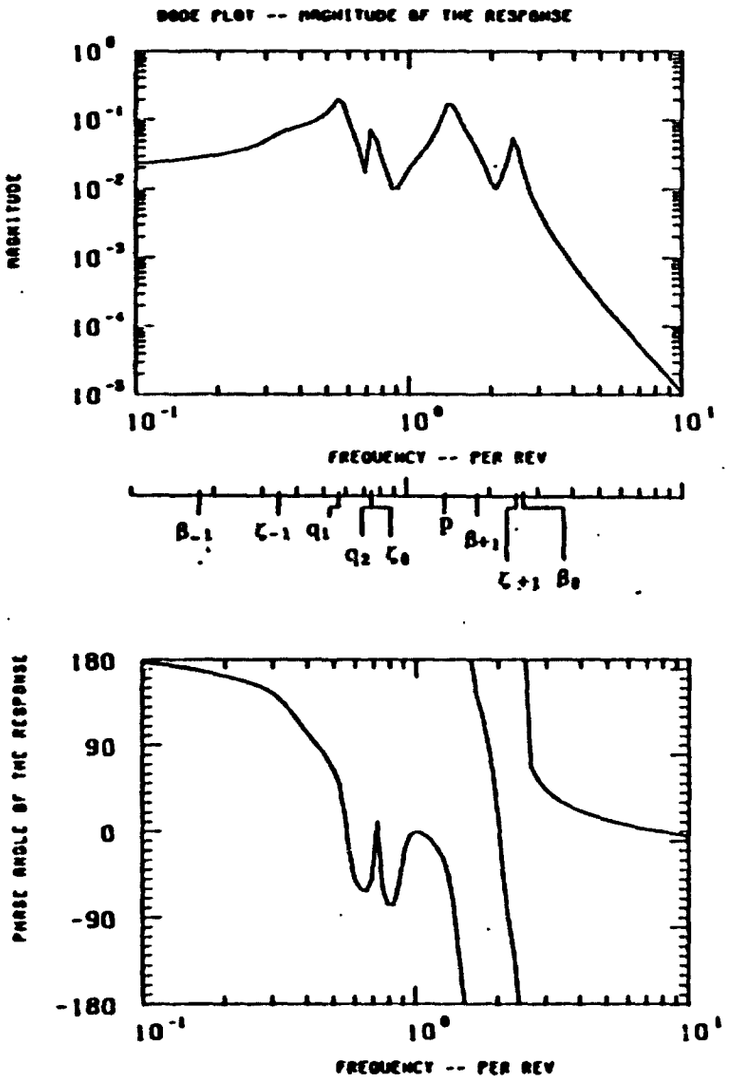

Figure C.27 p/θ_{1c} - Wing Torsion to Lateral Cyclic (Asymmetric)

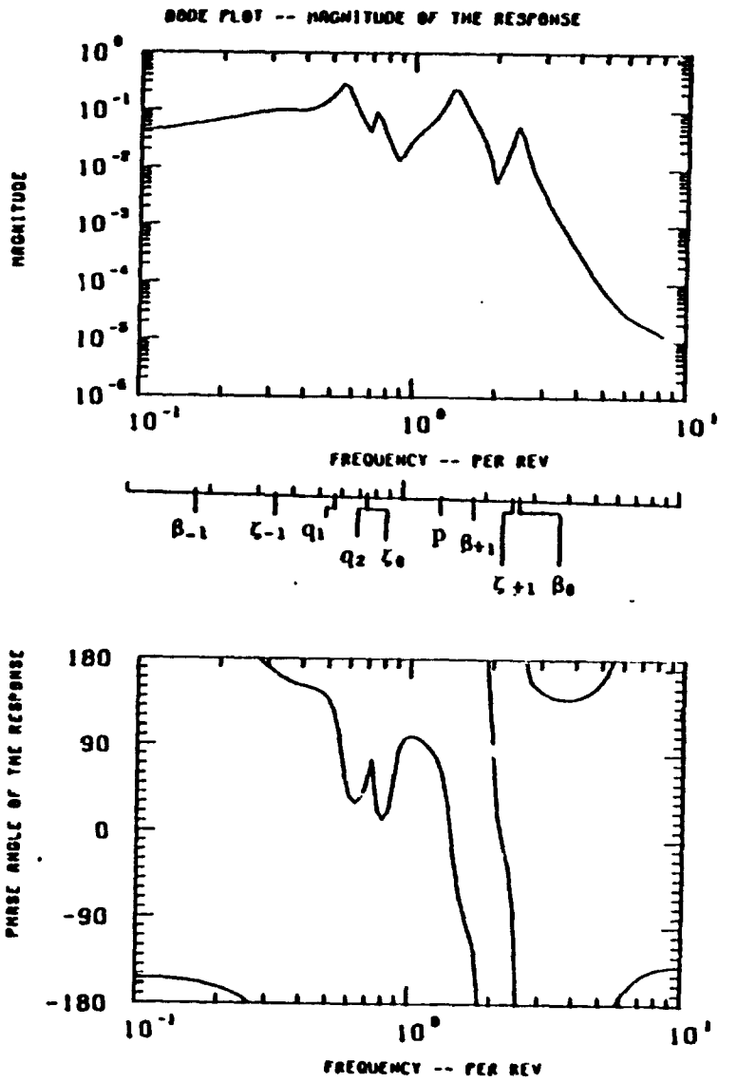

Figure C.28 p/θ_{1s} - Wing Torsion to Longitudinal Cyclic (Asymmetric)

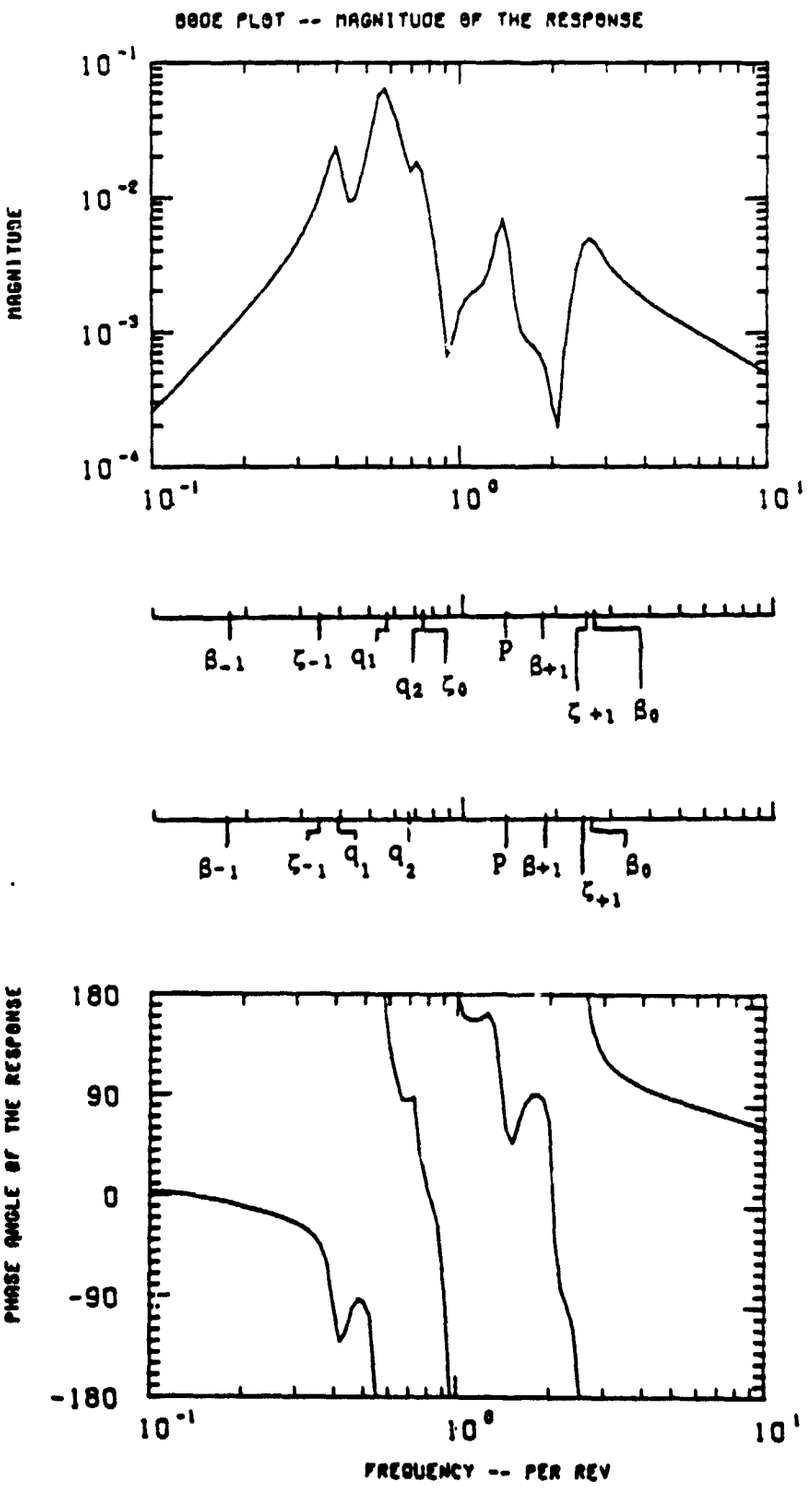

Figure C.29 $\ddot{q}_{w1}/\theta_o$ - Wing Vertical Acceleration to Collective (Coupled Wing Response - Excite One Wing, Measure Same Wing)

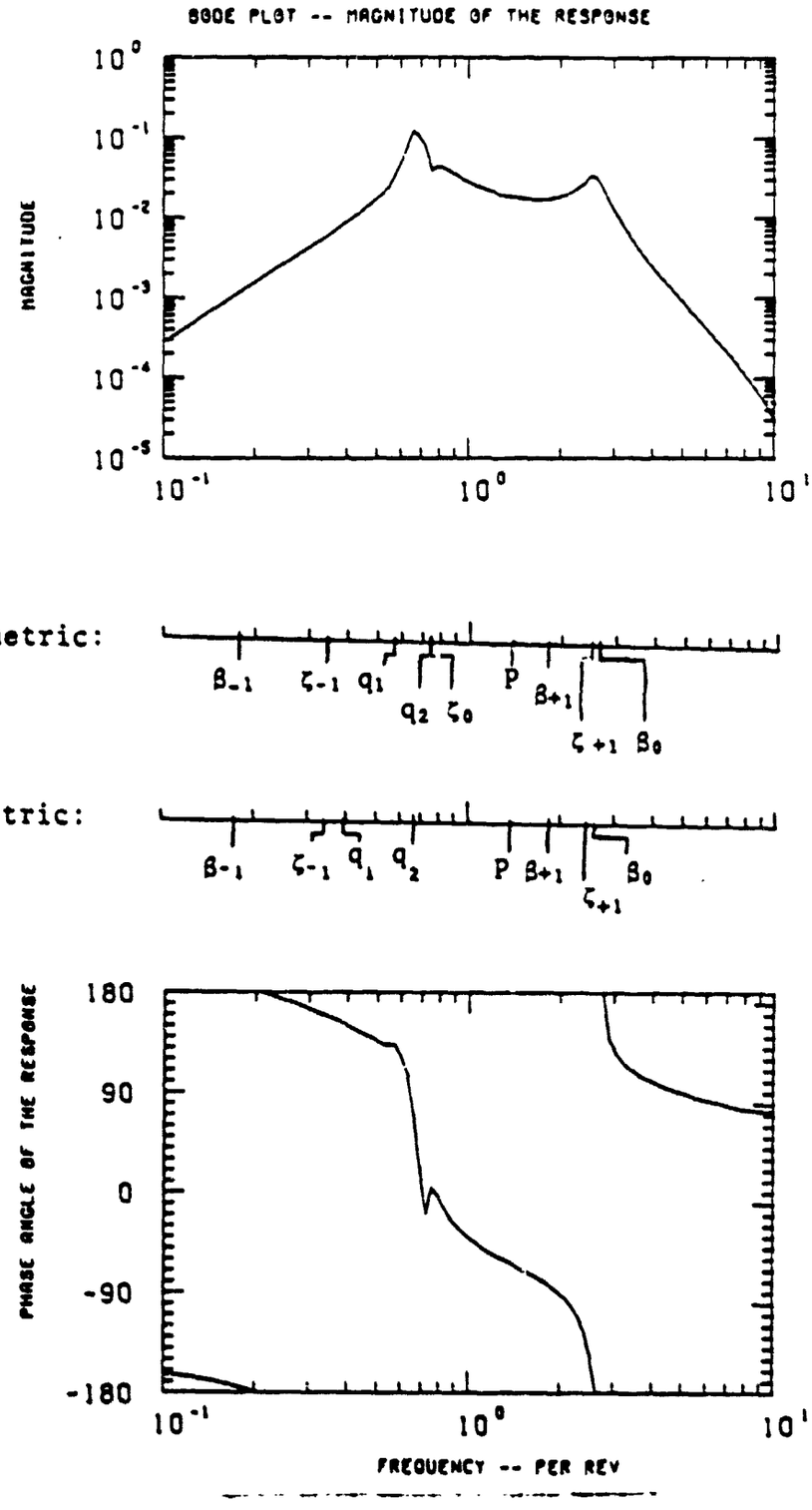

Figure C.30 $\ddot{q}_{w2}/\theta_o$ - Wing Chordwise Acceleration to Collective (Coupled Wing Response - Excite One Wing, Measure Same Wing)

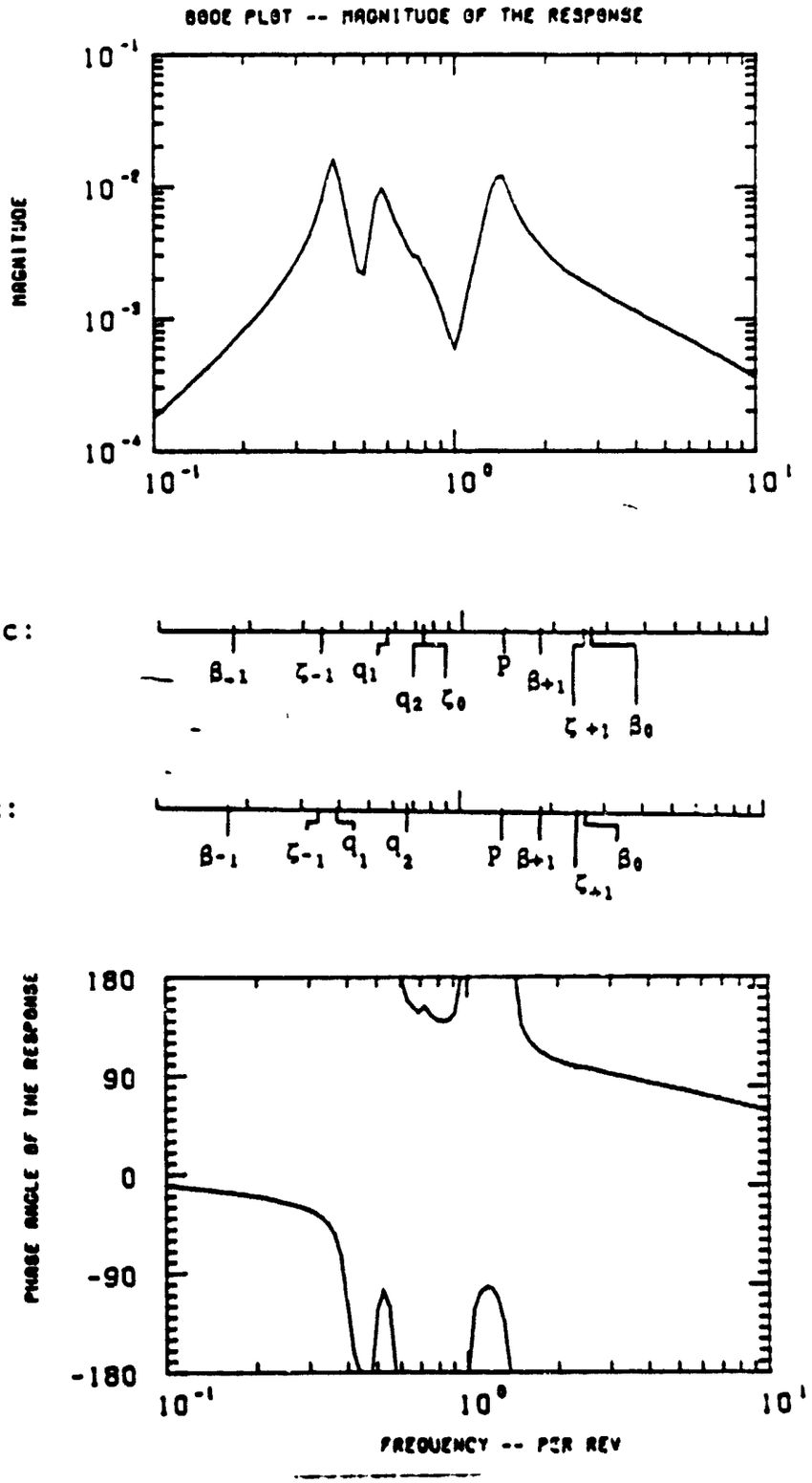

Figure C.31 $\ddot{q}_{w1}/\delta_f$ - Wing Vertical Acceleration to Flaperon (Coupled Wing Response - Excite One Wing, Measure Same Wing)

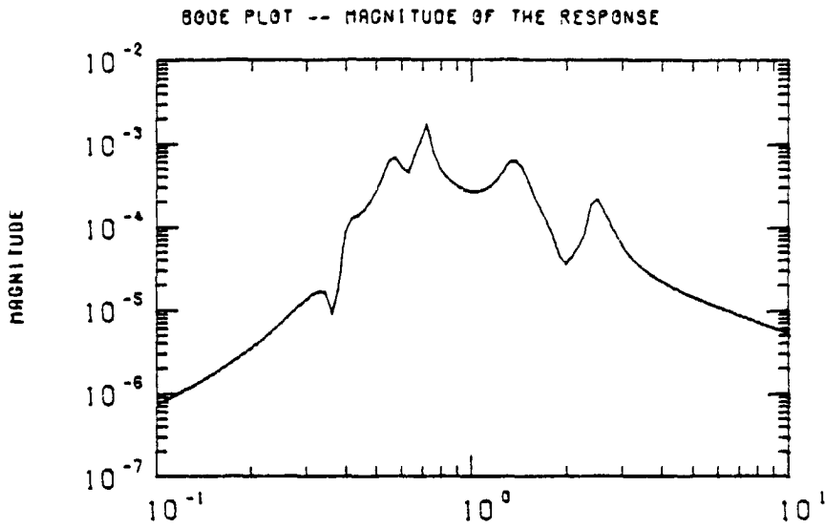

Asymmetric:

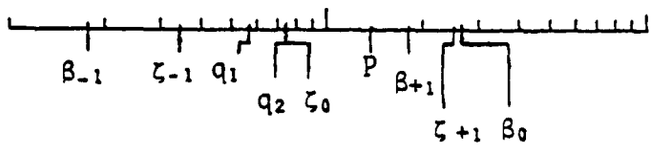

Symmetric:

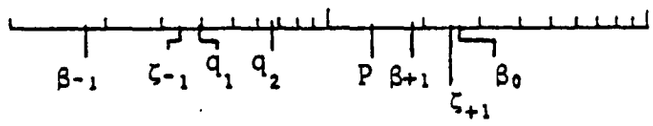

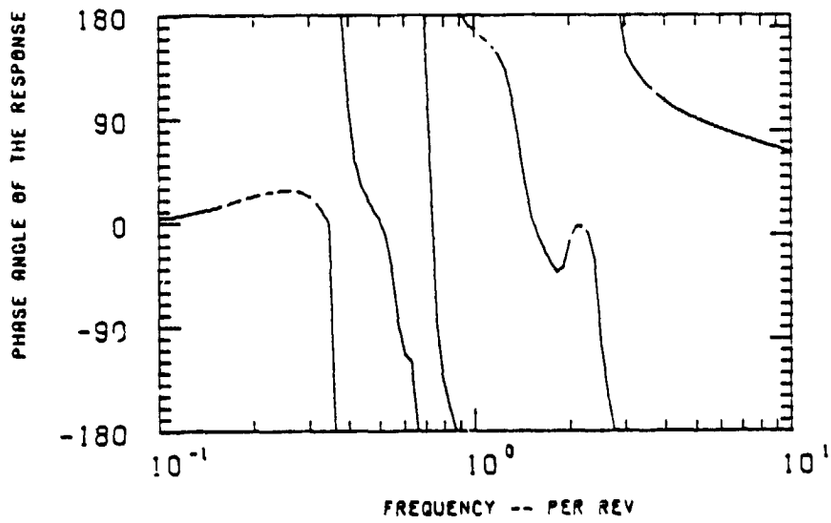

Figure C.32 $\ddot{q}_{w2}/\delta_f$ - Wing Chordwise Acceleration to Flaperon (Coupled Wing Response - Excite One Wing, Measure Same Wing)

REFERENCES

1. Tilt Rotor Project Office Staff, "Tilt Rotor Research Aircraft Familiarization Document," NASA TMX-62,407, Jan. 1975.

2. Johnson, W., "Dynamics of Tilting Proprotor Aircraft in Cruise Flight," NASA TND-767, May 1974.

3. Johnson, W., "Analytical Model for Tilting Proprotor Aircraft Dynamics, Including Black Torsion and Coupled Blade Bending Modes, and Conversion Mode Operation," NASA TMX-6236, Aug. 1974.

4. Johnson, W., "Analytical Modeling Requirements for Tilting Proprotor Aircraft Dynamics," NASA TND-8013, July 1975.

5. Johnson, W., "The Influence of Engine/Transmission/Governor on Tilting Proprotor Aircraft Dynamics," U.S. Army Air Mobility R&D Laboratory, Moffett Field, Calif. (Internal Document).

6. Johnson, W. and Biggers, J., "Shake Test of Rotor Test Apparatus in the 40- By 80-Foot Wind Tunnel," NASA TMX-62418, Feb. 1975.

7. Brown, T.J., "Program for the Analysis of Time Series," NASA TMX-2988, Sept. 1974.

8. Hall, W.E. and Gupta, N.K., "Methods for the Real Time Identification of Vehicle Parameters," TR No. 4 to Office of Naval Research, Feb. 1975.

9. Gantmacher, F.R., The Theory of Matrices, Vol. 1, Chelsea Publishing Co., New York, 1960.

10. Bosley, M.J., et al., "The Determination of Transfer Functions from State Variable Models," Automatica, 1972, Vol. 8, pp. 213-218.

11. Kennedy, C.C. and Pancu, C.D.P., "Use of Vectors in Vibration Measurement and Analysis," Journal of the Aeronautical Sciences, Vol. 14, No. 11, Nov. 1947.

12. Bendat, J.S. and Piersol, A.G., Random Data: Analysis and Measurement Procedures, John Wiley & Sons, Inc., New York, 1971.